Synthesis and Characterisation of Paddlewheel-Porphyrin Conjugates

Benedict Thompson

Master of Science by Research

University of York

Chemistry

January 2022

Abstract

Dimolybdenum paddlewheel complexes with a metal-metal quadruple bond are known for their redox activity and photophysical properties, and have been explored in relation to catalysis, macromolecular chemistry, and photovoltaics. Likewise, porphyrins, owing to their high stability, and redox/photophysical properties, have been studied in similar contexts, notably photovoltaics and molecular electronics. Despite the potential for interaction between the paddlewheel δ orbitals and the porphyrin π system, which could give rise to long-range charge-transfer properties, there have been relatively few examples in the literature of paddlewheel complexes bound to porphyrins in single molecule structures. Herein, synthetic procedures for paddlewheel-porphyrin conjugates with carboxylate and formamidinate ancillary ligands have been developed. The natural lability of the carboxylate ancillary ligands gave rise to mixtures of paddlewheel-porphyrin complexes which could not be separated, but the use of formamidinate ligands led to well-defined conjugates which could be isolated cleanly. Two such examples, Mo_2(N,N'-di(4-anisyl)formamidinate)$_3$(triphenylcarboxyphenylporphyrin) (Mo_2(DAniF)$_3$(A_3B)Porphyrin) and [Mo_2(N,N'-di(4-anisyl)formamidinate)$_3$]$_2$(μ-*trans*-diphenyldicarboxyphenylporphyrin) ([Mo_2(DAniF)$_3$]$_2$(μ-*trans*-A_2B_2Porphyrin)) were characterised by cyclic voltammetry (CV) and UV/Vis spectroscopy, but neither technique provided any evidence of electronic communication between the two components. Supporting density functional theory (DFT) calculations suggest that electron donating N-donor formamidinate ligands raise the energy level of the Mo_2 δ system so that it cannot effectively overlap with the porphyrin π system. Further tuning of the electronic structures of the two components is therefore required to promote electronic interaction between paddlewheel complexes and porphyrins and a parallel project stream has been conducted to assess the redox and optical properties of homoleptic fluorinated paddlewheel complexes, which could provide a route to achieve this. Future work aims to develop a second generation of paddlewheel-porphyrin conjugates with maximised electronic communication, and to explore the electrochemical and photophysical properties of these conjugates in the context of molecular electronics and photovoltaics.

Table of Contents

List of Tables

List of Figures

List of Abbreviations

ET- Electron transfer

IVCT – Inter-valence-charge-transfer

HOMO- Highest occupied molecular orbital

LUMO- Lowest unoccupied molecular orbital

CR- Charge resonance

MLCT- Metal-to-ligand-charge-transfer

CV- Cyclic voltammetry

UV/Vis (spectroscopy) – Ultraviolet visible (spectroscopy)

LMCT- Ligand-to-metal-charge-transfer

DSSC- Dye sensitized solar cell

THF- Tetrahydrofuran

ACS – American Chemical Society

DCM- dichloromethane

DDQ - 2,3-dichloro-5,6-dicyano-1,4-benzoquinone

TFA – Trifluoroacetic acid

MOF – Metal-organic framework

NAD(H)- Nicotinamide adenine dinucleotide (+ hydrogen)

DFT- Density functional theory

XRD – X-ray diffraction

TiPB - 2,4,6-triisopropylbenzoate

DAniF - N,N'-di(4-anisyl)formamidinate

NMR (spectroscopy) – Nuclear magnetic resonance (spectroscopy)

MALDI-TOF-MS – Matrix assisted laser desorption ionisation time of flight mass spectrometry

ESI-MS – Electron spray ionisation mass spectrometry

APCI-MS – Atmospheric-pressure chemical ionisation mass spectrometry

2Me-THF – 2-Methyl tetrahydrofuran

HSQC (NMR spectroscopy) – Heteronuclear single quantum coherence (nuclear magnetic resonance spectroscopy)

HMBC (NMR spectroscopy) - Heteronuclear multiple bond correlation (nuclear magnetic resonance spectroscopy)

COSY (NMR spectroscopy) – Correlated spectroscopy (NMR spectroscopy)

DPV – Differential pulse voltammetry

DMeF – Dimethylformaldehyde

DFArF - N,N’-di(fluoroaniline)formamidinate

1,2-DCB – 1,2-Dichlorobenzene

Acknowledgements

I would first like to express my gratitude to my supervisor, Luke Wilkinson. Luke has provided outstanding support and rapid feedback throughout this project as well as teaching me everything I know about air-sensitive chemistry, and the (surprisingly nuanced) art of making presentable figures and readable reports. His unabating enthusiasm has also helped me to remain optimistic throughout, even when results eluded us for months on end. I would also like to thank my second supervisor Jason Lynam for providing calm, level-headed support and advice where required and for his outstanding performances on the cricket pitch keeping the chemistry team at the right end of the league table.

I would also like to thank Heather Fish and Alex Heyam for their help with NMR experiments, Karl Heaton for running dozens of mass spectrometry samples, and Adrian Whitwood and Theo Tanner for their patience collecting and analysing some dreadful single crystal samples as well as a few usable ones.

I would also like to thank Chris Goult for teaching me that cannula filters>filter sticks. Furthermore, I would like to thank members of the Wilkinson group both past and present, as well as everybody in E214 for providing excellent company over the course of the year, both in the laboratory and on innumerable Wednesday socials. Finally, a big thank you to the Department of Chemistry and the University of York for funding my research this year.

Declaration

I declare that this thesis is a presentation of original work, and I am the sole author. This work has not previously been presented for an award at this, or any other, University. All sources are acknowledged as References.

Introduction

Metal-Metal Quadruple Bonds and Paddlewheel Complexes

The metal-metal quadruple bond was first recognized in 1964 in the $[Re_2Cl_8]^{2-}$ ion (**Figure 1**).[1] Shortly after, it became clear that rather than being an isolated curiosity, the formation of these short metal-metal quadruple bonds applied to a variety of transition metals. The quadruple bond itself consists of one σ bond, formed by the end-on overlap of two d_z^2 orbitals, two orthogonal π bonds from the side-on combination of the d_{xz} and d_{yz} orbitals, and one δ bond formed from the face-on overlap of the d_{xy} orbital (**Figure 2**). The dx^2-dy^2 orbital, although involved in metal-ligand bonding, does not take part in metal-metal bonding. It should also be noted that the σ and π contributions to the M-M bond are insensitive to the angle of rotation about the metal-metal axis, but the δ bond is strongly dependent on the orientation of the two metal atoms with respect to one another, and whilst only a small contribution to the overall bond strength, it does impart additional stability to the molecule. It is this δ bond energy that stabilises the eclipsed orientation of the chloride ions in the initial $[Re_2Cl_8]^{2-}$ example relative to the staggered arrangement, which would otherwise be favoured on steric grounds.

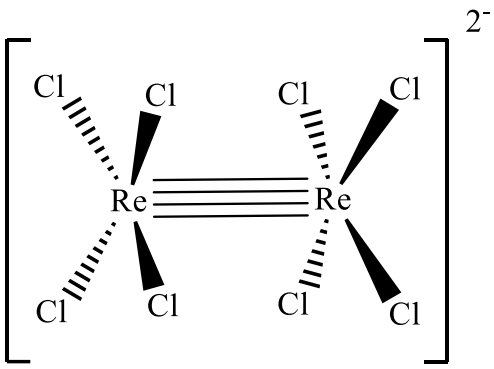

Figure 1: Structure of the $[Re_2Cl_8]^{2-}$ anion

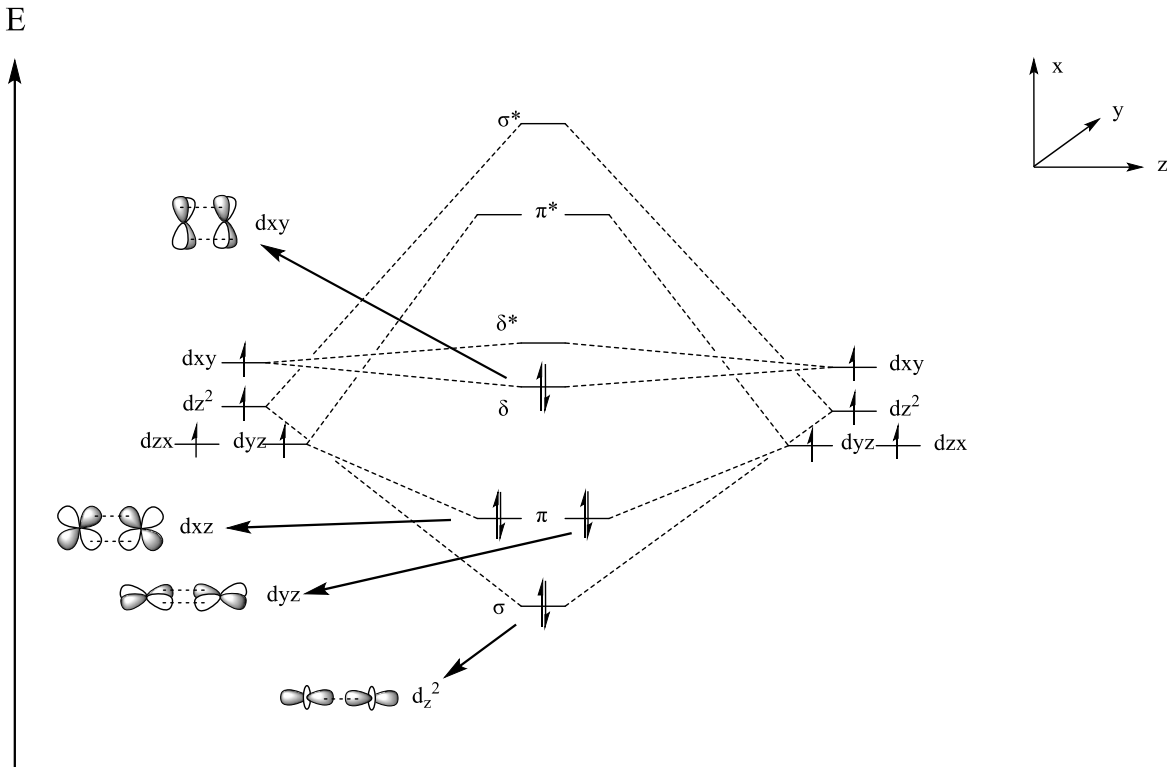

Figure 2: Qualitative molecular orbital diagram for the metal-metal quadruple bond[2]

The paddlewheel structure of $Mo_2(OAc)_4$ was first reported by Lawson and Mason in 1965 (**Figure 3**, left). It quickly became apparent that this structure, like the M-M quadruple bond itself, applied to a wide range of metals and accompanying ligands. The general structure of a quadruply bonded dimetal paddlewheel complex is depicted in **Figure 3**, right. From a qualitative assessment of the molecular orbital diagram for the metal-metal quadruple bond (**Figure 2**), it is easy to imagine that electrons may be added to or removed from quadruply bonded paddlewheel complexes without compromising the structure of the ligand framework. Indeed, paddlewheel complexes have become well-known for their redox activity and in addition to this, exhibit interesting photophysical properties.[3,4] As a result, research on quadruply bonded paddlewheel complexes has been far-reaching, ranging from studies of the fundamental mechanisms of electron transfer,[2] to diverse applications including catalysis,[5–7] macromolecular chemistry,[8] and photovoltaics.[9,10]

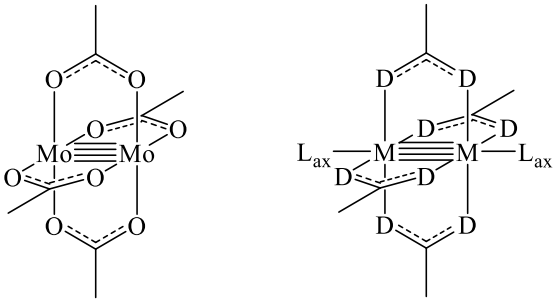

Figure 3: (Left) Structure of $Mo_2(OAc)_4$. (Right) Generalised quadruply bonded dimetal paddlewheel complex. D denotes donor atom

Electronic Coupling and Electron Transfer

Studies investigating electron exchange between electronically coupled redox sites have been known since the 1960s,[11] and instances where both redox sites are identical but for the level of oxidation are known as mixed valence compounds. The archetypal example is the Creutz Taube ion which consists of two Ru ions bridged by a pyrazine linker and an overall charge of 5+.[12] In mixed valence complexes, the electron density can spread itself out in several ways across the two redox centres- sometimes localised entirely on one centre, sometimes spread evenly between the two, or indeed anywhere in between.[13] The Class I-III nomenclature employed to characterise these different situations was first introduced by Robin and Day in 1967 as a qualitative measure for the degree of electronic communication between redox centres connected by a covalent bridge.[14]

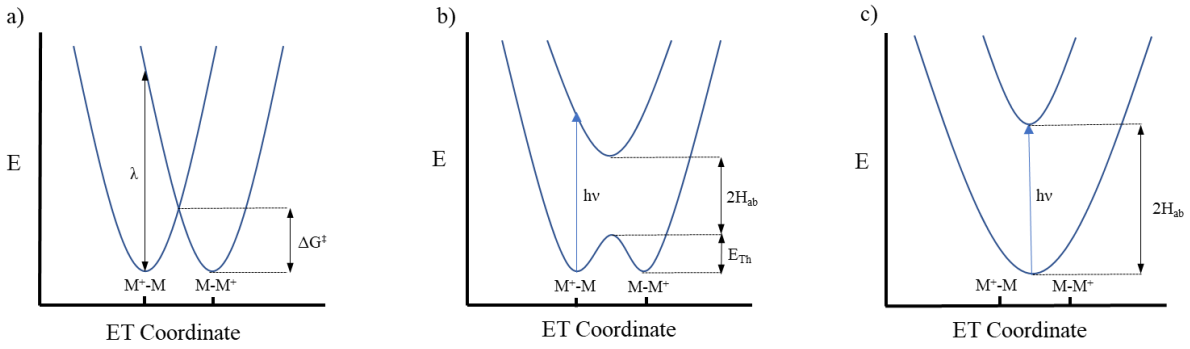

Figure 4: Energy level diagrams for mixed valence species **a**) Class I, **b**) Class II, **c**) Class III. (ET denotes electron transfer)[13]

At one extreme, Class I denotes compounds which exhibit no electronic communication and behave physically and spectroscopically as two independent redox centres (**Figure 4**, **a**). In this instance, the Marcus/Hush model for spontaneous electron transfer applies. The Franck Condon principle states that electrons move much faster than nuclei and therefore that electron

transfer occurs against a stationary nuclear framework. Electron transfer from the vibrational ground state is unfavourable, as oxidation/reduction of a metal centre is associated with contraction/expansion of bond lengths (and re-orientation of the solvent shell), and the stationary nuclear framework does not have time to react to the transfer. The Marcus-Hush model therefore stipulates that spontaneous electron transfer must therefore wait until random vibrations bring the bond lengths and solvent shell to an orientation where electron transfer is favourable. The vibrations that control such changes are simplistically modelled as harmonic oscillators, and the rate of electron transfer may be expressed in terms of λ, the reorganisation energy. In Class I systems, λ is invariably large enough that electron transfer does not occur on the timescale that the complex is observed upon (e.g. 10^{-15} s for UV/Vis spectroscopy), and the result is that the two redox centres appear and behave as separate entities.

In Class II, electronic communication (quantified by the electronic coupling parameter H_{ab}) does exist between the two redox centres but is not strong enough that the two redox centres appear indistinguishable. In this case, 2 minima exist corresponding to localisation of the unpaired electron on each centre, but there is a barrier to electron transfer (**Figure 4**, **b**). Upon observation the redox centres appear independent, but an important distinction from Class I is that electronic coupling allows photochemically (or thermally) induced inter-valence charge transfer (IVCT) and interconversion of the two isovalent states (i.e. upon promotion an exited electron may relax into either of the energy minima). This manifests as an IVCT band in the UV/Vis spectrum, with a diagnostic change in dipole moment, which may be probed independently by electron absorption spectroscopy.[13]

Class III denotes fully delocalised complexes, where the ground state consists of a broad hyper surface with one minimum (**Figure 4**, c). In this instance electronic coupling is greater than the reorganisation energy, and in the mixed valence state each redox centre will have the same preferred structure with intermediate structural characteristics (bond lengths, solvent shell etc.) to the oxidised and reduced forms. A band corresponding to the HOMO-LUMO transition is still observed in the UV/Vis spectrum, but unlike Class II this is not associated with a change in dipole moment (as there is no net movement of charge) and this absorption is accordingly termed a charge resonance band.

Quadruply bonded paddlewheel complexes bound by a linking organic unit, so-called dimers of dimers (**Figure 5**), have emerged as ideal candidates for the systematic study of mixed valency, owing to their well-defined $\sigma^2\pi^4\delta^2$ electronic structure at the M_2 core. Consequentially, charge transfer events may be confidently assigned as movement to/from the singly degenerate M_2 δ HOMO and interference from other electrons in metal based orbitals is largely precluded.[15,16] Furthermore, investigations of the electrochemical and spectroscopic characteristics of these complexes have served the dual purpose of probing the factors underlying electronic coupling between redox centres, and as a tool for anticipating the properties of more complex architectures with integrated M-M quadruple bonds.[17]

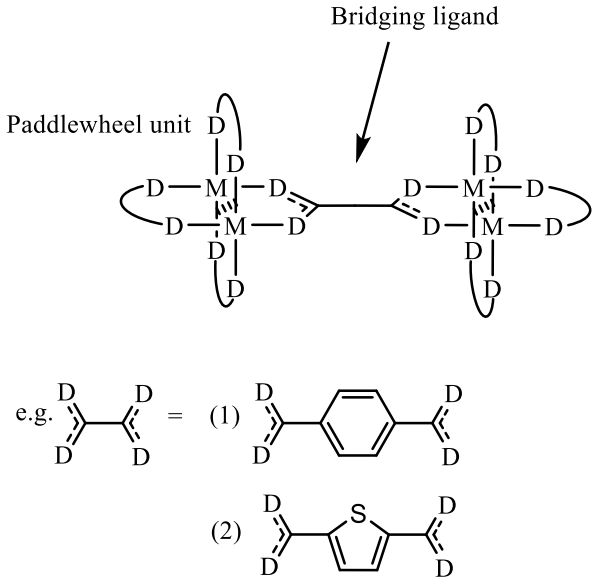

Figure 5: (Top) Generic form of paddlewheel dimers-of-dimers. (Bottom) Example bridging ligands. D denotes donor atom, most commonly oxygen or nitrogen

The extent of electronic coupling between the two metal centres in these dimers-of-dimers is dependent on a variety of factors including the metal itself and the length and nature of the bridging ligand. For instance, tungsten complexes are uniformly more delocalized than their molybdenum counterparts, as the δ-orbitals are around 0.5 eV higher in energy and more closely aligned with the ligand π* orbitals, facilitating a greater degree of orbital overlap across the complex.[16] The result is that tungsten complexes may reach Class III on the Robin and Day classification scheme, whilst their molybdenum counterparts remain Class II. Similarly, bridging ligands with integrated sulfur atoms demonstrate more electronic coupling than their nitrogen or oxygen-based analogues, as sulfur based ligands are less basic, lowering the ligand π* (LUMO) energy to be closer to the M_2 δ HOMO.[18,19]. Electronic communication decreases with increasing distance between the redox centres, and few examples of Class III behaviour in mixed valent systems are found at distances exceeding 10 Å.[20–22] Maintaining conjugation across the bridging ligand is also an important prerequisite (demonstrating that this effect is more than simply a through-space interaction) and instances where steric constraints force the conjugated bridge out of plane are associated with a loss of stabilization energy. Spectroscopically, increasing electronic coupling between the two redox centres is observed as a red-shifting and growth in intensity of the IVCT band. Electrochemically, this manifests as increased separation (in volts) between the first and second redox processes, owing (in part) to charge stabilisation in the mixed valence state. It should be noted this separation is dependent on a number of factors (e.g. electrostatics, inductive effects etc.) of which charge stabilisation from delocalization is only one. Therefore, this should only be used for qualitative comparisons between structurally similar systems.[13]

As well as studies of mixed valency between identical metal-based redox centres, research in this field has expanded into hybrid charge transfer complexes with both inorganic and organic components, where quadruply bonded paddlewheels are covalently tethered to a second redox

centre. In one such example, a Mo_2^{4+} paddlewheel was coupled with an organic triarylamine unit, and the charge transfer properties probed by UV/Vis spectroscopy and cyclic voltammetry (CV) (**Figure 6**).[23] All complexes showed Mo_2 δ – ligand π MLCT transitions, but the singly oxidised (Mo_2^{5+}) species also exhibited low energy LMCT from the triarylamine to the electron deficient Mo_2^{5+} centre. Further to this, interaction between the two redox centres was shown to reduce the reversibility of the triarylamine oxidation (which occurs at a higher potential than paddlewheel oxidation) due to significant N → Mo_2^{5+} charge transfer in the radical species. Much like mixed valence [(Mo_2)-bridge-(Mo_2)]$^+$ complexes, electronic coupling was improved with increasing sulfur content in the bridge, due to greater alignment between the Mo_2 δ orbitals and the triarylamine π system, and the conclusion drawn was that much of the conceptual framework from mixed valency studies could be equally applied to asymmetric charge-transfer systems.

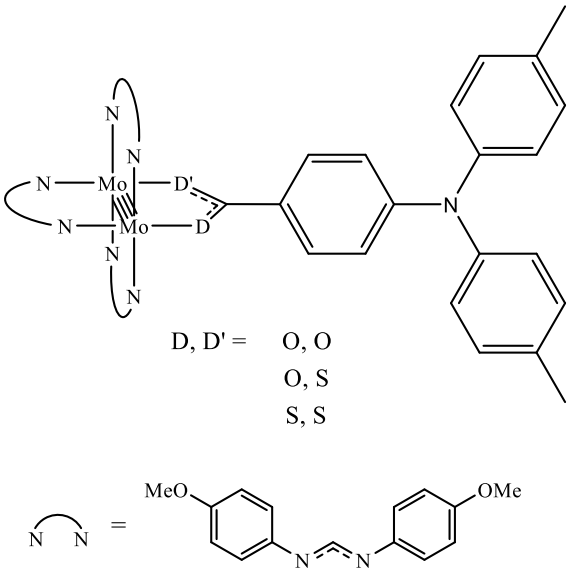

Figure 6: Mo_2 paddlewheel complex covalently tethered to a triarylamine group[23]

Similarly, Byrnes *et al.* have prepared systems where molybdenum and tungsten paddlewheels are covalently tethered to a variety of thiophenes via carboxylate bridging ligands (**Figure 7**).[10] Rather than studying the fundamentals of electron transfer as in previous examples, these complexes were investigated as a precursor to polythiophenes with pendent bimetallic units for solar harvesting applications. In these examples, there is strong electronic coupling between the metal centre and the thiophene, observed as an MLCT absorption in the visible region from M_2 δ to thiophene π*. This MLCT was redshifted by the addition of further thiophene units suggesting greater alignment of the π and δ systems. Furthermore, this MLCT signal also redshifts and grows in intensity upon substitution of Mo for W, which as discussed is a consequence of the increased energy of the frontier δ orbitals.

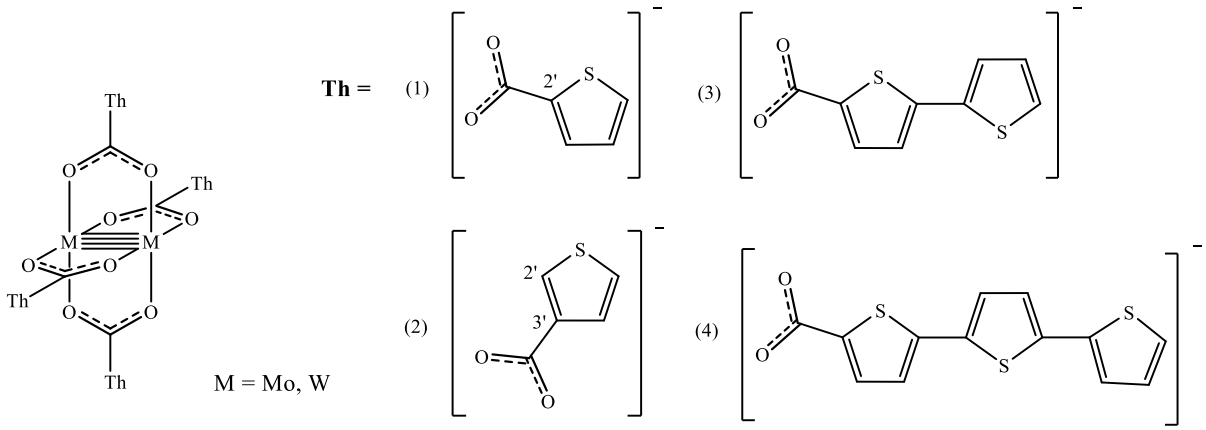

Figure 7: Paddlewheel complexes with pendent carboxythiophene ($^{-}O_2C$-Th) ligands[10]

A further recent example in the literature consists of covalent attachment of a quadruply bonded Mo_2 paddlewheel complex to a sulfur containing heterocyclic ligand, which in the cationic state can form an aromatic system incorporating the Mo_2 δ electrons due to overlap between the δ orbitals and the ligand π system (**Figure 8**, left).[24] This was conducted with a view to exploring the physical origin of, and the limits of aromaticity. Furthermore, metal-ligand orbital mixing between a paddlewheel and a conjugated organic component in the complex depicted in **Figure 8**, right, has been shown to improve electrical conductance by 1-2 orders of magnitude relative to purely organic analogues, showcasing the potential for paddlewheel/organic hybrid systems for use in molecular electronics applications.[25] Such examples demonstrate research pairing dimolybdenum paddlewheel complexes with pendent organic units can take both a chemical fundamentals or an application-focussed perspective, and with a broad set of redox-active organic ligands to choose from, this concept may be taken forward in a variety of different ways.

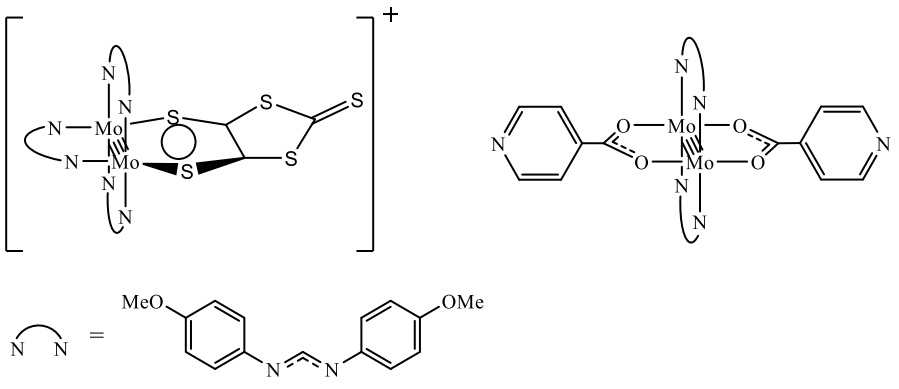

Figure 8: (Left) Mo_2 paddlewheel bound to sulfur containing heterocyclic ligand[24], (Right) *trans*-Mo_2 nicotinate complex for molecular electronics applications[25]

Tuning the properties of the Mo_2 quadruple bond

The ligand framework in a paddlewheel complex plays an important role in influencing the properties of the molecule as a whole. For instance, redox potentials, spectroscopic properties, or even crystal packing behaviour can vary greatly according to both the class of ligand (e.g., carboxylate vs formamidinate) and any substitution at the ligand periphery.[26–30] It is therefore important to choose the ligand set wisely when designing a synthesis or tailoring the properties of a material. To this end, there are several publications in the literature dedicated to systematic investigation of the effect of changes to the ancillary ligand set on dimolybdenum paddlewheel complexes.

Hicks *et al.* in 2012 probed the effect of modifying the donor ligand atoms on the electronic structure of Mo_2 quadruply bonded paddlewheel complexes (**Figure 9**).[26] Cyclic voltammetry (CV) experiments showed that the $\Delta E_{1/2}$ values for the $Mo_2^{4+/5+}$ redox couple (i.e. 1 electron oxidation of the paddlewheel) correlate with ligand basicity, and that the potentials for this process vary over a range of 0.9 V, giving broad scope for redox tunability within this paradigm. This effect arises because the more basic ligands are better able to donate electron density to the Mo_2 core and hence stabilise the electron deficient Mo_2^{5+} oxidation state. From an electronic structure perspective, more basic donor ligands raise the Mo_2 δ (HOMO) energy level, with DFT calculations suggesting a difference of 1.4 eV between the NN and the SS analogues. The effect on the energy of the Mo_2 δ (HOMO) – ligand π* (LUMO) transition is less dramatic, as to some extent more basic ligands raise the LUMO energy alongside the HOMO, but there are changes to the energy of this MLCT, which constitutes the most intense UV/Vis absorption for this set of complexes.

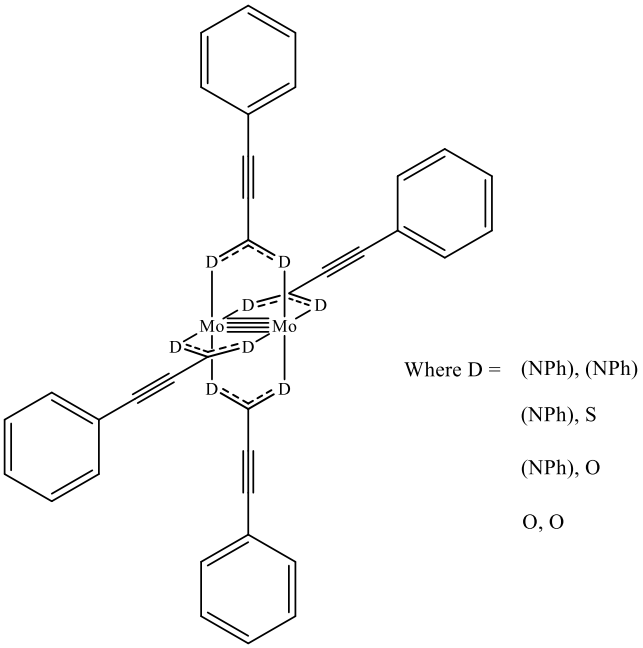

Figure 9: Dimolybdenum paddlewheel complexes investigated by Hicks et al.[26]

In a similar study, Lin *et al.* systematically investigated the role of formamidinate ligands in influencing the properties of dimolybdenum paddlewheel complexes.[27] Here, rather than altering the donor atoms, changes were instead made to the substitution pattern on the pendent aromatic groups, and the resultant changes to the redox potential and UV/Vis absorptions were recorded (**Figure 10**).

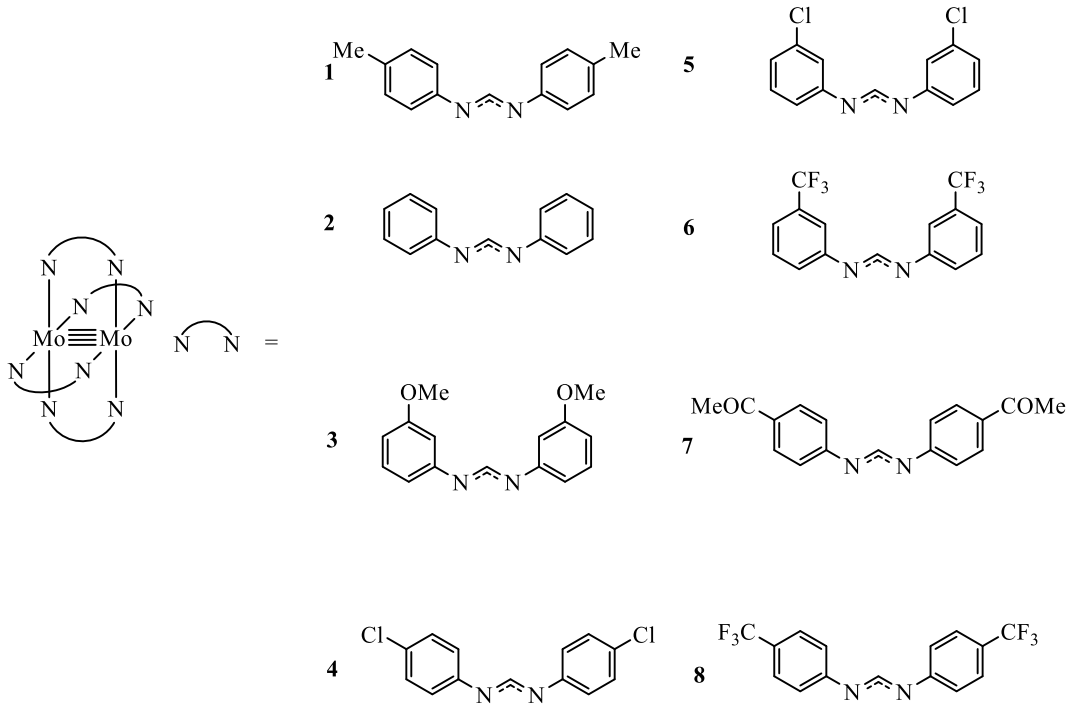

Figure 10: Formamidinate variants investigated by Lin[31]

As in the previous example, the redox potential for the 1 electron oxidation of the paddlewheel ($Mo_2^{4+/5+}$) was probed by CV experiments. In this case, the potential required was directly correlated to the Hammett constant (σ) of each formamidinate. Substituents with more positive σ values were found to increase $\Delta E_{1/2}$. Intuitively this is an unsurprising result, as ligands such as the CF_3 variants (**6** and **8** in **Figure 10**) with greater σ values are more electron withdrawing in nature, lowering the δ energy level of the Mo_2 quadruple bond, making the paddlewheel more difficult to oxidise. The redox potential (relative to Fc/Fc^+) varies between 244 mV for (**1**) to 795 mV for **8**, a range of about 0.5 V- less than the 0.9 V observed upon ligand donor atom alteration,[26] but still a broad window to tune paddlewheel electrochemistry. The different formamidinate variants have a much less pronounced effect on the spectroscopic properties. This is largely because changes to the remote substituents move both the δ and δ* orbitals (the HOMO and LUMO respectively in formamidinate-based paddlewheels) in tandem, so the energy gap between them remains similar. Consequentially, varying the formamidine has only a small effect on the key features of the UV/Vis spectrum. In addition to the δ-δ* transition, lower intensity LMCT transitions corresponding to electron transfer between the ligand π orbitals and the metal δ* and π* are largely unaffected by these changes. Consequentially, the

overall conclusion drawn was that formamidine remote substituents are a useful tool to tune the redox properties of the paddlewheel but leave the spectroscopic properties largely unaffected.

These findings are largely in agreement with those found using Ru_2 homoleptic paddlewheels with fluorinated benzoate ligands as an approach to tune redox behaviour (**Figure 11**).[32] This was carried out with a view to designing charge transfer complexes where the ruthenium paddlewheel is covalently tethered to an electron acceptor. In this instance, the efficacy of charge transfer was strongly dependent on the redox properties of both the donor paddlewheel and the acceptor.

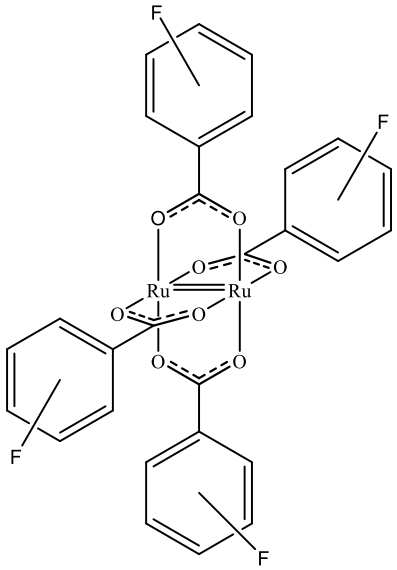

Figure 11: Ru_2 paddlewheel complexes with fluorinated benzoate ligands[32]

In general, the $Ru_2^{4+/5+}$ redox potential was found to decrease linearly as the pKa of the corresponding benzoic acid increased. It is worth noting that the redox potential varied with both the number and the position of the fluorine atoms on the aromatic ring, and the influence of position on the Ru_2 redox properties followed the trend *meta<ortho<para*. The authors also note a loose correlation between the dihedral angle defined by the plane of the aromatic group and the plane of the diruthenium unit and agreement with the pKa vs $\Delta E_{1/2}$ line of best fit. This suggests that steric constraints pushing the aromatic ring out of plane may subtly influence redox properties, although this effect is lessened in the solution state where the aromatic rings have much more rotational freedom. Also of interest was the observation that in several of the examples, the potential for the $Ru_2^{4+/5+}$ redox couple was pushed high enough that these normally air-sensitive complexes became tolerant to atmospheric oxygen in the short to medium term.

Overall, it appears that alteration of the ligand donor atoms leads to substantial changes in the properties of paddlewheel complexes. The redox potential of the M_2 centre may span almost

1 V, due to changes in the δ energy level. Furthermore, the electronic structure and spectroscopic properties may also be strongly affected. For instance, for N-donor formamidinate ligands the HOMO-LUMO transition corresponds to δ-δ*, but for some O or S donor ligands, the π system lies closer in energy to the δ orbitals and the LUMO is instead ligand π* in nature, and the HOMO-LUMO transition is an MLCT process. Perhaps unsurprisingly, remote substitution has a more subtle effect on the properties at the dimetal core, with relatively little effect on the spectroscopic properties,[28] but still provides a broad window to tune redox properties, even to the point of improving the air-stability of these complexes.

Porphyrins

Porphyrins have garnered extraordinary research interest in recent years owing to their high stability, low cost, and interesting photophysical and optical properties.[33] The basic structure of a porphyrin consists of four pyrrole rings linked together in an aromatic macrocycle (**Figure 12)**, however there is remarkable synthetic versatility when functionalizing at both the *meso* and β- positions of porphyrins, and the incorporation of differing functional groups may be used to tune the levels and spectroscopic properties of the porphyrin.[34]

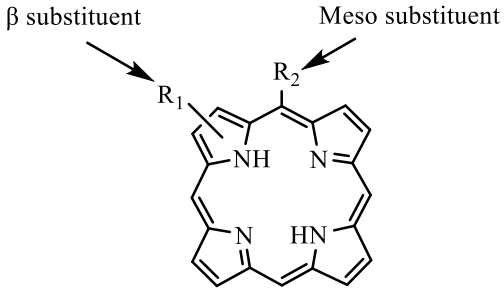

Figure 12: Chemical structure of porphine, the simplest porphyrin, with labelled substitutional positions

The absorption spectrum of a porphyrin typically consists of an intense Soret band around 400 nm and less intense Q-bands between 500 and 600 nm (**Figure 13**). Both of these originate from electronic transitions within the porphyrin π system, in the case of the Soret band $a_{1u}(\pi) \rightarrow e_g^*(\pi)$, for the Q-bands $a_{2u}(\pi) \rightarrow e_g^*(\pi)$.[35] When the central porphyrin cavity is occupied by a metal, the symmetry of the porphyrin is increased and the number of Q-bands is reduced, usually to one or two.[35] Porphyrins may also be both oxidised and reduced, exhibiting 2 successive 1-electron reductions and 2 1-electron oxidations. The gap (in volts), between the first oxidation and reduction may be used to determine the HOMO-LUMO gap in porphyrins,[36] and the position of each redox couple may be tuned by both the metal in the central cavity or by peripheral substituents (R_1/R_2 in **Figure 12**). An example of the effect of *meso*-substitution is shown in **Figure 14** (porphyrin structures are depicted in **Figure 15**), where more electron

withdrawing substituents shift both reductions and oxidations to higher potentials.[37] The combination of photophysical and redox properties in porphyrins have led to their use in a variety of photochemical applications, ranging from photodynamic therapy,[38,39] to liquid crystal arrays for electronic devices[40,41] to molecular wires.[42] Of particular interest to this project is the extensive research towards porphyrins for photocatalysis[43] and photovoltaics,[44] for example as sensitizers for dye-sensitized solar cells (DSSCs).[45,46] For these applications, asymmetric porphyrins are generally used to help drive charge extraction from the excited state, for example the push-pull dye depicted in **Figure 16**.[47] In this case, the tertiary amine groups act as electron donors, and the carboxylic acid groups electron acceptors. This push-pull effect leads to spatial separation of the HOMO and LUMO, which in turn brings about greater separation of electrons and holes in the excited state, promoting charge extraction into an external circuit. In this example, alkyne spacers have been incorporated to ensure the electron-donating amine groups are in-plane with the porphyrin π system allowing for optimal orbital overlap between components of the dye. Porphyrins have proven successful within this sphere, and donor-acceptor porphyrin based systems have reached solar efficiencies as high as 13%, comparable to more traditional ruthenium based dyes.[48] Indeed, donor-acceptor systems have become common motifs in the applications of porphyrins, for example the porphyrin/fullerene dyad depicted in **Figure 17**, where the porphyrin unit itself acts as a donor due to its electron-rich π system, and the fullerene as a powerful electron acceptor. This example molecule was prepared with a view to creating supramolecular arrays for use as molecular wires,[42] but potential applications of similar dyads also include the aforementioned solar harvesting and catalysis, occasionally arranged as a monolayer on a gold surface.[49]

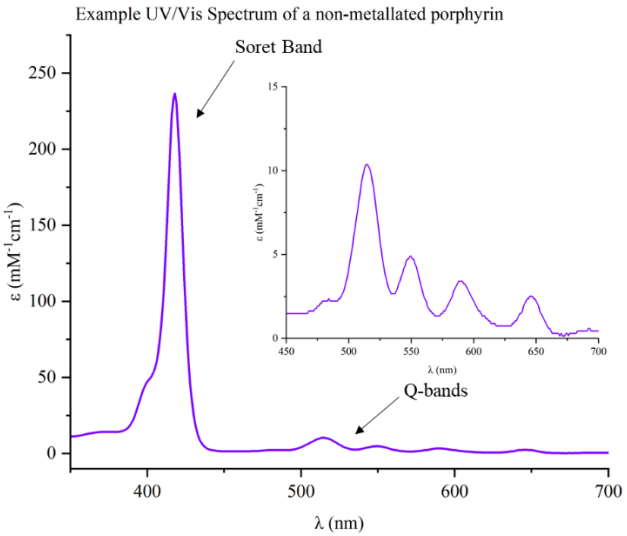

Figure 13: UV/Vis spectrum of an example porphyrin (triphenylmonocarboxyphenylporphyrin) (0.0068 mM in THF, 298 K). Data collected by Imogen Walsh

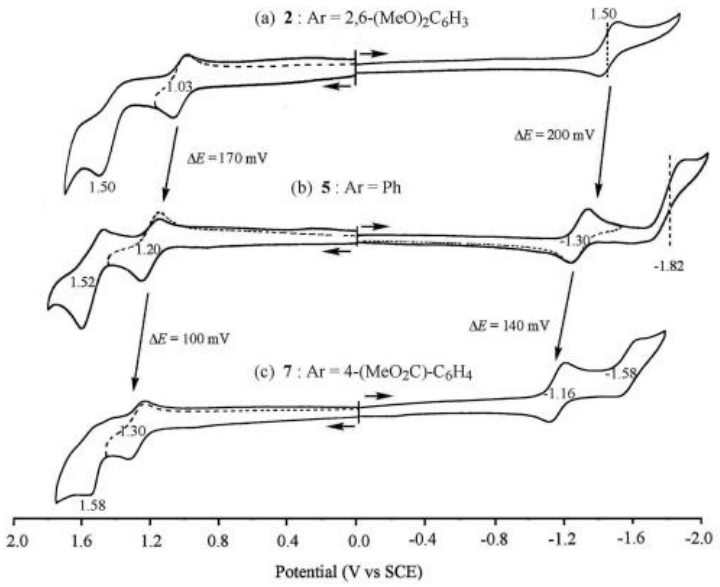

Figure 14: Cyclic voltammograms showing the redox properties of example (Pt) porphyrins. (**a**) aryl *meso*-substituents are 2,6-$(MeO)_2C_6H_5$, (**b**) aryl *meso*-substituents are Ph, (**c**) aryl *meso*-substituents are 4-$(MeO_2C)C_6H_5$. Reproduced with permission from ACS.[37]

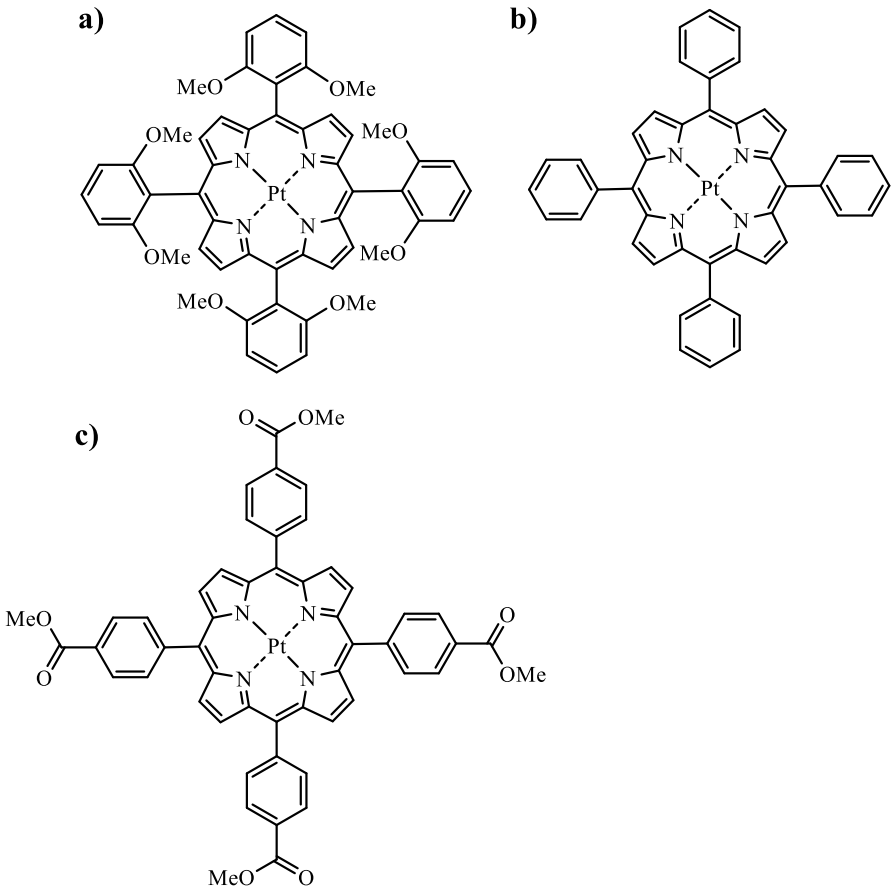

Figure 15: Example (Pt) porphyrins **a-c** from Figure 14

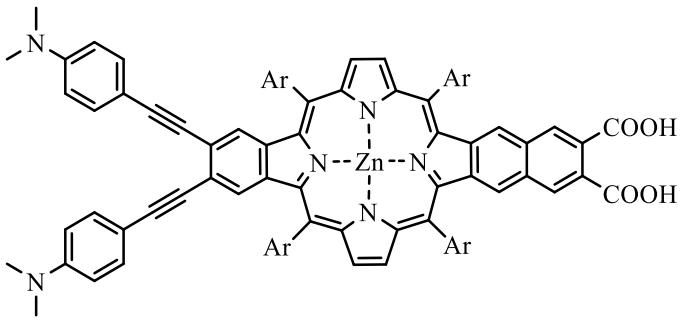

Figure 16: Example push-pull porphyrin for use in DSSCs[47]

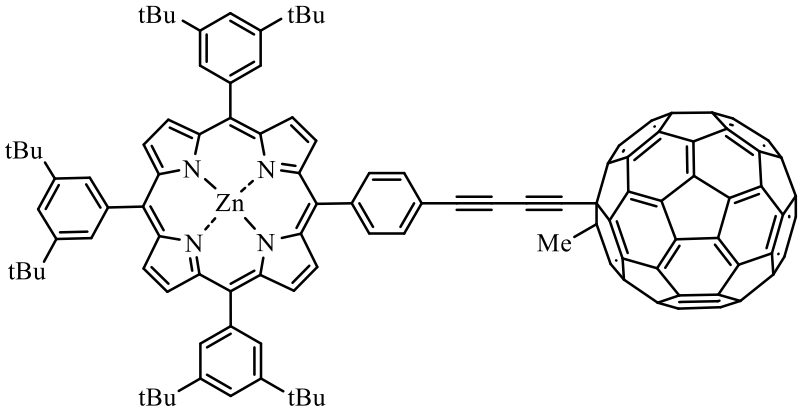

Figure 17: Example porphyrin/fullerene donor-acceptor system[42]

A brief note on porphyrin nomenclature: porphyrins with differing *meso*-substituents are generally referred to by the ABCD system, where A, B, C and D represent discrete groups.[50] For instance, **Figure 18**, left would be termed an ABCD porphyrin, **Figure 18**, centre, *cis*-A_2B_2 porphyrin, and **Figure 18**, right, *cis*-A_2BC porphyrin. This nomenclature is used throughout the report.

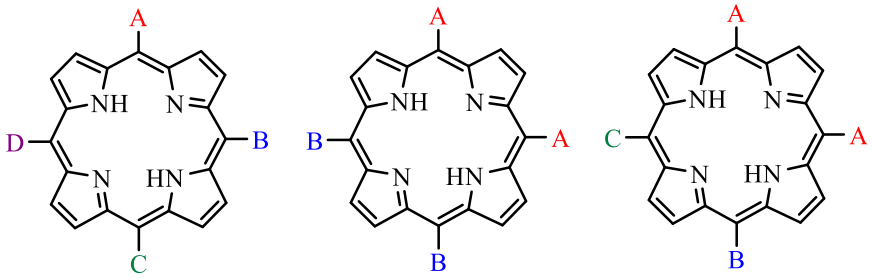

Figure 18: Examples of ABCD-type meso substituted porphyrins

Meso-substituted porphyrins can be made by one-pot, mixed condensation reactions, refluxing a mixture of pyrrole, dipyrromethanes, and functionalized aldehydes.[51,52] One popular method to achieve this was developed by Alder and Longo in 1967, conducting the reaction in propionic

acid (**Figure 19**).[53] This is a swift and inexpensive route to porphyrins, however the lack of control afforded by the one-pot process leads to the formation of a statistical mixture of porphyrin products, which can be lengthy and difficult to separate, These are also low yielding reactions, typically 10-12% due to the formation of polypyrroles as the entropically favoured product.

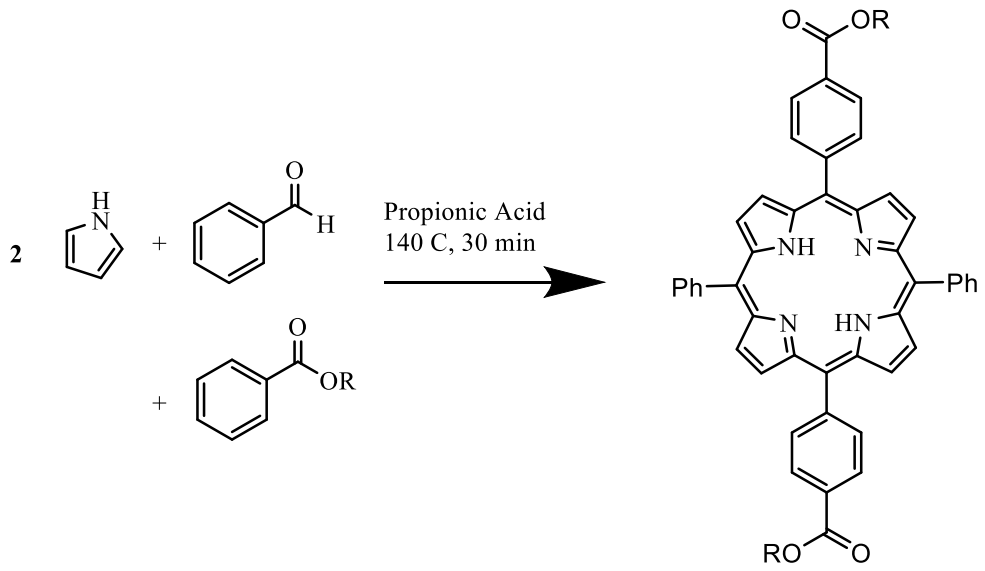

Figure 19: Alder-Longo method for mixed condensation porphyrin synthesis[53]

Through use of low concentration solutions in DCM and an oxidising agent (*p*-chloranil or 2,3-dichloro-5,6-dicyano-1,4-benzoquinone, DDQ), Lindsey developed a mixed condensation synthesis that produces *meso*-substituted porphyrins in yields of up to 55%, and further to this, reaction conditions have been developed that minimise scrambling of the substituents (**Figure 20**).[54,55] However, the volume of solvent required to produce the low concentration solutions (10^{-2} M) for these reactions may become prohibitive when preparing porphyrins in bulk. Both methods can be effective for the preparation of simple A_4 or A_3B type porphyrins, but other synthetic pathways may be more appropriate for more complex, asymmetric ABCD systems.

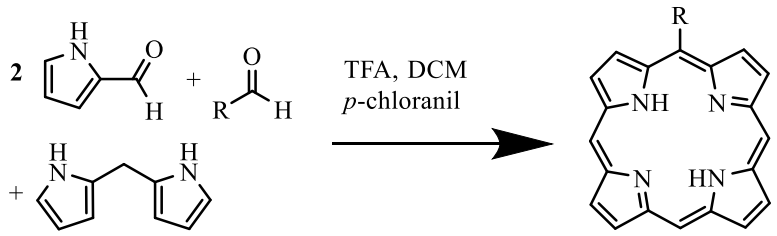

Figure 20: Lindsey method for mixed condensation porphyrin synthesis[54]

"Total" synthesis of specific porphyrin derivatives may also be achieved from a non-cyclic precursor by ring closure followed by oxidation to the porphyrin. However, this is not a favoured approach due to the high number of synthetic steps required.[56] Porphine itself may be synthesised in one step at 60% yield by acid catalysed dealkylation of tetra(*tert*-butyl) porphyrins,[57] and may then be subsequently functionalised by the addition of alkyl lithium reagents at the meso position, followed by oxidation to the porphyrin with DDQ.[58] An alternative approach to functionalize porphine is to brominate at the meso position (different reagents and conditions give varying levels of substitution), followed by a Pd-catalysed cross-coupling to attach the desired functional group to the porphyrin periphery.[59–61] By these methods a wide range of functional groups may be integrated into the porphyrin derivative. These may be used either to modify the solubility of the porphyrin, or to introduce additional functionality to the molecule. These steps tend to be relatively high yield compared to the mixed condensation process, (40-70% in the case of the alkyl lithium addition),[33] but owing to more harsh conditions and expensive reagents, they may only be worthwhile for specific derivatives unobtainable by mixed condensation.

Paddlewheels and Porphyrins

There are already a great many publications where paddlewheel complexes are combined with porphyrins in the context of metal organic frameworks (MOFs).[62] These usually take the form of 2D grid sheet structures (pillared 3D structures also exist), where A_4 type porphyrin tetracarboxylates are linked to tetrasubstituted paddlewheel complexes in an alternating structure (**Figure 21**).[62] These have been explored for a variety of applications, including as photocatalysts,[63] electrodes in nanodevices,[64] carbon capture technologies,[65] and solar harvesting.[66,67] However, these examples are primarily concerned with the properties of the porphyrins, and the paddlewheel building blocks, usually the redox inactive $Zn_2(OAc)_4$ but sometimes $Co_2(OAc)_4$, serve largely as structural components to bind porphyrin units together in a highly ordered manner. There is a solitary example in the literature of a dirhodium paddlewheel/porphyrin 2d array, which does exhibit electronic coupling, observed as an intramolecular charge transfer band from porphyrin to paddlewheel.[68] The potential for such materials as photocatalysts is merely noted however, and no follow-up publication currently exists. Whilst these examples do not explore the redox or photochemical capabilities of paddlewheel complexes, they do demonstrate the potential for expanding simple paddlewheel-porphyrin conjugates into supramolecular arrays, and that synthetic procedures to achieve this are already in existence.

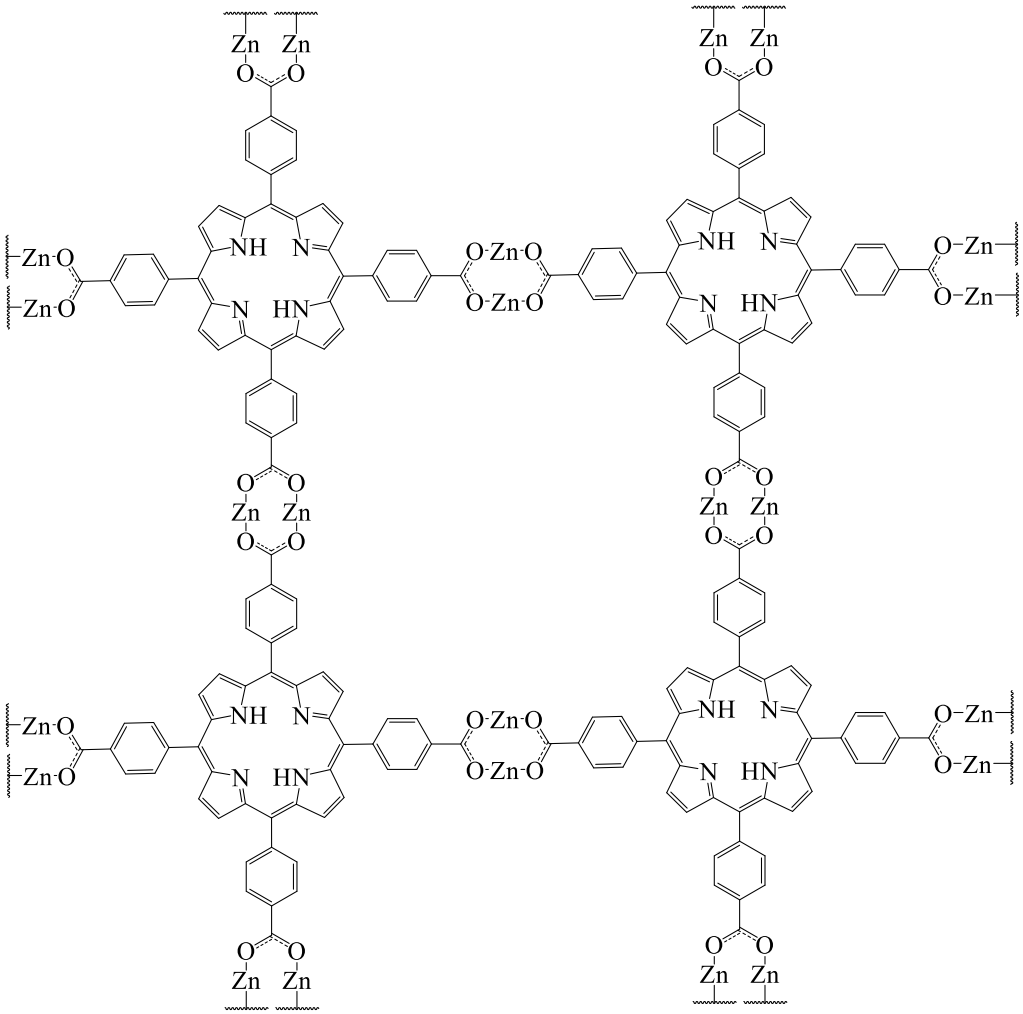

Figure 21: Example structure of a paddlewheel-porphyrin 2D MOF. Paddlewheel ancillary ligands are omitted for clarity

To the author's knowledge, there is currently only one example in the literature where molybdenum paddlewheel complexes are electronically coupled to porphyrins in a single molecule, published in 2021. The Liu Group prepared a single-molecule quadruply bonded Mo_2 paddlewheel complex tethered to a zinc-centred porphyrin, which acts as a photocatalyst for the reduction of water to H_2, and the reduction of NAD^+ to NADH (**Figure 22**).[69]

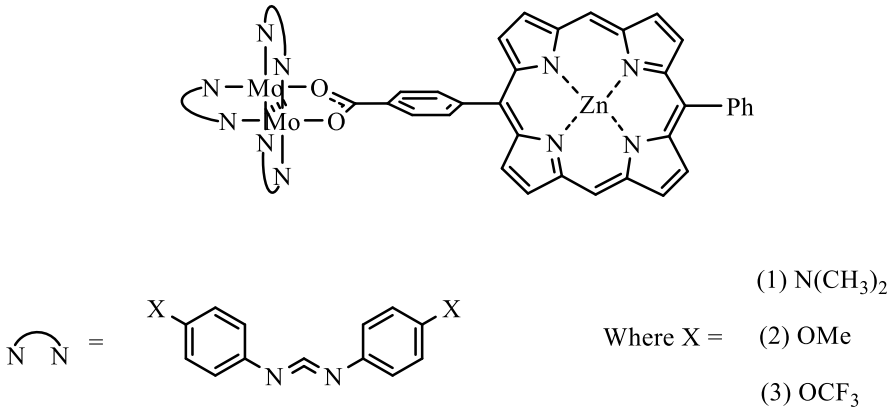

Figure 22: Single molecule paddlewheel-porphyrin conjugates investigated by the Liu group[69]

Here, the paddlewheel component acts as photosensitizer, whereby upon light absorption an electron is promoted from the M_2 δ to the M_2 δ* orbital, followed by charge transfer into the porphyrin π* system. This is an unusual situation given that it is usually the porphyrin that acts as the photosensitizer in similar systems, such as the complex depicted in **Figure 23** from the group of Robin Perutz where porphyrin Q-band absorption is followed by (through space) charge transfer to a covalently tethered rhenium complex- activating the complex for the reduction of CO_2 to CO.[70]

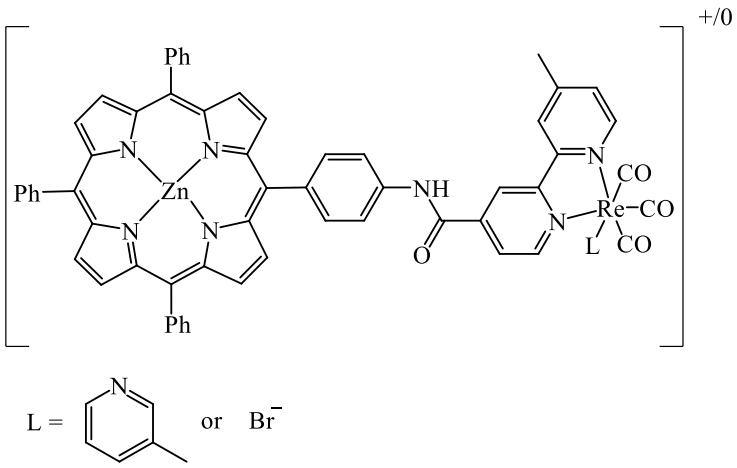

Figure 23: Porphyrin-rhenium dyad where the porphyrin acts as a photosensitizer[70]

Redox activity in this paddlewheel-porphyrin dyad takes place either on the porphyrin metal centre or the ring itself. This system achieves turnover numbers of up to 640, well short of current systems based on precious metals (which achieve turnovers up to 10^5),[71] but greatly exceeds the performance of either the paddlewheel or porphyrin in isolation. Steady state UV/Vis spectroscopy suggests that the redox process proceeds via a Mo_2-Ph-chlorin

intermediate as the porphyrin bands decrease as the reaction proceeds. The authors put forth that the porphyrin takes up four electrons and two protons in a stepwise manner.

It is also worth noting that the photoinduced charge transfer from paddlewheel to porphyrin takes place even although DFT calculations suggest that the porphyrin is twisted out of plane with the Mo_2 quadruple bond by around 60°, as loss of planarity in the bridging ligand has been shown to dramatically reduce electronic coupling in mixed valence systems. The $Mo_2^{4+/5+}$ redox couple was shown to remain essentially unchanged by porphyrin attachment, providing further evidence of only weak electronic coupling between the two components. Despite this, the structure of the paddlewheel was found to affect the catalytic output of the molecule, which performed most effectively with electron donating $N(CH_3)_2$ groups appended to the formamidinate ancillary ligands relative to both OMe, and the electron withdrawing CF_3 group. It is suggested that this is due to fine tuning of the Mo_2 δ energy level and illustrates that these complexes may be tailored to optimise the properties for a specific application. Whilst the catalytic output does not match current technologies with precious metals, this nonetheless showcases the potential of paddlewheel-porphyrin conjugates, and it will be of interest to explore these concepts further with a wider range of complexes.

Project Aims:

This project shall incorporate two streams. The first will be the synthesis and characterisation of paddlewheel-porphyrin conjugates. Starting from the simplest possible paddlewheel-porphyrin dyad (**Figure 24**, **i**), synthesis and work-up conditions shall be optimized to produce paddlewheel-porphyrin conjugates cleanly and with the highest yields practicable. From there, syntheses of more complex architectures will be developed, for instance complexes with multiple porphyrins surrounding a central paddlewheel unit (**Figure 24 ii**), or the reverse situation where multiple paddlewheels append a central porphyrin (**Figure 24 iii**). These compounds shall subsequently be characterised, initially by CV and UV/Vis spectroscopy to explore their redox and spectroscopic properties and probe the structure-property relationships between the different paddlewheel-porphyrin conjugates in the family. Of particular interest is the electronic communication between paddlewheel and porphyrin – i.e. the extent to which the Mo_2 δ orbitals overlap with the porphyrin π system. In complexes with multiple paddlewheel units, there is also the potential for interaction between multiple Mo_2 units mediated by the porphyrin bridge, which could give rise to mixed valence characteristics. Laboratory work shall be supplemented by computational chemistry employing DFT calculations to support and build upon these results. The properties of these conjugates shall be investigated with a view to exploring their suitability for photovoltaic applications or in molecular electronics by evaluating electronic communication, either electrochemically or spectroscopically, between the two components.

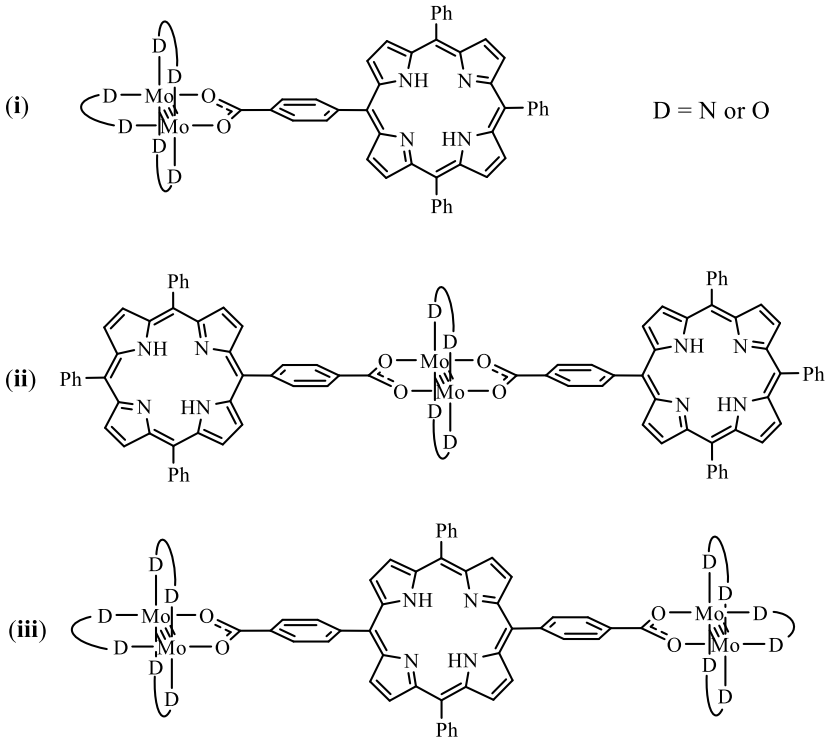

Figure 24: Examples of paddlewheel-porphyrin conjugates; diad (**i),** and triads (**ii**) and (**iii**).

Parallel to this, an avenue of research will be undertaken to examine the effects of ligand-based fluorination on homoleptic paddlewheel complexes (**Figure 25**). This shall first consist of optimizing a synthetic procedure to produce these complexes cleanly and in high yields. These complexes will then be characterised by X-ray diffraction (XRD), cyclic voltammetry and UV/Vis spectroscopy to investigate the effect that the fluorine substitution patterns have on the redox properties, electronic structure, and spectroscopic properties of the complexes. There is some evidence that fluorination can improve air-stability in similar systems[27,32] and furthermore, tuning of the energy levels of the frontier orbitals may be an invaluable tool to help improve electronic communication when paddlewheel units are covalently tethered to porphyrins.

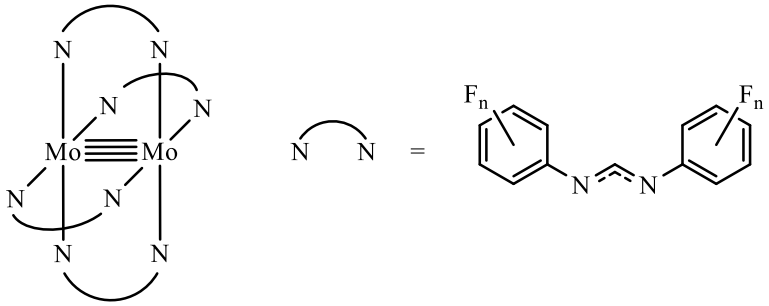

Figure 25: General structure of homoleptic fluorinated paddlewheels

Results and Discussion

Porphyrin Synthesis

The porphyrins used throughout this project were prepared using the Adler-Longo mixed condensation method (**Figure 26**).[53] The result of this process was a mixture of porphyrin products, including A_4Porphyrin, A_3BPorphyrin, *cis/trans*-A_2B_2Porphyrin (where A = phenyl and B = 4-(methyl)benzoate), alongside a mixture of poly-pyrroles. The crude product was washed with ethanol, and the different porphyrins separated by silica gel chromatography with a DCM mobile phase. A_3BPorphyrin had a high R_f value of around 0.8 and could be separated from other porphyrin isomers quickly and with relative ease. *Trans*-A_2B_2Porphyrin had a very similar R_f value (around 0.45) to *cis*-A_2B_2Porphyrin (R_f 0.40) and the two proved difficult and lengthy to separate. Best results were achieved with long, wide columns (**Figure 27**) and without the use of compressed air/bellows to hasten elution. Full separation often required multiple columns. Each porphyrin was isolated as a dark purple powder and was characterised by ESI-MS and ^{1}H NMR spectroscopy (chloroform-*d*), and the data for each matched values found for these compounds in the literature.[72]

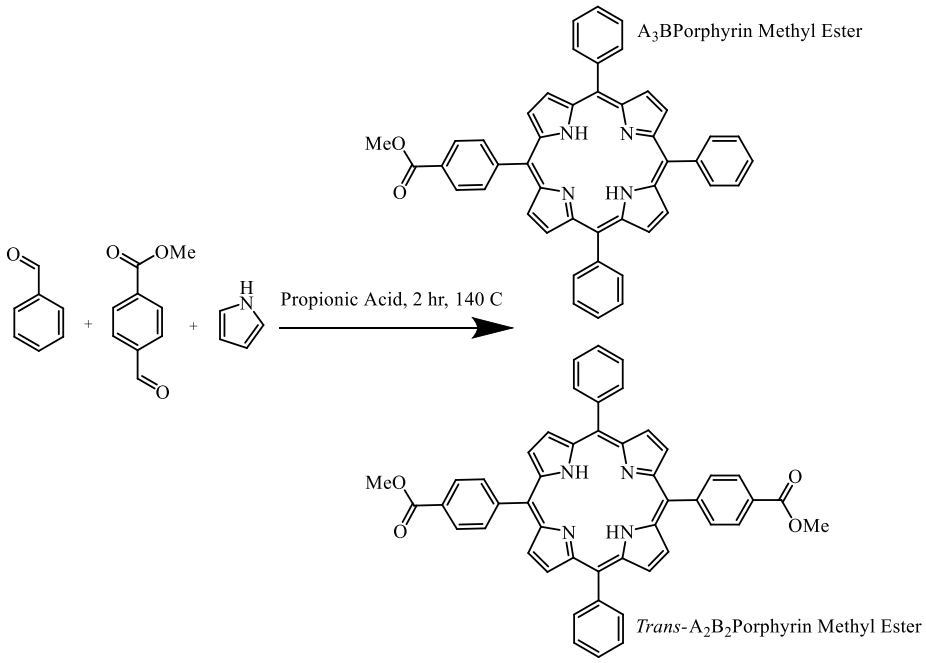

Figure 26: Reaction scheme for mixed condensation porphyrin synthesis

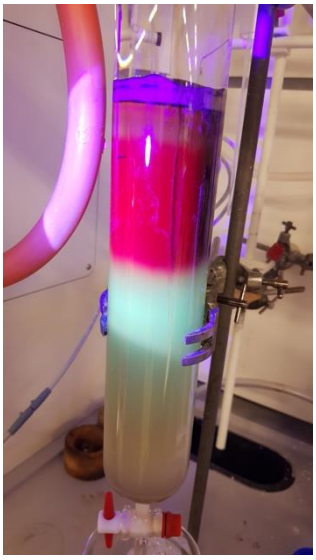

Figure 27: Example column separating porphyrin isomers with silica stationary phase and DCM mobile phase

Once isolated, the ester moieties were converted to their respective carboxylic acids by NaOH mediated ester hydrolysis (**Figure 28**). Best results were obtained by re-acidifying the solution to pH 3, then selectively removing the THF by rotary evaporation, causing the water-insoluble porphyrin product to fully precipitate, whereupon it could be collected by filtration.

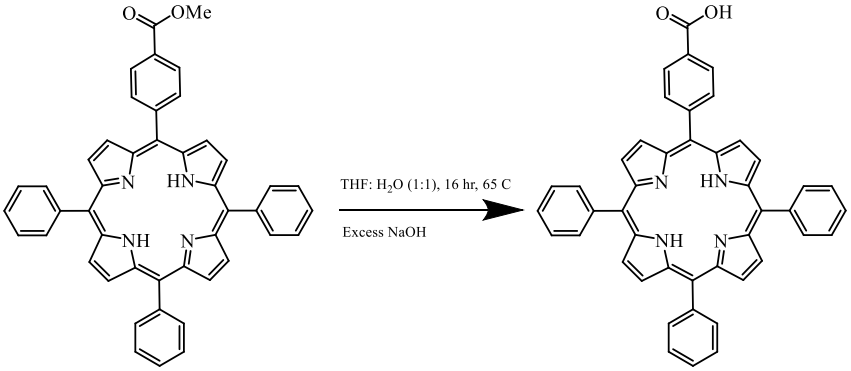

Figure 28: Base mediated ester hydrolysis of an example A_3BPorphyrin

Paddlewheel-Porphyrin Conjugate Synthesis

In designing a synthetic pathway towards the desired Mo_2 paddlewheel-porphyrin complexes, care must be taken over the choice of ancillary ligands as they have been shown in many cases to be non-innocent.[1] Carboxylates tend to be more labile than various NN or ON donor ligands, and substituents on the ligands have been shown to have a strong influence on the

optoelectronic properties of the Mo_2 core.[26] The paddlewheel-porphyrin conjugates synthesised in this investigation proceed via substitution of a labile ligand on a pre-prepared starting paddlewheel with a carboxyphenylporphyrin. Two different sets of ancillary ligands are investigated herein, the carboxylate based TiPB ligand (2,4,6-triisopropylbenzoate), and the formamidinate based DAniF ligand (N,N'-di(4-anisyl)formamidinate) (**Figure 29**).

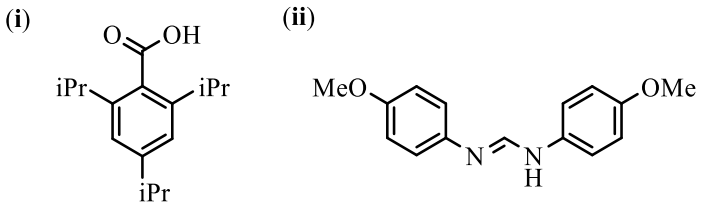

Figure 29: Structure of (**i**) HTiPB, (**ii**) HDAniF

TiPB Systems

Investigative Synthesis

Early investigative work favoured $TiPB^-$ as an ancillary ligand system, as the steric bulk improves solubility and helps protect the axial position from unwanted coordination. Additionally, the natural lability of $TiPB^-$ allowed for direct ligand substitution with a carboxyphenylporphyrin. This, coupled with the facile preparation of the homoleptic starting material $Mo_2(TiPB)_4$ (**Figure 30**) served as a convenient starting point for the project.

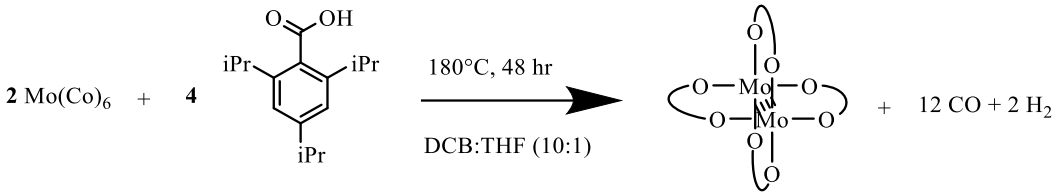

Figure 30: Reaction scheme for $Mo_2(TiPB)_4$

As a proof-of-concept reaction, the simplest paddlewheel-porphyrin conjugate was pursued (**Figure 31**), compound (**1**), consisting of one paddlewheel complex linked to one porphyrin unit via a carboxyphenyl linker. Product formation was achieved through a simple ligand exchange of a labile $TiPB^-$ unit for a carboxyphenylporphyrin, facilitated here by a base (NaOMe). The crude product was washed with hexane and filtered through celite to remove impurities. A sticky brown solid was isolated (20% yield) and analysed by ^1H NMR spectroscopy (chloroform-*d*) (**Figure 32**).

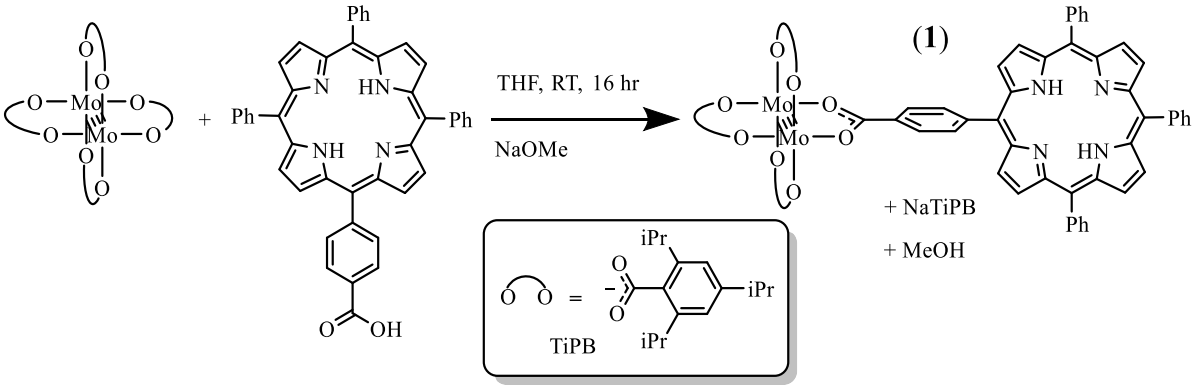

Figure 31: Reaction scheme for $Mo_2(TiPB)_3(A_3BPorphyrin)$ (**1**)

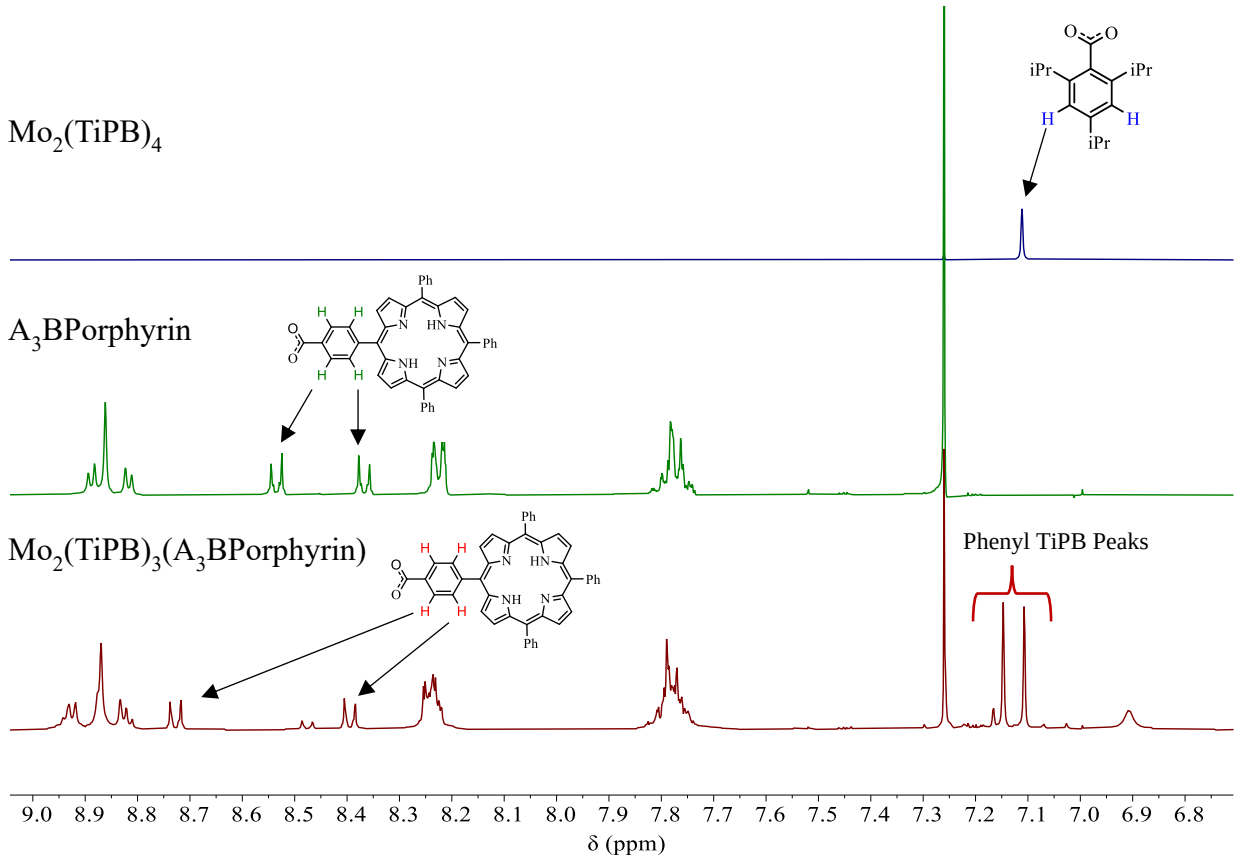

Figure 32: The aromatic region of the ^{1}H NMR spectrum (chloroform-*d*) of the reaction product displaying a mix of $Mo_2(TiPB)_3(A_3BPorphyrin)$ (**1**) and potentially $Mo_2(TiPB)_2(A_3BPorphyrin)_2$ (**2**)

The phenyl protons on the ancillary TiPB ligands are a useful tool for understanding this spectrum as they are well resolved and away from other peaks. In the homoleptic starting material, $Mo_2(TiPB)_4$, this peak appears as a singlet at 7.11 ppm. In the monosubstituted product, $Mo_2(TiPB)_3(A_3BPorphryin)$ (compound **1**), this peak was expected to split into two

singlets in a 2:1 ratio, corresponding to the *cis*- and *trans*- TiPB units respectively. However, this was not observed, and instead, 3 singlets were observed in a 1:5:5 ratio. The singlet at 7.11 ppm possibly corresponds to unreacted starting material, but regardless, the splitting pattern observed is not consistent with either compound **1**, nor the over-substituted *trans*-$Mo_2(TiPB)_2(A_3BPorphyrin)_2$ conjugate (compound **2**) known to be a thermodynamic sink in similar systems which would produce one singlet.[73] This suggested that a mixture of products had been formed, most likely a combination of (**1**) and (**2**). The carboxyphenyl protons on the A_3B porphyrin (labelled green in **Figure 32**) were the only porphyrin signals to be shifted in the product and moved downfield from 8.30 and 8.45 ppm to 8.40 and 8.75 ppm. The absence of the doublets at 8.30 and 8.45 ppm indicated there was no residual free-base porphyrin in the product, and the additional doublet at around 8.5 ppm further supported the argument that a mixture of products may have been formed. *Vide infra* for discussion of the broad singlet at around 6.9 ppm. Overall, the shifts in certain diagnostic peaks along with a dearth of free HTiPB decomposition products were encouragement that with the right reaction conditions and work-up procedure, isolation of the product may be possible.

MALDI-TOF-MS, the preferred (and often essential) mass spectrometry technique for Mo_2 paddlewheel complexes was unavailable at the time, and so samples were instead submitted for ESI and APCI MS. Neither technique yielded any molybdenum-based signals.

Following on from concerns that $Mo_2(TiPB)_4$ may have over-substituted to give a mixture of products, and knowing that a trans-bis-bis configuration is often a thermodynamic sink,[74] the stoichiometry of the reaction was altered, adding two equivalents of porphyrin to see if *trans*-$Mo_2(TiPB)_2(A_3BPorphyrin)_2$ (**Figure 33**, compound **2**) could be produced cleanly.

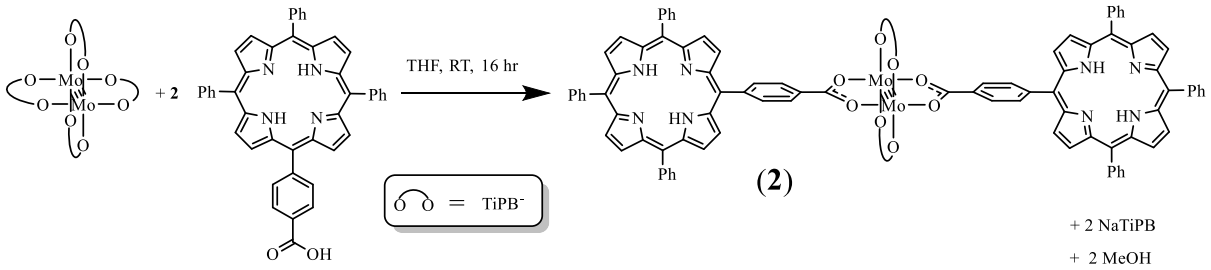

Figure 33: Reaction scheme for *trans*-$Mo_2(TiPB)_2(A_3BPorphyrin)_2$ (**2**)

The *cis*- analogue of this conjugate, *cis*-$Mo_2(TiPB)_2(A_3BPorphyrin)_2$ was also prepared, but because the *trans* effect drives substitution of $Mo_2(TiPB)_4$ with A_3BPorphyrin to the *trans*-isomer, an indirect synthetic route was taken instead. $Mo_2(TiPB)_4$ was stirred overnight in a solution of acetonitrile (a less *trans* directing ligand than TiPB) with an excess of $[Et_3O][BF_4]$ to yield the intermediate salt *cis*-$[Mo_2(TiPB)_2(NCMe)_4][BF_4]_2$ (**Figure 34**, compound **3**).[75] This salt was washed with diethyl ether to extract excess $[Et_3O][BF_4]$ and EtTiPB, isolating **3** as a purple powder in 48% yield.

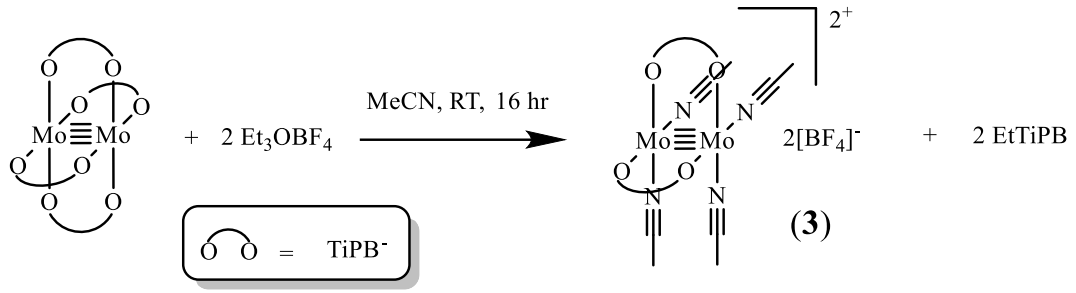

Figure 34: Preparation of intermediate [*cis*-$Mo_2(TiPB)_2(NCMe)_4]^{2+}$ (**3**)

The intermediate complex was subsequently stirred with 2 equivalents of A_3B Porphyrin to displace the labile, monodentate acetonitrile ligands to yield the final product (**Figure 35**, **4**). A dark brown powder was obtained from this reaction, but neither ^1H NMR nor MALDI-TOF-MS were able to confirm the presence of the desired complex **(4)**.

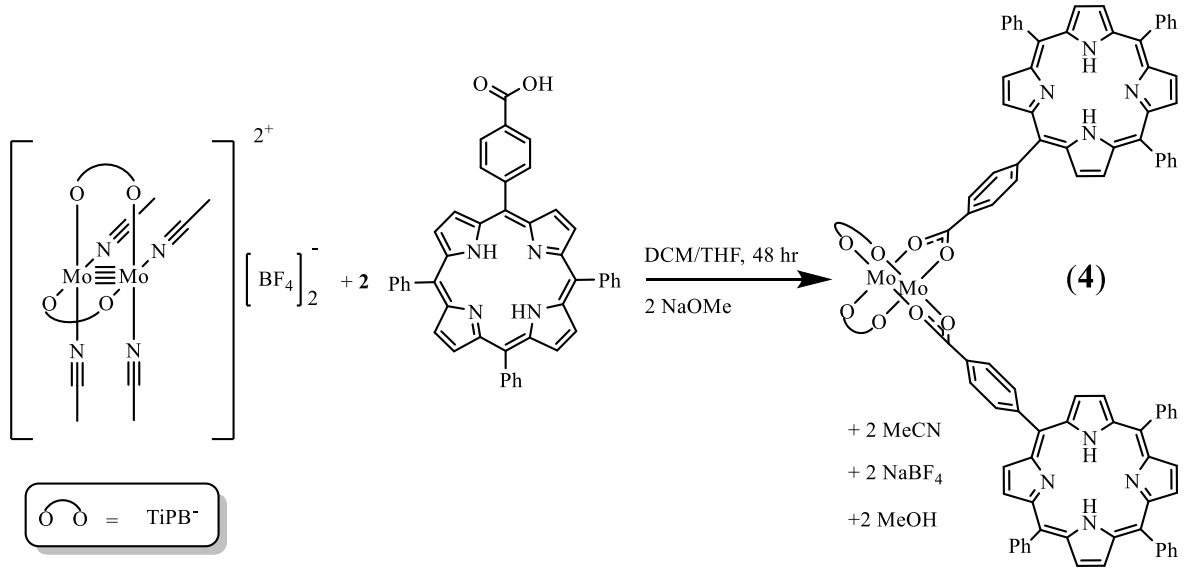

Figure 35: Reaction scheme for *cis*-$Mo_2(TiPB)_2(A_3BPorphyrin)_2$ (**4**) from intermediate MeCN complex

By starting from porphyrins with two or more carboxylate linker units, an alternative set of paddlewheel-porphyrin conjugates with central bridging porphyrin units is also synthetically accessible. The simplest example is depicted in **Figure 36**, where a *trans*-A_2B_2Porphyrin was stirred with $Mo_2(TiPB)_4$ in THF for 56 hr. The ligand substitution process is essentially the same as previously described, but the result in this case is a disubstituted complex with a bridging porphyrin. A summary of the investigative work carried out on this set of reactions is outlined in **Table 1**.

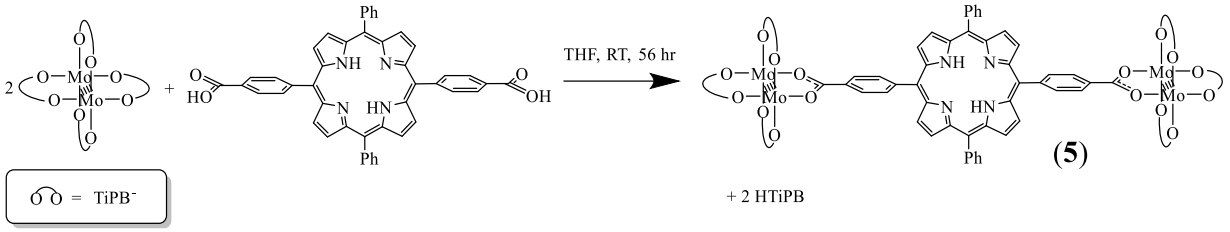

Figure 36: Reaction scheme for $[Mo_2(TiPB)_3]_2$(μ-*trans*-A_2B_2Porphyrin) (**5**)

Table 1: Investigative synthesis of paddlewheel-porphyrin conjugates with TiPB ancillary ligands (* NaOMe added)

Reaction	Mo_2 Starting Material	Porphyrin Starting Material	Mo_2: Porphyrin Ratio	Time (hr)	Solvent	Wash Solvent	% Yield	Description
A	$Mo_2(TiPB)_4$	A_3B	1:1	48	THF*	Hexane	20	Greasy brown solid
B	$Mo_2(TiPB)_4$	A_3B	1:2	48	THF	Hexane	17	Greasy dark brown powder
C	$Mo_2(TiPB)_4$	A_3B	1:2	16	THF	Diethyl ether	76	Flaky purple powder
D	$Mo_2(TiPB)_4$	A_3B	1:2	48	Toluene	Diethyl ether	58	Purple/brown powder
E	[*cis*-$Mo_2(TiPB)_2(MeCN)_4]^{2+}[BF_4]^-_2$	A_3B	1:2	48	DCM/ THF*	Diethyl ether	-	Dark brown powder
F	$Mo_2(TiPB)_4$	*Trans*-A_2B_2	2:1	56	THF	Toluene	-	-

Several improvements to the synthetic procedure were made over the course of this investigation. For instance, it was discovered that the TiPB ligands were sufficiently labile that NaOMe was not required to facilitate ligand substitution. This in turn simplified the work-up procedure as sodium salts no longer needed to be separated from the products. Diethyl ether was found to be a superior alternative to hexane as a washing solvent, as it more effectively removed both free-base porphyrin and free HTiPB whilst leaving the intended products behind. Consequentially, the isolated products were much less greasy and easier to work with. Except for the synthesis of (**5**) (reaction **F**) the full 48 hr was not required- 16 hr was sufficient for starting material consumption and this in conjunction with diethyl ether washes resulted in much higher yields.

The ^{1}H NMR spectrum (chloroform-*d*) of the mono-substituted species $Mo_2(TiPB)_3(A_3BPorphyrin)$ has already been depicted in **Figure 32** and the salient features discussed. In summary, a mixture of products were visible and it was thought that the complex had over-substituted to give a mixture of the intended mono-substituted product (**1**) and the *trans*-bis-substituted product (**2**).

In subsequent samples complex **2** was targeted deliberately with a view to isolating an analytically pure product. However, the low solubility of the product in chloroform-*d* hindered ^{1}H NMR analysis as the sample precipitated in the NMR tube resulting in poor quality spectra. Pyridine-d_5 was investigated as an alternative NMR solvent as these complexes were found to be more soluble in polar aromatic solvents. However, the spectra were still poorly resolved, and the solvent signals overlapped with key product peaks in the aromatic region, hindering interpretation. Additionally, there are examples of paddlewheel-pyridine adducts with pyridine coordinated at the axial site, partially displacing the bridging carboxylate ligands on the paddlewheel. Thus, pyridine-d_5 may actually catalyse the breakdown of the product.[1] Rather than change the NMR solvent system entirely, it was found that *trans*-$Mo_2(TiPB)_2(A_3BPorphyrin)_2$ could be solubilised in chloroform-*d* by addition of a few drops of THF. The THF peaks in the ^{1}H NMR spectrum were large and obscured the TiPB alkyl signals, but the porphyrin peaks and the diagnostic aromatic TiPB peaks in the region 7-8 ppm were visible and reasonably well resolved upon magnification (**Figure 37**).

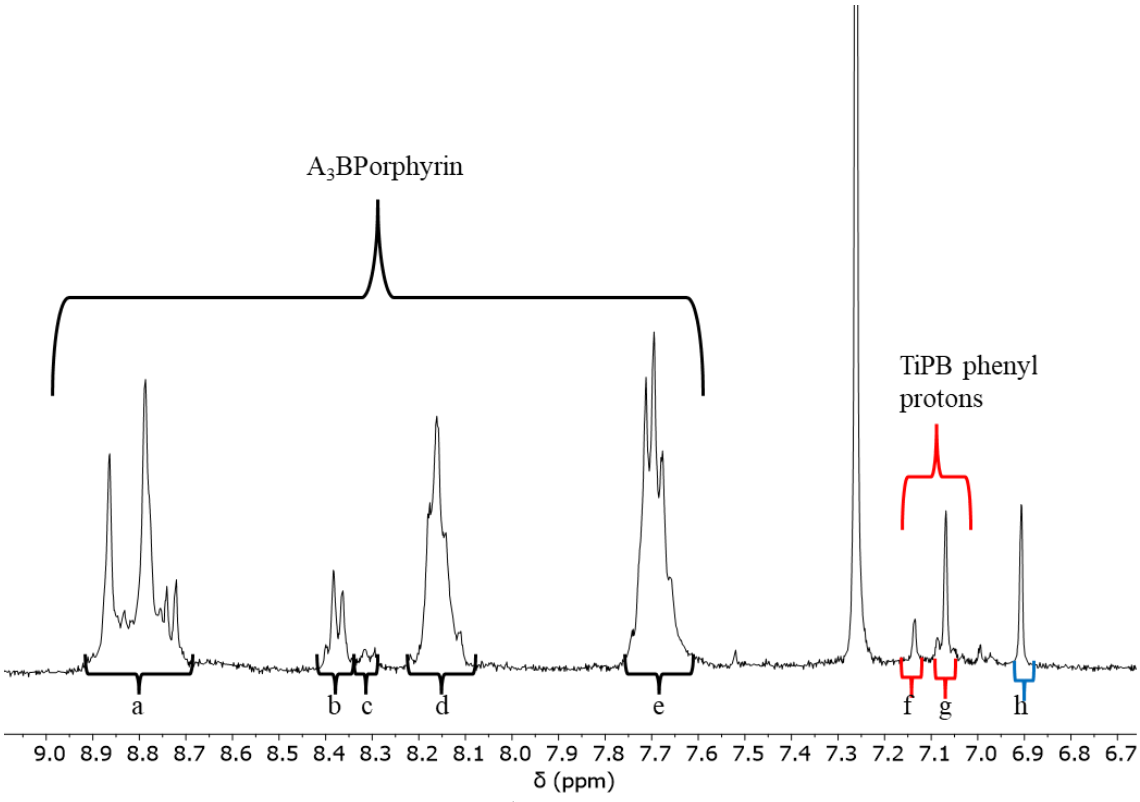

Figure 37: The aromatic region of the ^{1}H NMR spectrum (chloroform-*d* + THF-H_8) of *trans*-$Mo_2(TiPB)_2(A_3BPorphyrin)_2$, (**2**), reaction **C** in **Table 1**

Initially, it was thought that signals **f** and **g** corresponded to phenyl TiPB protons in compounds **1** and **2**. If this was the situation 3 peaks should be present; *cis*- and *trans*- peaks for $Mo_2(TiPB)_3(A_3BPorphyrin)$, and one signal for *trans*-$Mo_2(TiPB)_2(A_3BPorphyrin)_2$, although it is possible that one of these may be obscured by the larger of the two signals. However, this interpretation was unable to explain the overly large porphyrin-based signals (**Table 2**, **a**, **d** and **e**), nor the identity of peak **h** at around 6.9 ppm.

Once MALDI-TOF-MS became available for product analysis, the sample was characterised by mass spectrometry (dithranol matrix, THF solution). The spectrum is shown in **Figure 38** and the major peaks are summarized in **Table 3**

Table 2: ^{1}H NMR integrals for $Mo_2(TiPB)_2(A_3BPorphyrin)_2$

NMR signal	Expected Integral	Observed Integral
a	20	42
b	4	7
c	-	2
d	12	28
e	18	44
f	-	1
g	4	4
h	-	3

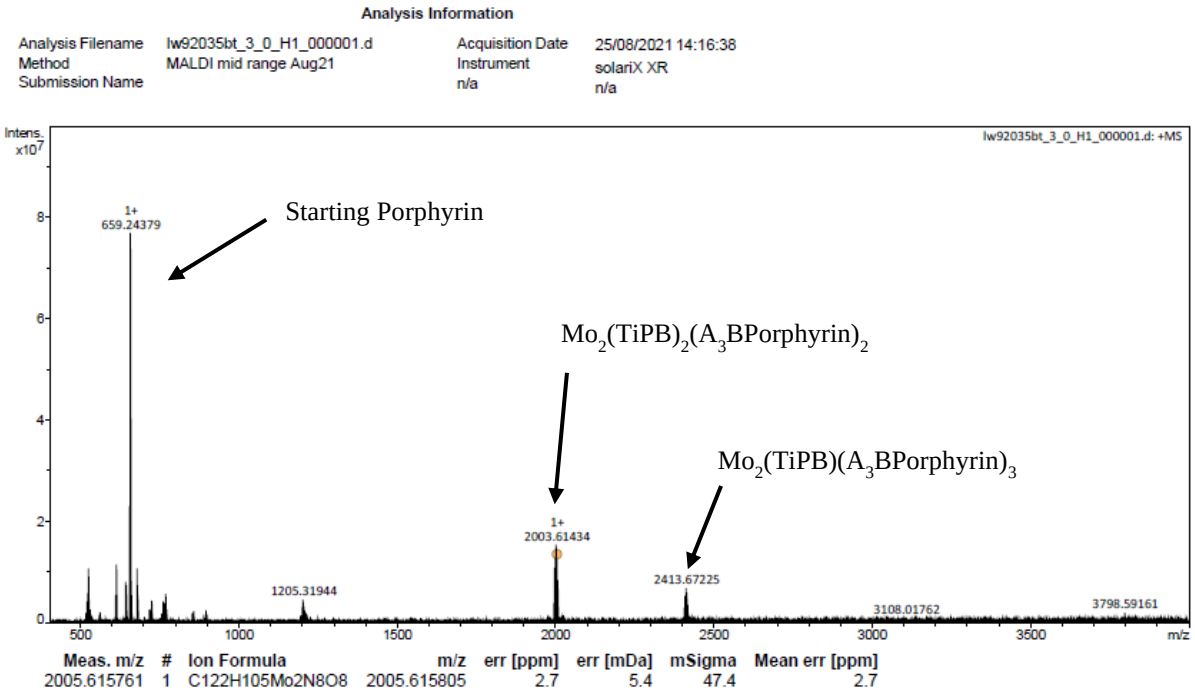

Figure 38: MALDI TOF-MS spectrum of the product from Reaction **C** (dithranol matrix, THF solution)

Table 3: MALDI-TOF-MS signals of the product from Reaction **C** (dithranol matrix, THF solution)

MS peak (m/z)	Assignment
659.24	Free Base Porphyrin
2003.61	$Mo_2(TiPB)_2(A_3BPorphyrin)_2$
2413.67	$Mo_2(TiPB)(A_3BPorphyrin)_3$

Mo_2-based species are observed as a distribution of peaks owing to isotopic distribution of molybdenum (the central, most intense of which is reported in **Table 3**). The obtained spectrum confirmed the presence of $Mo_2(TiPB)_2(A_3BPorphyrin)_2$ (**2**) (2003 m/z). The peak at m/z 659 amu corresponds to the starting free base porphyrin, probably released due to degradation in the spectrometer, as no residual starting porphyrin had been observed in the ^1H NMR spectrum of the same sample. However, the major finding from this spectrum was the presence of the over-substituted species $Mo_2(TiPB)(A_3BPorphryin)_3$ (compound **6)**, an unexpected result given the steric bulk of the porphyrin units. The absence of the mono-substituted conjugate **1** (1594 m/z) was also noteworthy, as *a priori* the under-substituted side product was expected to be the major impurity for this reaction. It is also worth noting that given the different propensity of the species present to ionize and fly in the instrument, the relative sizes of the peaks present cannot be considered a good indicator of purity. However, the mass spectrometry data provided a major shift in the understanding of these systems, showing that the tri-substituted conjugate (**6**) was present alongside the intended product (**2**), rather than **1**.

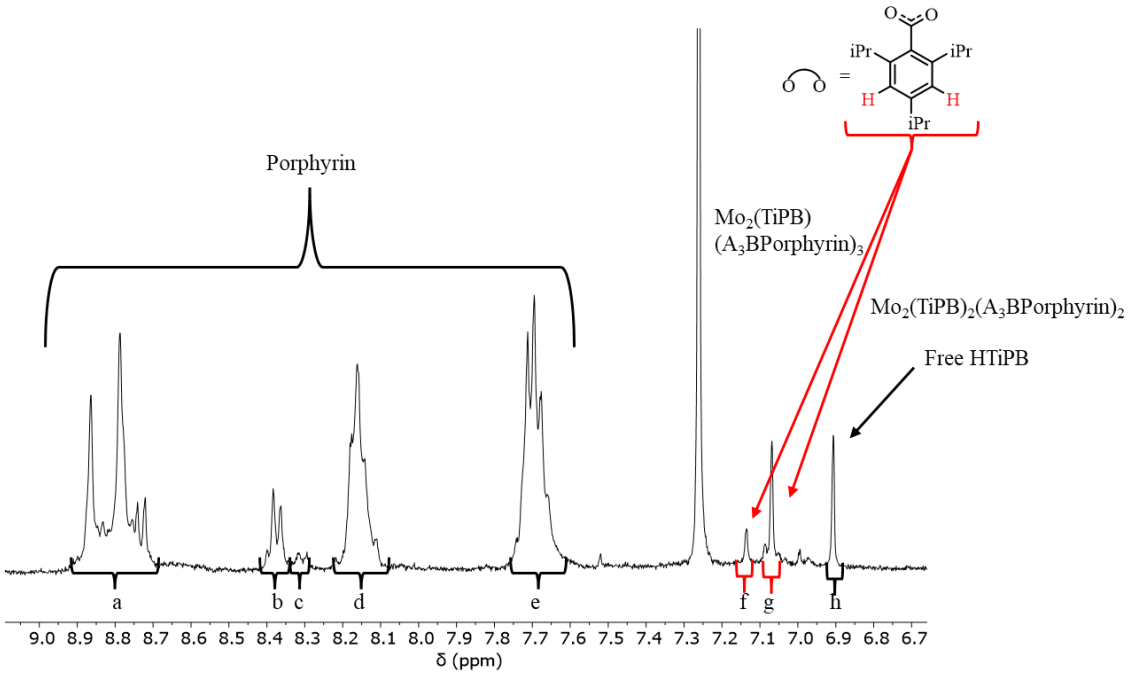

Figure 39: The aromatic region of the ^1H NMR spectrum (chloroform-*d*/THF-H_8) of *trans*-$Mo_2(TiPB)_2(A_3BPorphyrin)_2$ (**2**), reaction **C**

With this information in hand, the ^{1}H NMR spectrum from this reaction was revisited (**Figure 39**). It is now thought that the singlet at 7.07 ppm corresponds to the TiPB phenyl protons on compound **2**, while the singlet at 7.14 ppm corresponds to the equivalent TiPB protons on compound **6**. Most of the porphyrin signals overlap between the two species – which accounts for the large integral values relative to the TiPB signals. Additionally, the smaller doublet at 8.31 ppm comes from the tris-substituted complex **6**, corresponding to the carboxyphenyl aromatic protons on the porphyrin unit *trans*- to the sole TiPB ligand (either the red pair or blue pair in **Figure 40**). The equivalent peaks on the porphyrins *cis*- to the TIPB unit appear at 8.37 ppm, overlapping with the analogous peaks of compound **2**, thereby accounting for the subsidiary peak just to higher ppm of this doublet. Comparison of the integral sizes of the singlets at 7.07 and 7.14 ppm suggested that [**6**]/[**2**] = 0.65 (7.07 ppm corresponds to 4 protons, but 7.14 ppm only 2) and from there it followed that 40% of the total (by moles) was the side product (**6**). A brief exercise was also conducted to demonstrate that the relative sizes of the peaks are roughly what are expected (**Table 4**). The aromatic ^{1}H NMR signals labelled (**a-h)**, and the expected intensity of each calculated based on the size of the phenyl TiPB peaks, which are distinct from one another. The sum of these values was then compared to the measured integral for each peak. In each case, the measured peak was larger than the calculated value (especially for **d** and **a**), but these peaks are roughly the size predicted by the disubstituted/trisubstituted mixture interpretation. The singlet at 6.91 ppm has been assigned to HTiPB impurities, formed either as a product of the reaction or through subsequent decomposition of the molybdenum complexes. Typically, the phenyl HTiPB proton signals usually appear at 7.02 ppm in chloroform-*d*, however through a series of ^{1}H NMR experiments on a sample of Mo_2TiPB_4, it was determined that the peak at 6.91 ppm was indeed the aromatic signal from residual HTiPB (**Figure 41**).

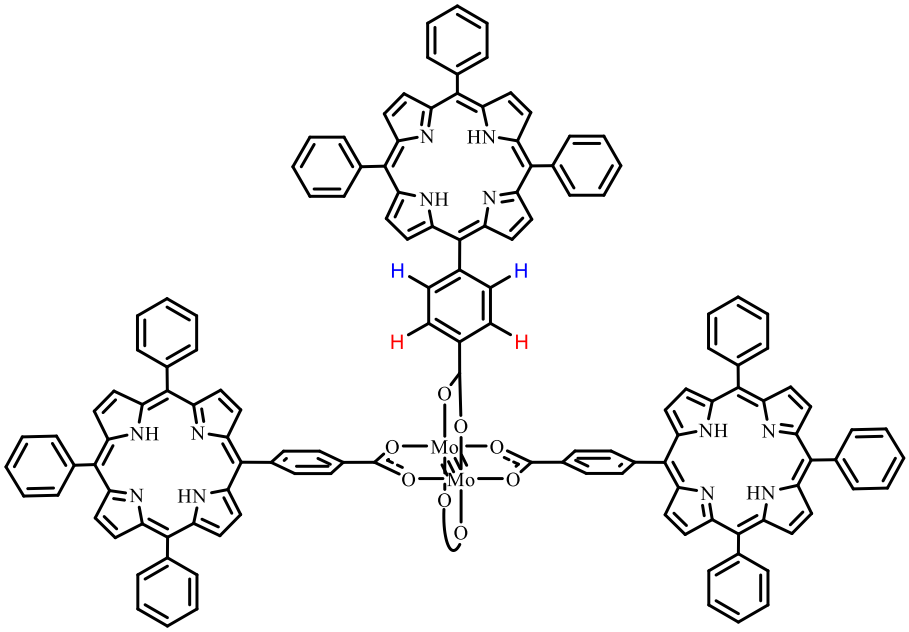

Figure 40: Diagnostic proton environments on the carboxyphenyl protons trans to the TiPB ligand in the tris-porphyrin conjugate (**6**)

Table 4: Contribution of different Mo_2-porphyrin conjugates to the observed integrals in the ^1H NMR spectrum

Cumulative Peak	Contribution to integral from 2	Contribution to integral from 2 (scaled down by 0.65)	Calculated Total	Observed Total
a	20	19.5	39.5	41.9
b	4	2.6	6.6	6.9
c	-	1.3	1.3	1.8
d	12	11.7	23.7	27.6
e	18	17.5	35.5	43.8
f	-	1.3	1.3	1.3
g	4.0	4.0		4.0
h	-	-	-	4.3

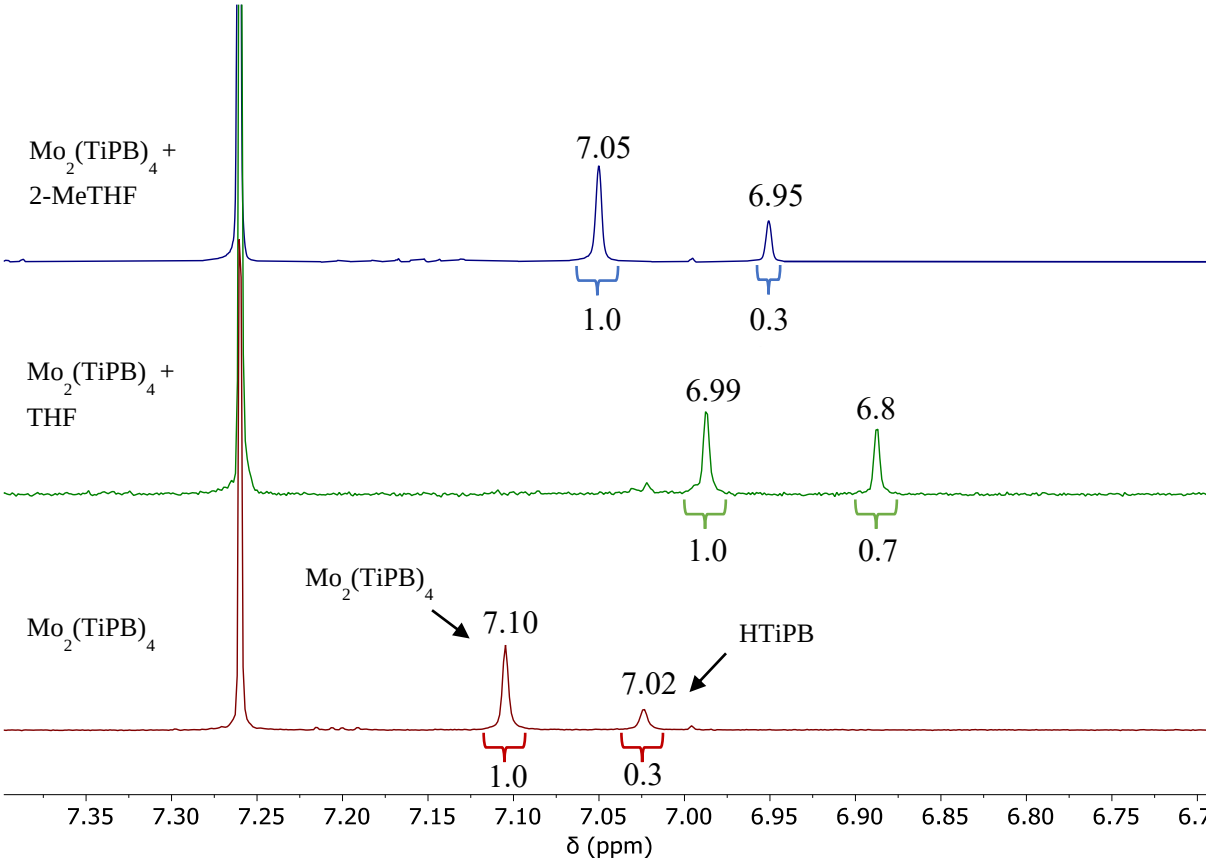

Figure 41: Selected peaks from the ^1H NMR spectrum (chloroform-*d*) of $Mo_2(TiPB)_4$: HTiPB (1:0.3) with added solvent dopants

Upon addition of THF, the $Mo_2(TiPB)_4$ and HTiPB ^1H NMR signals were shifted upfield by around 0.1 ppm. The peak at 6.89 ppm is close to that seen in the spectrum of reaction **C** and supports the conclusion that this does belong to free HTiPB. The shift (ppm) between the two peaks remains the same. It is also worth noting that the integral of the HTiPB signal increases relative to $Mo_2(TiPB)_4$ in the THF sample, and this suggests that THF may encourage/catalyse dissociation of labile ligands, forming (in this case) additional free HTiPB. A 2Me-THF sample

was also investigated as a less coordinating alternative to THF. In this instance, both peaks were shifted upfield, but the relative sizes remained the same, indicating 2Me-THF probably does not catalyse complex breakdown.

Following the revelation that over-substitution, rather than under-substitution was limiting product purity, the reaction was repeated in toluene (reaction **D).** Compound **2** is insoluble in toluene, so the rationale was to precipitate **2** out of solution upon formation, precluding further substitution and biasing the equilibrium towards the intended product. The resultant product was characterised by MALDI-TOF-MS (**Table 5**) and ^{1}H NMR spectroscopy (chloroform-*d*) (**Figure 42**). MALDI-TOF-MS analysis confirmed the presence of both $Mo_2(TiPB)_2(A_3BPorphyrin)_2$ (2002 m/z) and $Mo_2(TiPB)(A_3BPorphyrin)_3$ (2412 m/z), but as a technique is unable to accurately determine the relative concentrations of each.

Table 5: MALDI-TOF-MS signals for the product from reaction **D** with toluene as the reaction medium (dithranol matrix, THF solution)

MS peak (m/z)	Assignment
2003.62	*trans*-$Mo_2(TiPB)_2(A_3BPorphyrin)_2$
2414.67	$Mo_2(TiPB)(A_3BPorphyrin)_3$

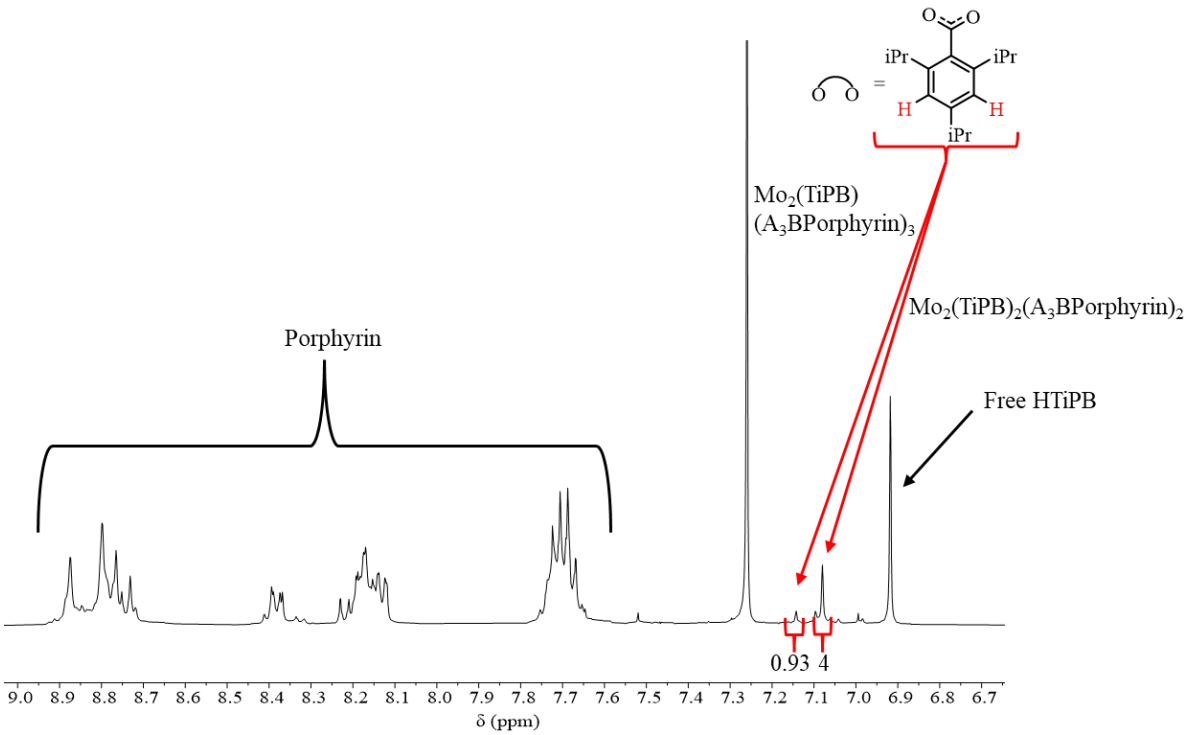

Figure 42: The aromatic region of the ^{1}H NMR spectrum (chloroform-*d*) of *trans*-$Mo_2(TiPB)_2(A_3BPorphyrin)_2$ (**2**), reaction **D**

The ratio of products was assessed by comparing the integrals of the phenyl TiPB proton signals for **2** (7.08 ppm), and **6** (7.14 ppm) (labelled in **Figure 42**). In this instance [**6**]/[**2**] = 0.47, and it followed that 32% of the total (by moles) was the over-substituted product **6**. This constituted a slight improvement over the previous example (reaction **C** which showed 40% over-substitution) where the reaction was conducted in THF but had not changed the overall picture greatly. Furthermore, an increased proportion of HTiPB (6.92 ppm) was seen here, along with a significant quantity of the starting free base porphyrin which explained why the porphyrin peaks appeared much larger than predicted by the integrals of the phenyl TiPB protons. The position of the carboxyphenyl free base porphyrin doublet (labelled blue in **Figure 43**) was itself a curiosity, as the 2 doublets generally appear at 8.53 and 8.36 ppm respectively. A ^{1}H NMR spectrum (chloroform-*d*) of the starting free base porphyrin doped with THF was taken to investigate whether the chemical shift values are changed by the addition of THF to the sample. All the porphyrin signals were shifted upfield, for instance the two sets of carboxylphenyl doublets are shifted to 8.41 and 8.25 ppm respectively. The THF doped starting porphyrin is overlayed against the reaction product in **Figure 43** to demonstrate that the large integral sizes in the original spectrum may be accounted for by the presence of the starting free base porphyrin.

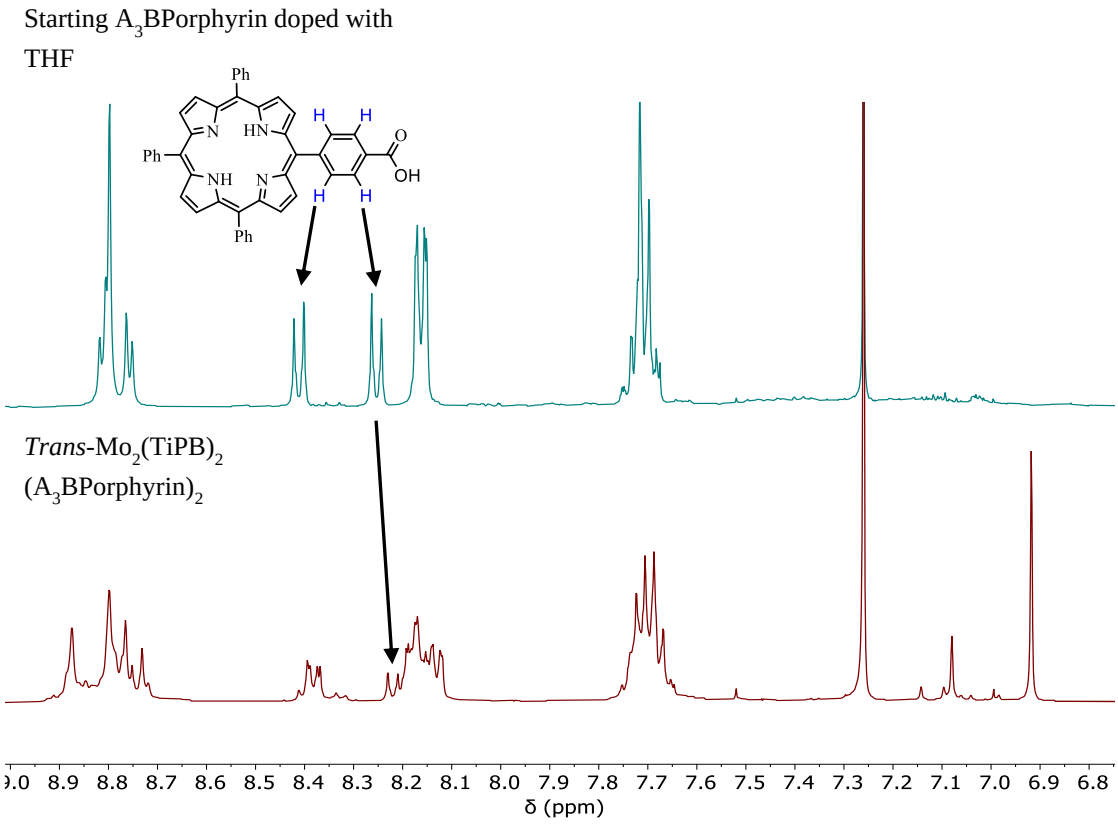

Figure 43: The aromatic region of the ^{1}H NMR spectrum (chloroform-*d*) of the starting A_3B Porphyrin doped with THF (top) overlayed with *trans*-$Mo_2(TiPB)_2(A_3BPorphyrin)_2$ (**2**), reaction **D** (bottom)

Knowing that the reaction for *trans*-$Mo_2(TiPB)_2(A_3BPorphyrin)_2$ (**2)** consistently yields a mixture of products, the reaction stoichiometry was altered to deliberately prepare the trisubstituted complex $Mo_2(TiPB)(A_3BPorphyrin)_3$ (**6**) (**Figure 44**).

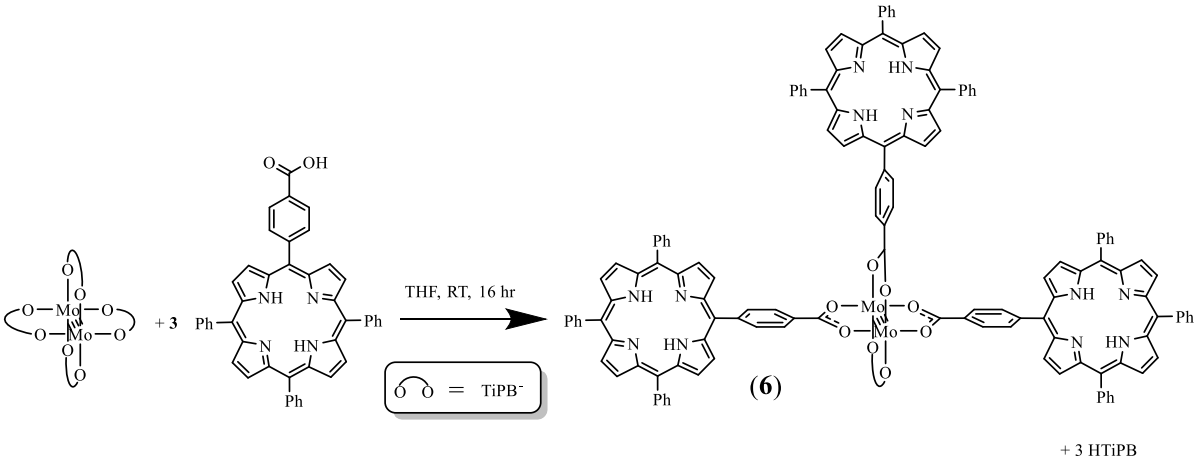

Figure 44: Reaction Scheme for $Mo_2(TiPB)(A_3BPorphyrin)_3$ (**6**), reaction **G**

MALDI-TOF-MS analysis (**Table 6**) confirmed the presence of both **2** and **6**, and that increasing the stoichiometry of porphyrin starting material does not greatly bias the outcome towards a single pure complex. ^1H NMR spectroscopy data were not obtained due to product decomposition. Furthermore, retrospective MALDI-TOF-MS analysis of the reaction to form the mono-substituted conjugate **1** (reaction **A**) found that even when the Mo_2: Porphyrin stoichiometry is held at 1:1, the result is still a mixture of **2** and **6**. The mass spectrometry data are summarized in **Table 7**, but the overall conclusion was that biasing the stoichiometry of the starting materials does not affect product formation and that a mixture of the di-substituted and tri-substituted analogues is formed each time.

Table 6: MALDI-TOF-MS signals for the product from reaction **G** (dithranol matrix, THF solution)

MS peak (m/z)	Assignment
2004.61	$Mo_2(TiPB)_2(A_3BPorphyrin)_2$
2414.67	$Mo_2(TiPB)(A_3BPorphyrin)_3$

Table 7: Summarized MALDI-TOF-MS data upon variation of Mo_2: Porphyrin stoichiometry (dithranol matrix, THF solution)

Sample	Mo_2: Porphyrin Stoichiometry	MS Peak (m/z)	Assignment
$Mo_2(TiPB)_3(A_3BPorphyrin)$ (**1**) (reaction **A**)	1:1	659.24	Free Base $A_3BPorphyrin$
		2003.62	$Mo_2(TiPB)_2(A_3BPorphyrin)_2$
		2413.68	$Mo_2(TiPB)(A_3BPorphyrin)_3$
Trans-$Mo_2(TiPB)_2(A_3BPorphyrin)_2$ (**2**) (reaction **B**)	1:2	659.24	Free Base $A_3BPorphyrin$
		2003.62	$Mo_2(TiPB)_2(A_3BPorphyrin)_2$
		2412.67	$Mo_2(TiPB)(A_3BPorphyrin)_3$
$Mo_2(TiPB)(A_3BPorphyrin)_3$ (**6**) (Reaction **G**)	1:3	2004.61	$Mo_2(TiPB)_2(A_3BPorphyrin)_2$
		2414.67	$Mo_2(TiPB)(A_3BPorphyrin)_3$

Analysis of the product from reaction **F**, **5** $[Mo_2(TiPB)_3]_2$(μ-*trans*-A_2B_2Porphyrin), by ^{1}H NMR spectroscopy (chloroform-*d*/THF-H_8) showed a subtly different situation to the paddlewheel-bridged complexes (**Figure 45**). In this case, the reaction had not gone to completion, indicated by the presence of $Mo_2(TiPB)_4$ at 7.11 ppm. The porphyrin peaks were shifted from the starting material and appeared in roughly the correct proportions. HTiPB (7.03 ppm), was also present, liberated either through the ligand substitution process or through paddlewheel decomposition. The product decomposed before a reliable MALDI-TOF-MS spectrum could be taken, and so plans were made to repeat the reaction with a longer reaction time or increased temperature to help improve starting material consumption. However, due to time constraints in the laboratory this experiment was not undertaken.

In the synthesis of **2** and **6**, alterations to the stoichiometry, reaction length, and the reaction medium did not make significant changes to the product distribution. Dimolybdenum paddlewheel complexes typically react with silica and alumina, so column chromatography was unfeasible and attempts to purify via recrystallisation still led to a mixture of products. Consequently, there was no known way to separate out the mixture of products once formed. A recent idea is to employ size-exclusion chromatography to separate **2** and **6** but due to time constraints, this was not attempted.

While the lability of the TiPB ligand was seen as favourable in initial studies, the results suggest that this lability allows an equilibrium to occur which favours multiple substitution products which are difficult to separate. Therefore, changes were made to the system to encourage formation of a single product, and the labile TiPB ancillary ligands were replaced with non-labile formamidinates.

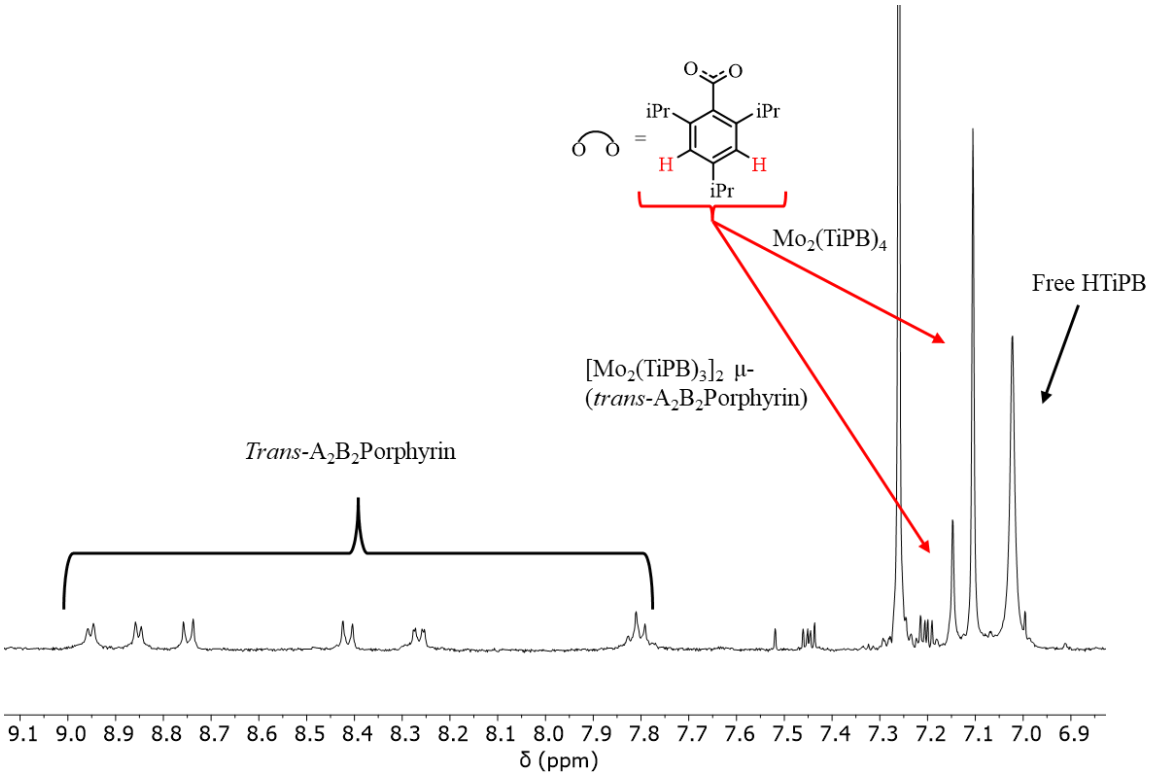

Figure 45: The aromatic region of the ^{1}H NMR spectrum (chloroform-*d*) of $[Mo_2(TiPB)_3]_2$ (μ-*trans*-A_2B_2Porphyrin) (**5**), reaction **F**

DAniF Systems

Following the foray into carboxylate based ancillary ligands with TiPB, the di-anisyl substituted formamidinate DAniF (**Figure 29**, **ii**) was chosen as an alternative paradigm to TiPB based paddlewheels for investigation.

Formamidinate ligands are well known within the context of paddlewheel chemistry as stable, tuneable, and non-labile N-donor ligands.[31,73] In particular, the non-lability was seen as desirable from the perspective of avoiding over-substitution, but also raised some synthetic challenges as paddlewheel-porphyrin conjugates could no longer be prepared directly from the homoleptic starting paddlewheel (as with $Mo_2(TiPB)_4$). Initially the homoleptic paddlewheel complex $Mo_2(OAc)_4$ was prepared from $Mo(CO)_6$ (**Figure 46**). Then, an extra synthetic step was required to prepare $Mo_2(DAniF)_3(OAc)$ (**Figure 47**), from $Mo_2(OAc)_4$. From there, the sole acetate ligand could be replaced by a variety of carboxyphenyl porphyrins to form the corresponding conjugate (**Figure 48**).

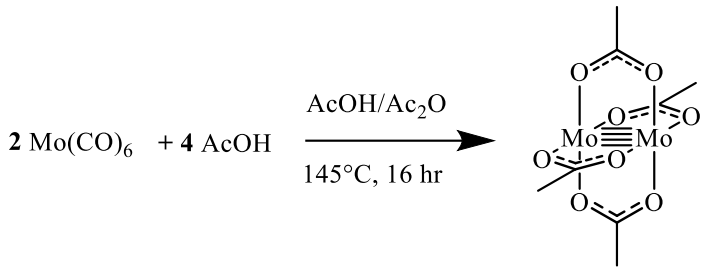

Figure 46: Reaction scheme for $Mo_2(OAc)_4$

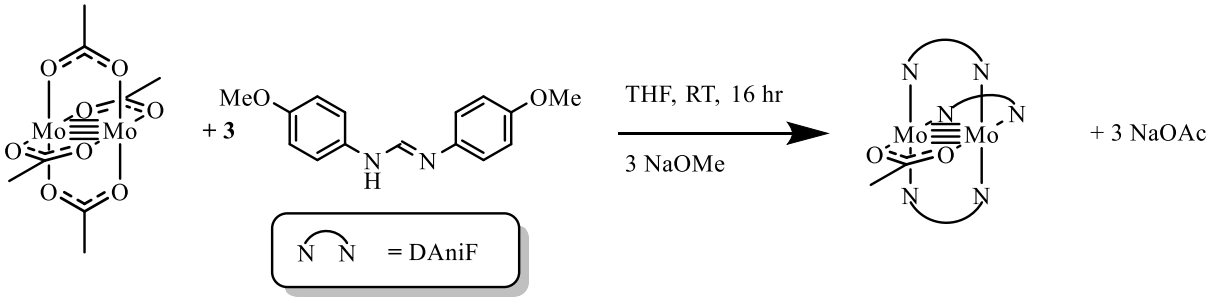

Figure 47: Reaction Scheme for $Mo_2(DAniF)_3(OAc)$

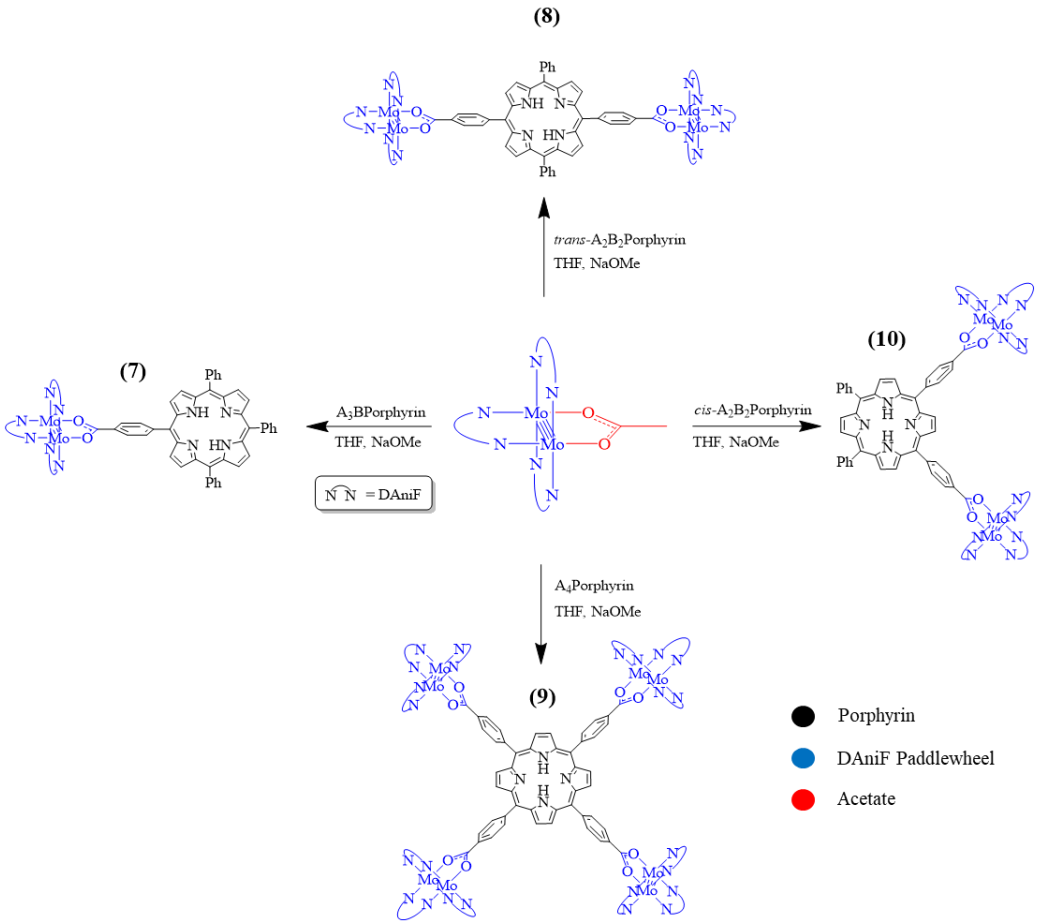

Figure 48: Paddlewheel-porphyrin conjugates synthetically accessible from $Mo_2(DAniF)_3(OAc)$

Investigative Synthesis

The first complex to be prepared from this family was the monosubstituted, DAniF-based paddlewheel/porphyrin conjugate $Mo_2(DAniF)_3(A_3Bporphyrin)$ (**7**), shown in **Figure 49**. The solvent was removed, and the crude product was washed with ethanol and filtered through celite to remove impurities. A sticky black solid was obtained (44% yield). Characterisation took place by MALDI-TOF-MS and ^{1}H, ^{13}C, ^{1}H-^{13}C HSQC, and ^{1}H-^{13}C HMBC NMR spectroscopy (chloroform-*d*).

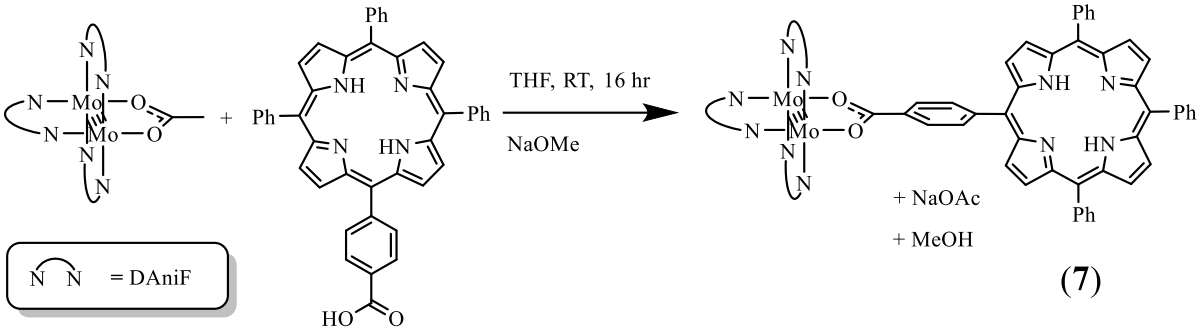

Figure 49: Reaction scheme for $Mo_2(DAniF)_3(A_3BPorphyrin)$ (**7**) reaction **H**

Several variations on this protocol were carried out to assess the effect of time, starting material stoichiometry, washing solvent and porphyrin zincation on the reaction. Furthermore, several variations were carried out with porphyrins carrying multiple pendent carboxyphenyl units to build up complexes with bridging porphyrin units (**8** and **9** in **Figure 48**). The key results are summarized in **Table 8**.

Table 8: Summary of reaction optimization for the synthesis of conjugates from $Mo_2(DAniF)_3(OAc)$

Reaction	Starting Porphyrin	Mo_2: Porphyrin stoichiometry	Reaction Time (hr)	Washing Solvent	Yield (%)	Appearance
H	A_3B Porphyrin	1:1	16	Ethanol	44	Sticky black solid
I	A_3B Porphyrin	1:1	5	Ethanol	16	Fine dark brown powder
J	A_3B Porphyrin	1:1.5	16	Ethanol, diethyl ether	39	Fine brown powder
K	Zn-A_3B Porphyrin	1:1	5	Ethanol	19	Sticky black solid
L	*Trans*-A_2B_2Porphyrin	2:1	3	Ethanol, diethyl ether	46	Fine brown powder
M	B_4Porphyrin	4:1	3	Ethanol	10	Sticky black solid

Washing with diethyl ether in addition to ethanol proved effective at reducing the sticky, tar-like quality of the products formed, to produce fine brown powders that were cleaner and easier to work with although very staticky. In general, longer reaction times led to higher yields, although in some cases this also led to the formation of more unwanted side-products (*vide infra*).

The isolated products from reactions **H** and **K (Table 8)** were characterised by ^{1}H NMR spectroscopy (chloroform-*d*) and MALDI-TOF-MS. The only major difference between the ^{1}H NMR spectra (chloroform-*d*) for the zincated and non-zincated analogues was the absence of the inner ring protons at -2.74 ppm for metalated variant. Consequentially, only the non-zincated ^{1}H NMR spectrum (**Figure 50**) is discussed here, and it was noted that the reaction procedure was insensitive to the presence of zinc in the central porphyrin cavity.

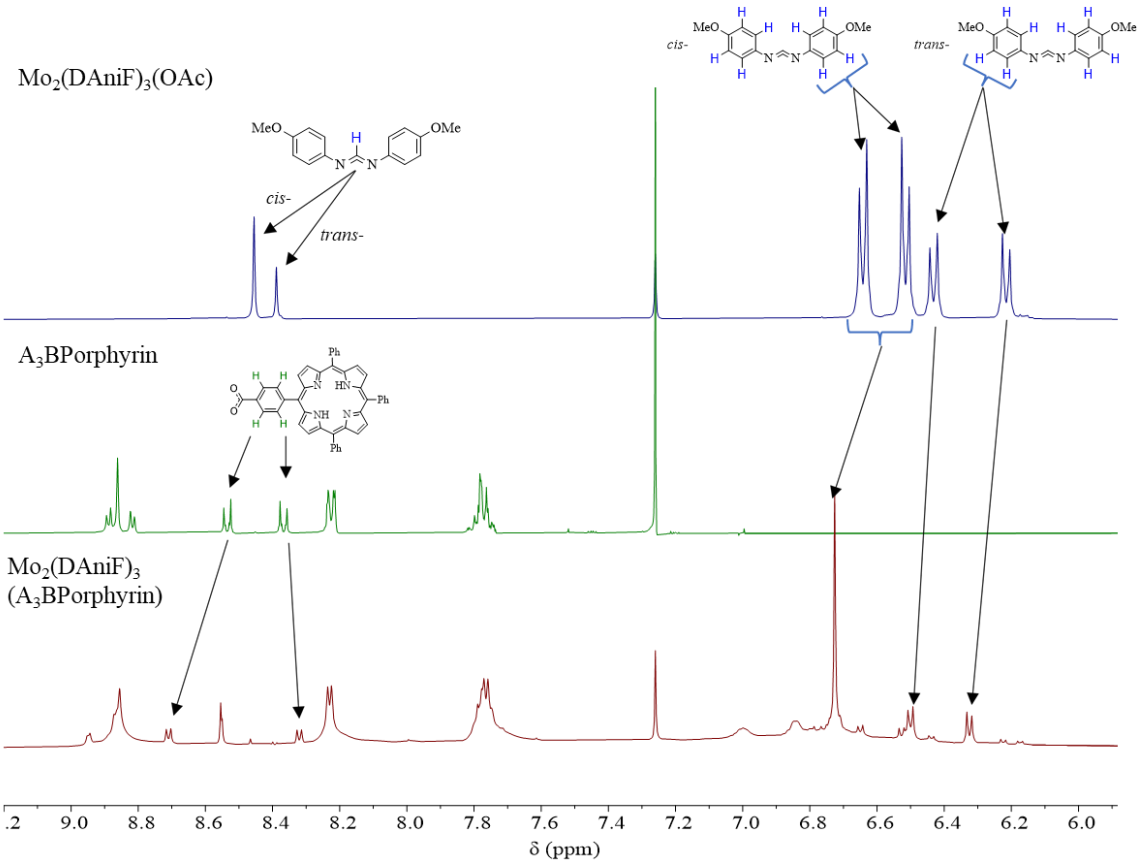

Figure 50: The aromatic region of the ^{1}H NMR spectrum (chloroform-*d*) of $Mo_2(DAniF)_3(A_3BPorphyrin)$ (**7**), reaction **H Table 8**

The phenyl protons on the ancillary DAniF ligands are key diagnostic peaks in this system and appear shifted from both the starting material and the free ligand. The integrals were largely consistent with formation of **7**. However, several side products were also present in the spectrum. Small doublets in the region 6.6-6.2 ppm correspond to the phenyl DAniF protons in the starting material, $Mo_2(DAniF)_3(OAc)$. The broader peaks in the range 6.8-7 ppm correspond to free HDAniF, formed from degradation of the paddlewheel. The porphyrin-based peaks at 8.86, 8.24, and 7.78 ppm were also too large compared to the rest of the porphyrin signals, possibly due to tetraphenylporphyrin impurities in the sample. One curiosity in the

spectrum is the singlet at 6.73 ppm, which corresponds to the phenyl protons on the two DAniF ligands *cis*- to the carboxyphenyl porphyrin. In $Mo_2(DAniF)_3(OAc)$, these two protons are distinct chemical environments, and appear as two separate doublets. However, upon replacement of the acetate ligand for the carboxyphenyl porphyrin, the chemical shifts become almost identical and the two peaks merge into one singlet. This was confirmed by the ^{1}H-^{13}C HSQC spectrum (**Figure 51**), which clearly showed two independent carbons coupling to a proton signal at 6.73 ppm. Overall, this was an improvement over the TiPB based systems because i) the compound was more soluble, which made characterisation more straightforward and ii) the non-labile DAniF ligands prevented over-substitution. Although both unreacted starting material and decomposition products were present in the spectra, this encouraging proof-of-concept reaction indicated the potential for further optimisation.

The ^{1}H NMR spectroscopy data were largely corroborated by MALDI-TOF-MS (**Table 9**), which confirmed the presence of the intended product in both cases, but also served as a reminder that neither sample was entirely pure, and that further reaction optimization was required.

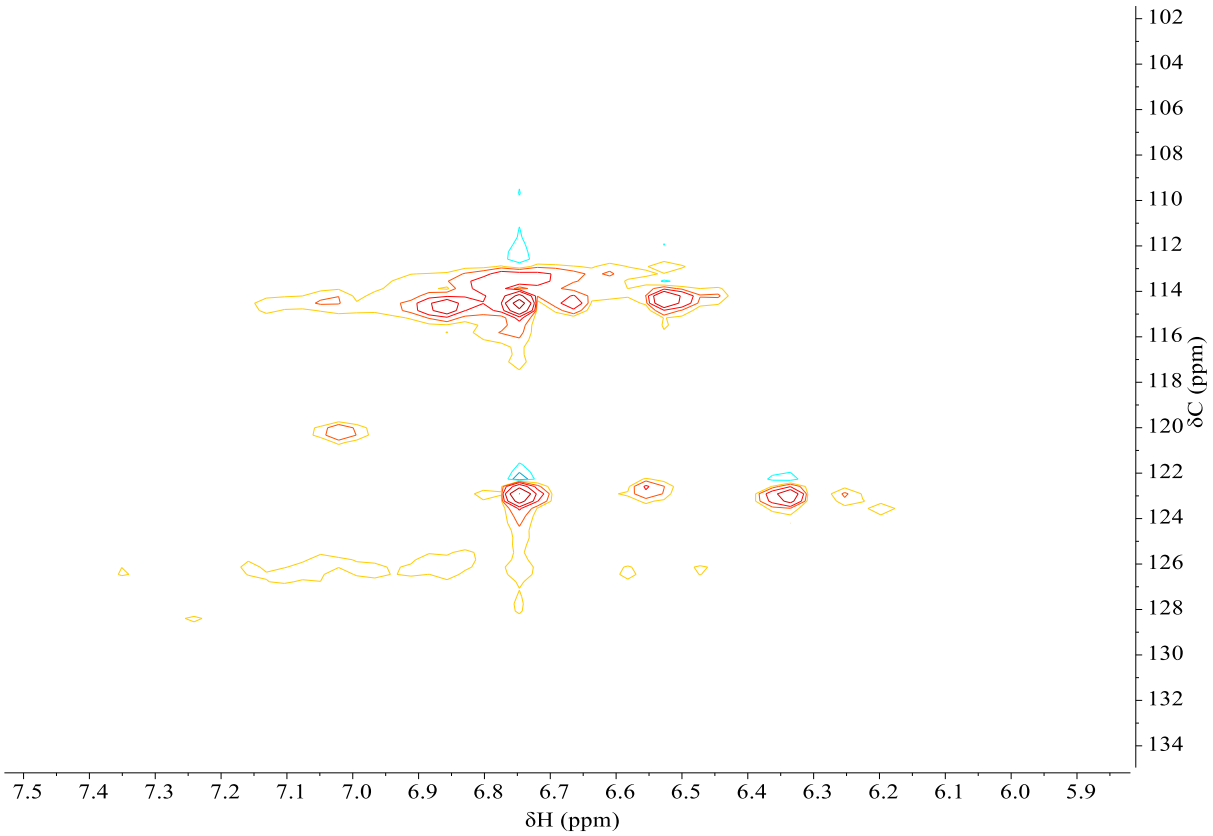

Figure 51: Selected signals from the ^{1}H-^{13}C HSQC spectrum (chloroform-*d*) of $Mo_2(DAniF)_3(A_3BPorphyrin)$ (**7**), reaction **H**

Table 9: MALDI-TOF-MS data for monosubstituted DAniF conjugates (dithranol matrix, THF solution)

Reaction	MS Peak (m/z)	Assignment
H, $Mo_2(DAniF)_3(A_3BPorphyrin)$ (**7**)	1617.38	$Mo_2(DAniF)_3(A_3BPorphyrin)$
K, $Mo_2(DAniF)_3$(Zn-A_3BPorphyrin) (**7a**)	720.15	Free base Zn-A_3BPorphyrin
	1677.29	$Mo_2(DAniF)_3$(Zn-A_3BPorphyrin)

When the reaction was repeated with a shorter (5 hr) reaction time (reaction **I**), neither the broad peaks around 6.8-7 ppm, nor the porphyrin impurities were present in the ^{1}H NMR spectrum (**Figure 52**). However, the doublets at 6.42 and 6.21 ppm were indicative of residual starting material.

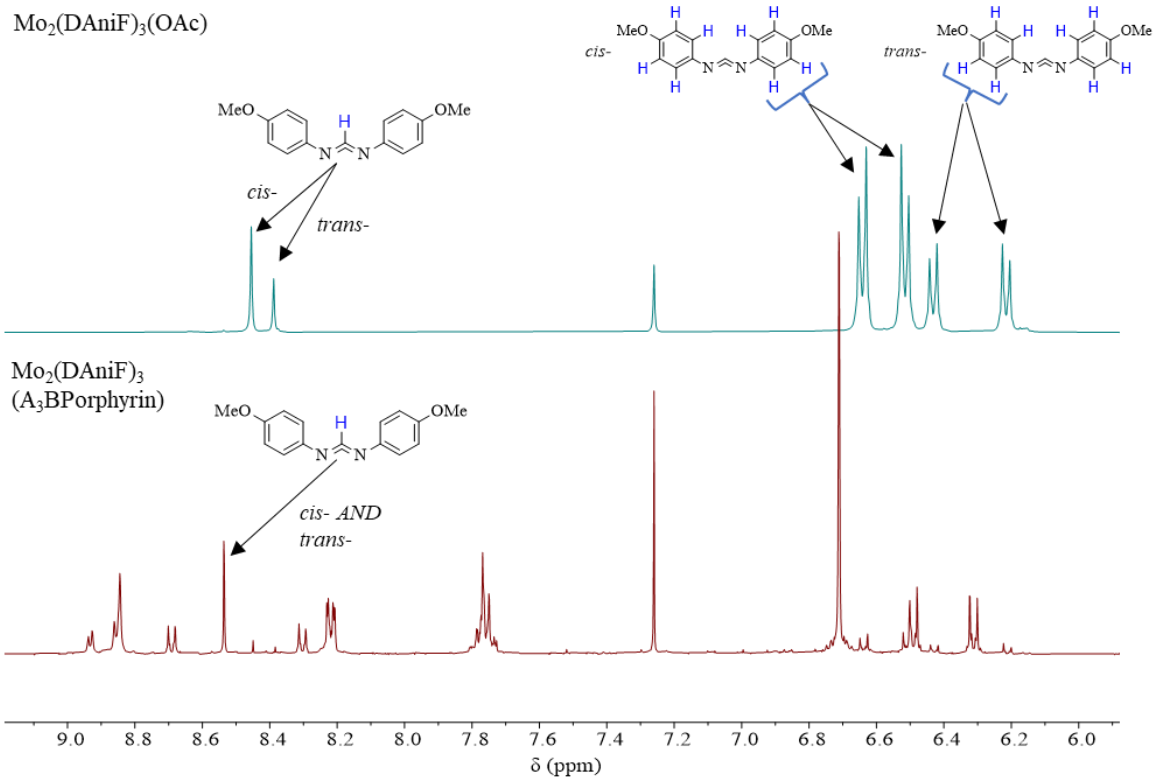

Figure 52: The aromatic region of the ^{1}H NMR spectrum (chloroform-*d*) of $Mo_2(DAniF)_3(A_3BPorphyrin)$ (**7**), reaction **I** (reduced reaction time)

The next issue to be addressed was therefore starting material consumption. Parallel research in the Wilkinson Group had determined that addition of 1.5 equivalents of ligand and overnight reaction times could be an effective approach to drive Mo_2 starting material consumption. Excess porphyrin at the end of the reaction was not seen to be an issue as its relative solubility in diethyl ether allowed for removal during the work-up. The isolated product from reaction **J**, where a 1.5 excess of A_3BPorphyrin had been incorporated was analysed by MALDI-TOF-MS (**Table 10**) and ^{1}H NMR spectroscopy (chloroform-*d*) (**Figure 53**).

Table 10: MALDI-TOF-MS signals for $Mo_2(DAniF)_3(A_3BPorphyrin)$ (**7**), reaction **J** (dithranol matrix, THF solution)

MS peak (m/z)	Assignment
1618.37	$Mo_2(DAniF)_3(A_3BPorphyrin)$

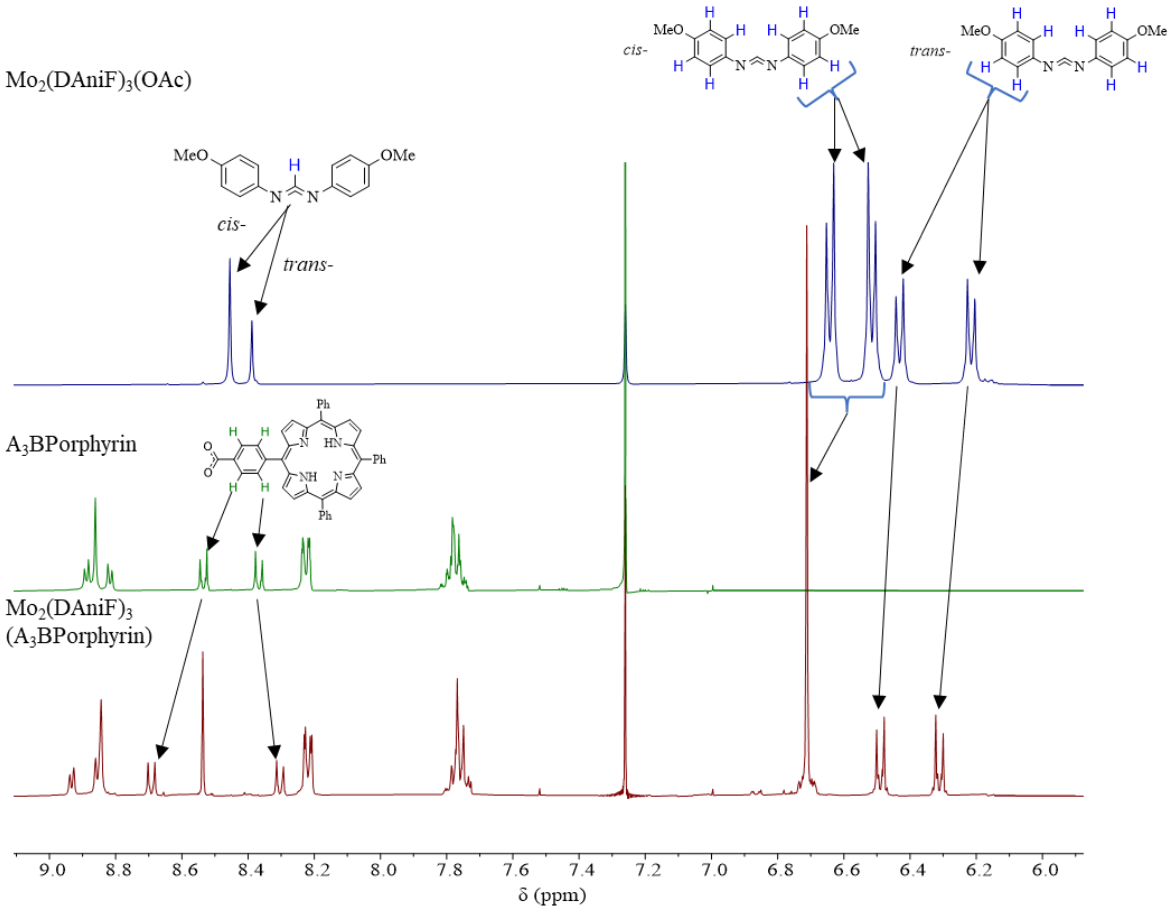

Figure 53: The aromatic region of the ^{1}H NMR spectrum (chloroform-*d*) of $Mo_2(DAniF)_3(A_3BPorphyrin)$ (**7**), reaction **J**

Both the mass spectrum and the ^{1}H NMR spectrum showed a marked improvement in starting material consumption, which can be seen in the ^{1}H NMR spectrum as the absence of the small $Mo_2(DAniF)_3$ doublets in the region 6.2-6.45. This sample was therefore retained for cyclic voltammetry and UV/Vis measurements (*vide infra*).

The reaction to produce the porphyrin bridged system $[Mo_2(DAniF)_3]_2$(μ-*trans*-A_2B_2Porphyrin) (compound **8**, reaction **L**), resulted once again in a mixture of the intended product alongside residual starting material and some DAniF based decomposition products. The ^{1}H NMR spectrum for this reaction is shown in **Figure 54**. As in the previous examples there was free HDAniF (best seen in signals at 7.01 and 6.88 ppm) and residual starting material

$Mo_2(DAniF)_3(OAc)$. The doublets at 6.62, 6.48, 6.42 and 6.20 correspond to the phenyl protons on $Mo_2(DAniF)_3(OAc)$. The presence of cross peaks in the COSY spectrum at (6.62,6.48) and (6.42,6.20) confirms these signals are coupled which is consistent with this assessment. The 2:1 singlets at 8.38 and 8.37 likely correspond to the *cis*- and *trans*- DAniF formyl C-H respectively, which is a curiosity as these signals usually appear at 8.47 and 8.40. However, it is known that both the ring currents introduced by the porphyrin and THF impurities in the sample can alter the chemical shift values. These peaks also integrate in the correct ratios with the acetate singlet at 2.60 ppm (1.02: 2.73). Comparison of the integral for the central DAniF proton in the product (8.53 ppm) with the *cis*-central DAniF proton in the starting material (8.45 ppm) (labelled in **Figure 54**) suggested that only 47% (by moles) of the total was the final product and that more than half was unconsumed starting material. In addition to starting material impurities, the MALDI-TOF-MS data (**Table 11**) also suggested the presence of the mono-substituted species $Mo_2(DAniF)_3(HA_2B_2Porphryin)$, where only one of the carboxyphenyl units on the porphyrin has become a point of attachment to a paddlewheel moiety. However, the ^1H NMR evidence for this is unclear. It may be that this species was formed by product decomposition within the MALDI-TOF-MS instrument. Ideally, this reaction would have been repeated with a longer reaction time and with the addition of an excess of porphyrin, as in the case of reaction **J**, but time constraints in the laboratory prevented this.

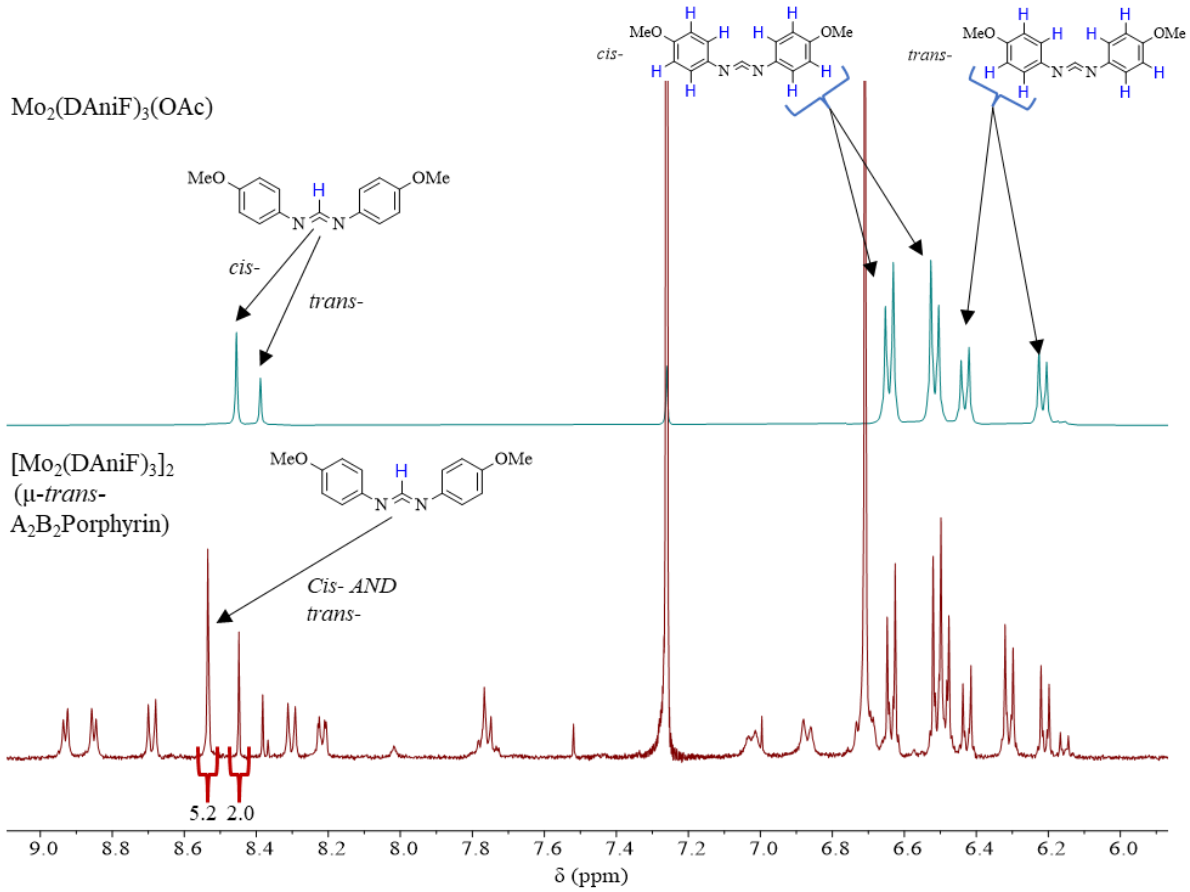

Figure 54: The aromatic region of the ^1H NMR spectrum (chloroform-*d*) of $[Mo_2(DAniF)_3]_2$ (μ-*trans*-A_2B_2Porphyrin) (**8**), reaction **L**

Table 11: MALDI-TOF-MS signals for $[Mo_2(DAniF)_3]_2$ (μ-*trans*-A_2B_2Porphyrin) (**8**), reaction **L** (dithranol matrix, THF solution)

MS peak (m/z)	Assignment
1020.16	$Mo_2(DAniF)_3(OAc)$
1662.37	$Mo_2(DAniF)_3(HA_2B_2Porphryin)$
2612.51	$[Mo_2(DAniF)_3]_2$(μ-*trans*-A_2B_2Porphyrin)

The same issue of starting material consumption carried over to the tetrasubstituted paddlewheel porphyrin, $[Mo_2(DAniF)_3]_4$ (μ-B_4Porphyrin) (compound **9**) (reaction **M, Figure 55**). There were concerns that the solubility may be too poor for the conventional characterisation methods, similar to the more heavily substituted TiPB complexes. However, whilst the solubility of **9** was lower than **8**, characterisation by ^{1}H NMR (chloroform-*d*) was still possible (**Figure 56**). MALDI-TOF-MS analysis was also conducted, but no product was visible, probably because the product did not ionise sufficiently for mass spectrometric analysis.

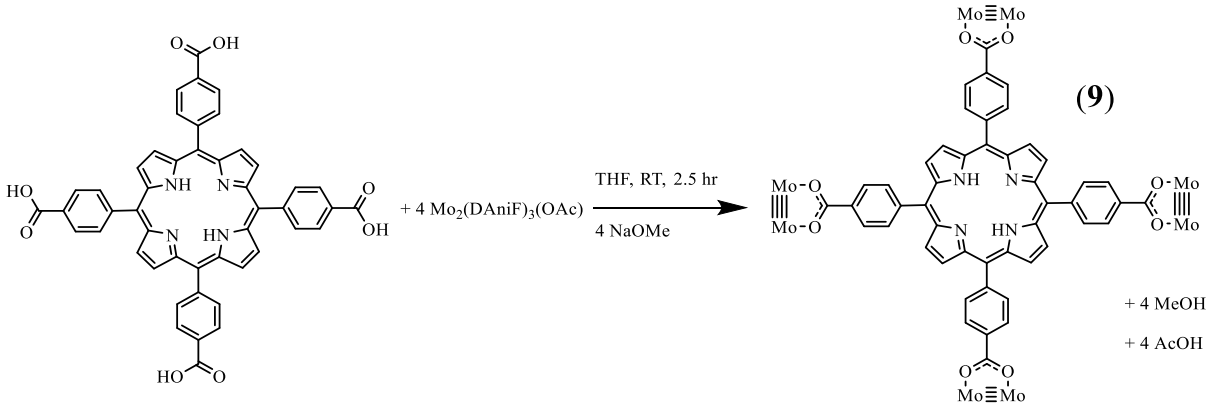

Figure 55: Reaction scheme for $[Mo_2(DAniF)_3]_4$ (μ-B_4Porphyrin) (**9**), reaction **M**. Ancillary ligands on Mo_2 unit are omitted for clarity

In the ^{1}H NMR spectrum (chloroform-*d*) (**Figure 56**), the broad peaks in the range 6.8-7 ppm correspond to HDAniF, and the subsidiary doublets at 6.63, 6.42 and 6.21 ppm correspond to unreacted $Mo_2(DAniF)_3(OAc)$. Integral comparison of the central DAniF proton in the product (8.52 ppm) with the *cis*- central DAniF proton on the starting material (8.44 ppm) (labelled in **Figure 56**) suggested that only 39% of the mixture (by moles) was the final product, and in fact the majority was unreacted starting material. However, it is also worth noting that this calculation is also dependent on the solubility of the species in chloroform-*d* and the relative insolubility of the product may bias this figure in favour of unreacted starting material. In any case, the picture was clear that the product was contaminated with residual $Mo_2(DAniF)_3(OAc)$. An excess of porphyrin alongside a longer reaction time would be

required to push the reaction to completion. As before however, time constraints in the laboratory prevented this experiment taking place.

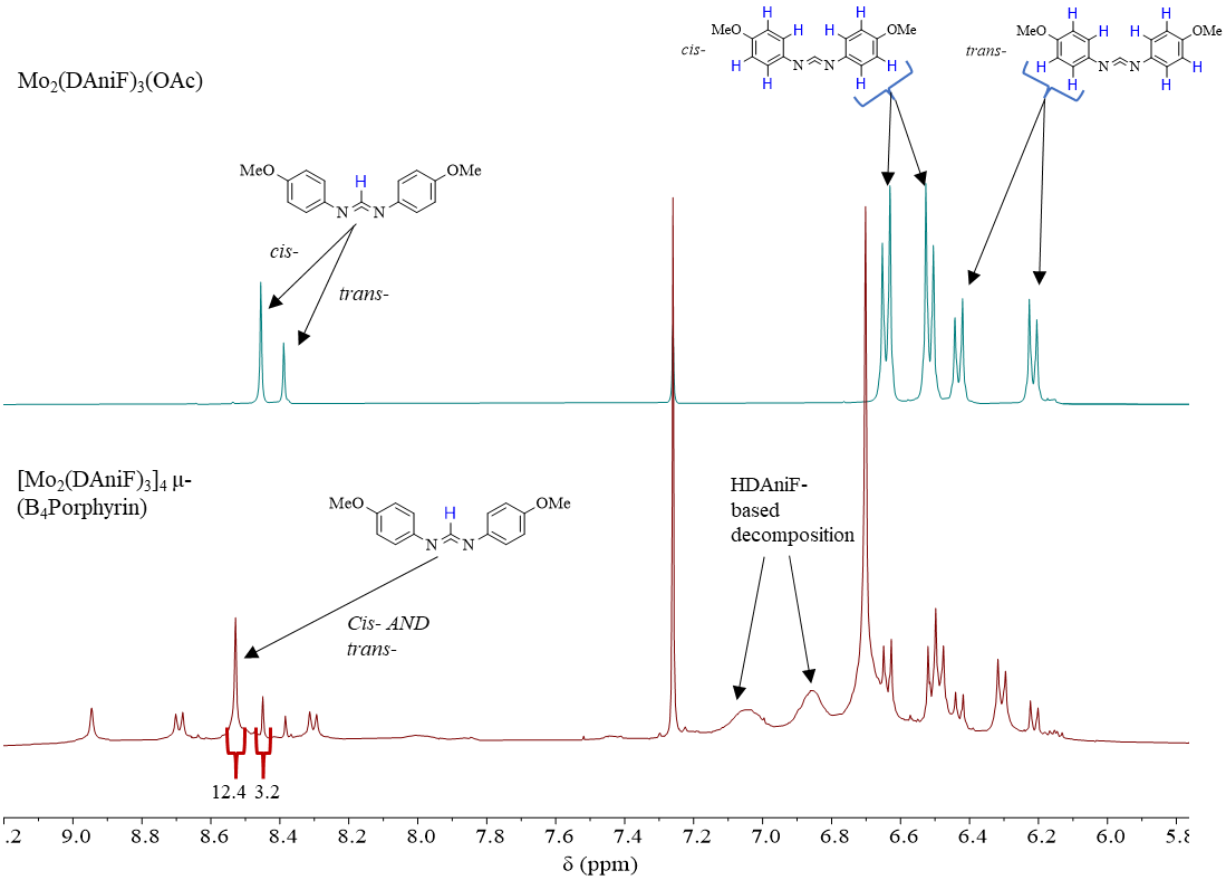

Figure 56: The aromatic region of the ^{1}H NMR spectrum (chloroform-*d*) of $[Mo_2(DAniF)_3]_4$ (μ-B_4Porphyrin) (**9**), reaction **M**

Further Characterisation

Compounds **7** (**Figure 57**) and **8** (**Figure 60**) were analysed by CV (THF solution vs Fc/Fc^+) and UV/Vis spectroscopy (THF solution). Three major peaks were observed in the cyclic voltammogram for $Mo_2(DAniF)_3(A_3BPorphyrin)$ (compound **7**) (**Figure 58**, **Table 12**). The first a 1-electron paddlewheel oxidation at -273 mV, and then as the potential scanned lower, 2 successive 1-electron porphyrin reductions at -1654 and -1976 mV respectively. The irreversible porphyrin reduction peak at around -2200 mV is an electrochemically generated species absent in the first cycle (**Figure 59**, **a**), which grew over the course of the experiment. The best results were obtained upon scanning towards negative potentials first, as scanning oxidatively initially led to irreversibility of the porphyrin reductions and sample decomposition. Porphyrin oxidations are present when scanning to higher potentials but were irreversible and led to permanent decomposition of the compound (and hence loss of CV signals). **Figure 59** (**b-d**) takes a closer look at the fully reversible paddlewheel oxidation at -272 mV. Peak current scaled linearly with √scan rate, confirming electrochemical reversibility, but **Figure 59 b** and **c** show the forward and reverse peaks drifting apart as the scan rate is raised. This is indicative of slightly sluggish electron transfer within the cell, probably a consequence of slow diffusion of the paddlewheel units towards/away from the electrode which is unsurprising given the large size of the conjugate.

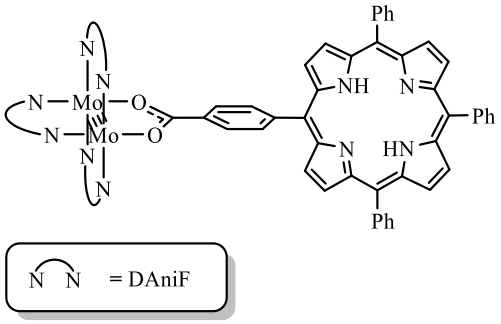

Figure 57: $Mo_2(DAniF)_3(OAc)$ (**7**)

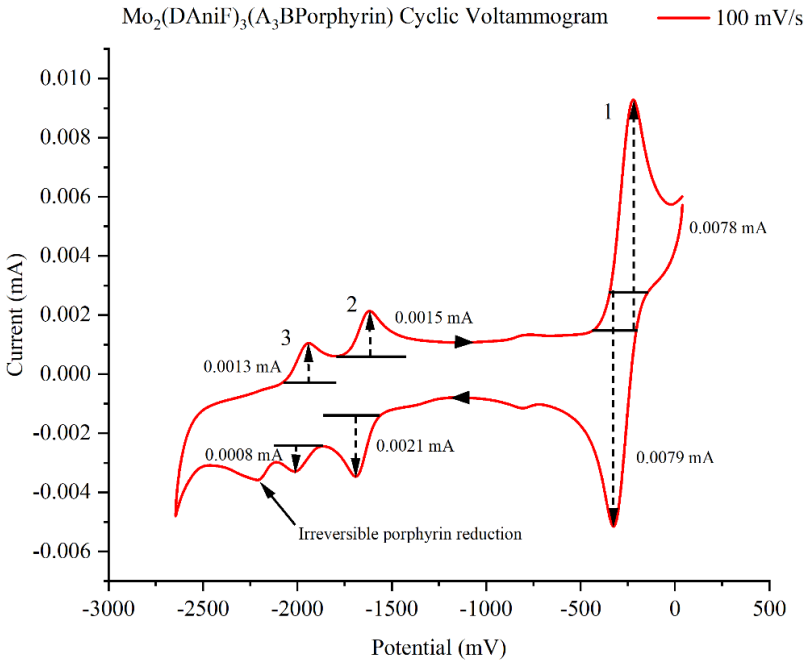

Figure 58: $Mo_2(DAniF)_3(A_3BPorphyrin)$ Cyclic Voltammogram (100 mV/s vs Fc/Fc^+, 0.1 M $[n\text{-}Bu_4][PF_6]$ in THF, 298 K)

Table 12: $Mo_2(DAniF)_3(A_3BPorphyrin)$ (**7**) CV Peaks

CV Peak	Assignment	$\Delta E_{1/2}$ (mV)	i_{pc}/i_{pa}
1	Paddlewheel oxidation	-272	0.99
2	1st Porphyrin reduction	-1654	0.71
3	2nd Porphyrin reduction	-1976	1.6

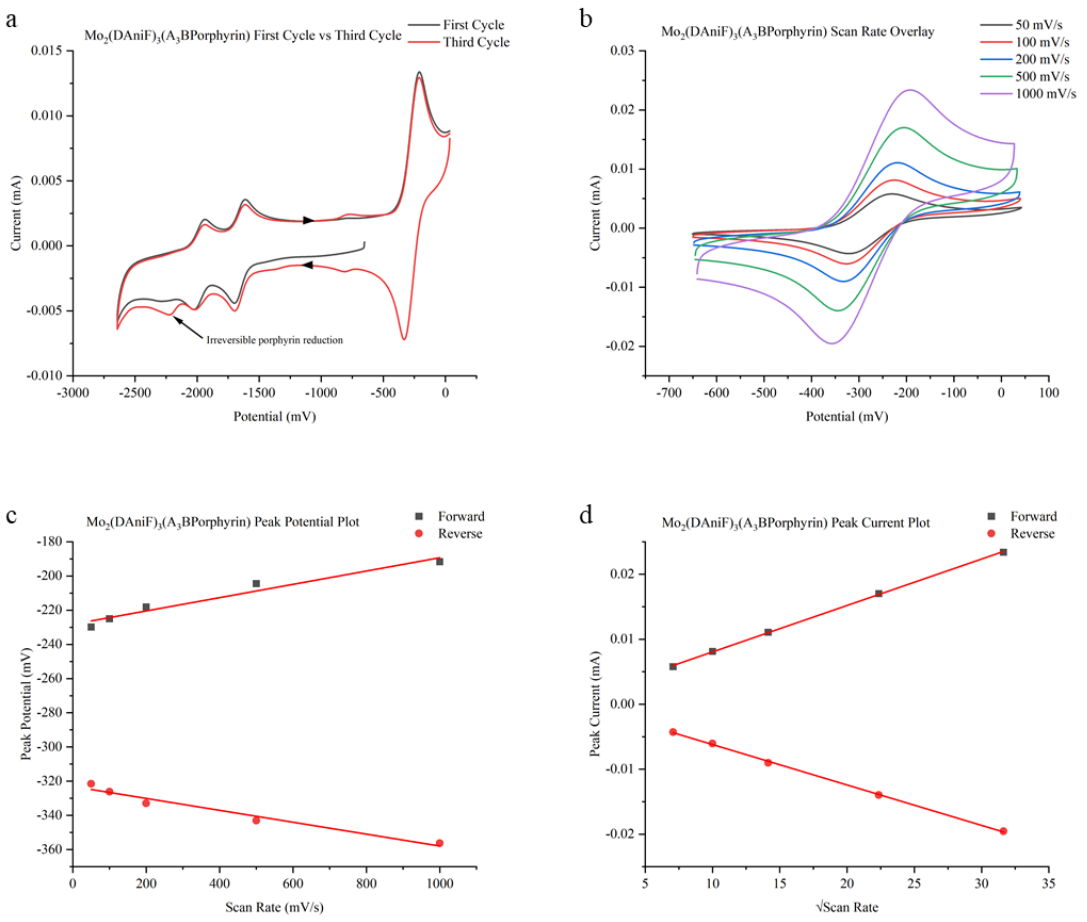

Figure 59: CV Plots (vs Fc/Fc^+, 0.1 M $[n\text{-}Bu_4][PF_6]$ in THF, 298 K) for $Mo_2(DAniF)_3(A_3BPorphyrin)$ (**7**). **a)** First cycle vs third cycle comparison (100 mV/s), **b)** Scan rate overlay for 1st paddlewheel oxidation, **c)** Peak potential vs scan rate for 1st paddlewheel oxidation, **d)** Peak current vs √scan rate for 1st paddlewheel oxidation

The features of the cyclic voltammogram for $[Mo_2(DAniF)_3]_2$(μ-*trans*-A_2B_2Porphyrin) (**8**) were essentially the same as for **7** (**Figure 61**, **Table 13**). It had been hypothesised that the bridging porphyrin unit may facilitate through-bond electronic communication between the two paddlewheel units via overlap between the Mo_2 δ orbitals and the porphyrin π system. This effect could potentially stabilise a mixed valence (singly oxidised) state where the single positive charge is partially delocalised across both Mo_2 units. This would manifest as two separate paddlewheel peaks in the region around -200 mV. However, no evidence of this was found and only 1 (reversible) paddlewheel oxidation signal was observed at -243 mV, and differential pulse voltammetry (DPV) confirmed this peak only comprised of 1 electrochemical event (**Figure 62**). Much like **7**, 2 successive 1-electron porphyrin reductions were observed (although with greater reversibility in this example). The reversible 1-electron paddlewheel oxidation behaved similarly to **7** showing full electrochemical reversibility but slightly sluggish electron transfer kinetics (**Figure 63**, **b-d**). Further oxidations were present at potentials greater than 500 mV. In particular, the signal labelled in **Figure 63**, **a** is thought to originate from DAniF oxidation as the peak is around 3 times the size of the 1st paddlewheel oxidation, but porphyrin

oxidations may also be present in this region. In any case, scanning to potentials greater than 500 mV (vs Fc/Fc^{+}) led to irreversible oxidation which permanently decomposed the sample.

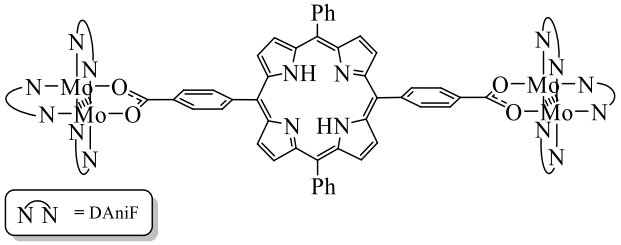

Figure 60: $[Mo_2(DAniF)_3]_2$ (μ-*trans*-A_2B_2Porphyrin) (**8**)

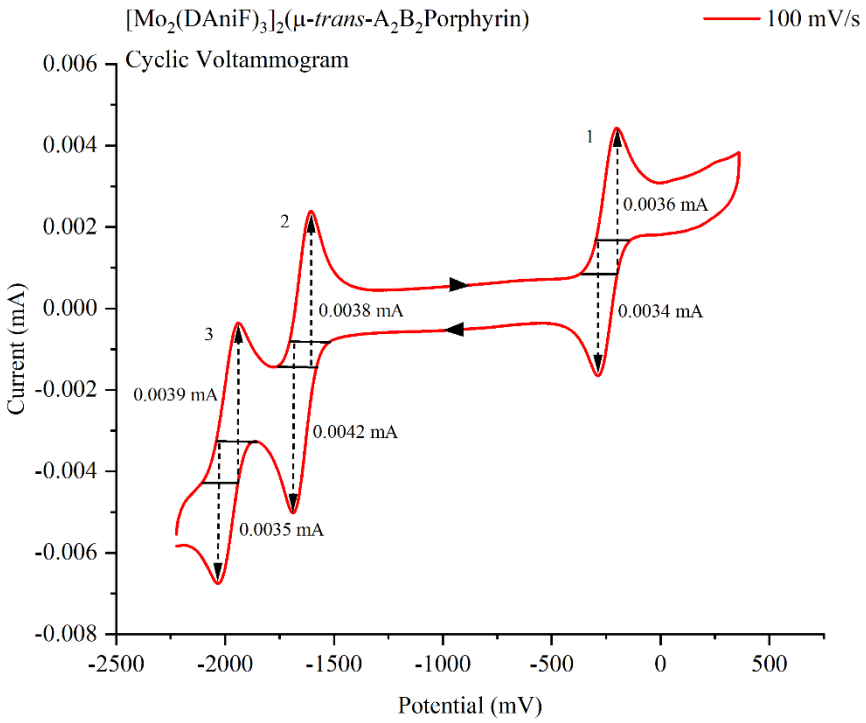

Figure 61: $[Mo_2(DAniF)_3]_2$(μ-*trans*-A_2B_2Porphyrin) (**8**) Cyclic Voltammogram (100 mV/s vs Fc/Fc^{+}, 0.1 M $[n\text{-}Bu_4][PF_6]$ in THF, 298 K)

Table 13: $[Mo_2(DAniF)_3]_2$(μ-*trans*-A_2B_2Porphyrin) (**8**) CV Peaks

CV Peak	Assignment	$\Delta E_{1/2}$ (mV)	i_{pc}/i_{pa}
1	Paddlewheel Oxidation	-243	1.1
2	1st Porphyrin reduction	-1687	0.90
3	2nd Porphyrin reduction	-1982	1.1

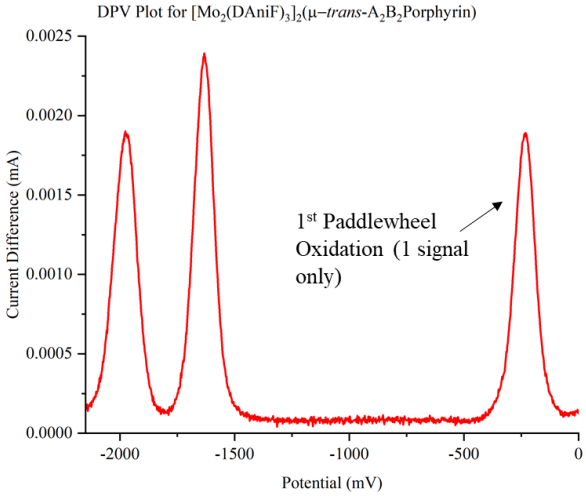

Figure 62: Differential Pulse Voltammetry (DPV) plot (vs Fc/Fc^+, 0.1 M [n-Bu_4][PF_6] in THF, 298 K) for [Mo_2(DAniF)$_3$]$_2$(μ-*trans*-A_2B_2Porphyrin) (**8**)

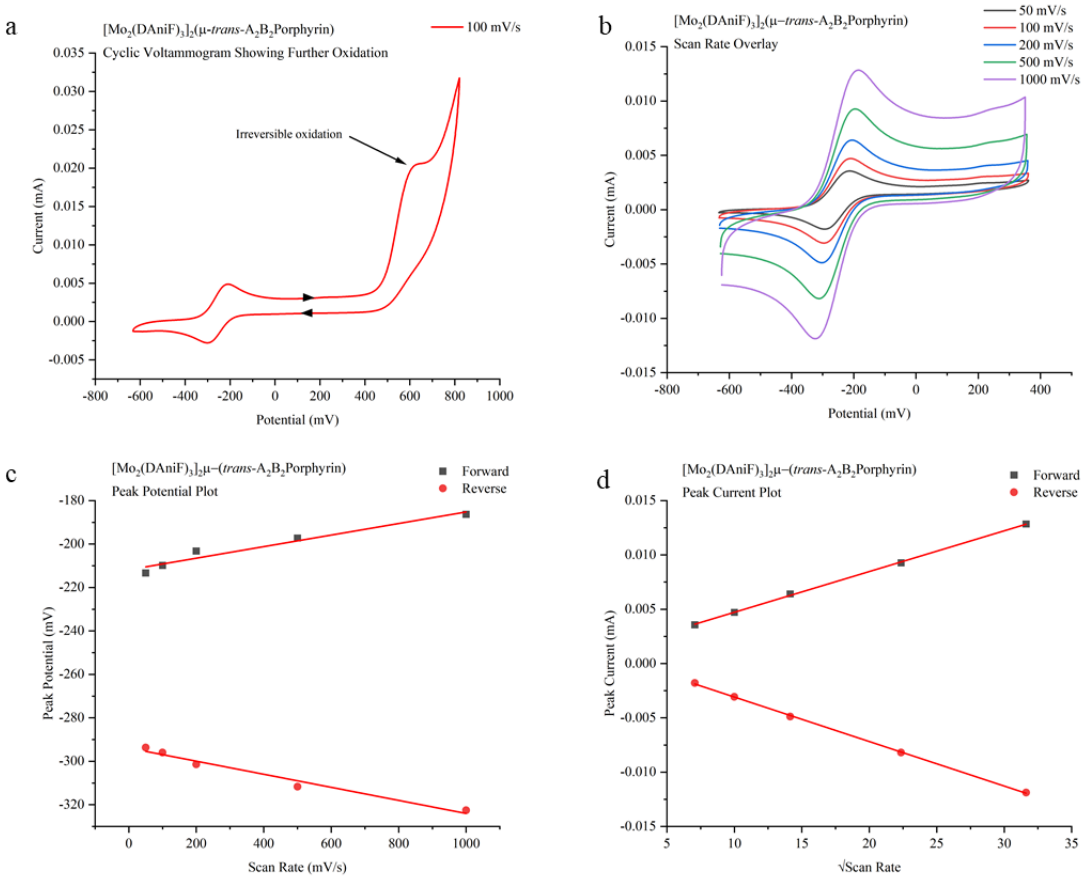

Figure 63: CV Plots (vs Fc/Fc^+, 0.1 M [n-Bu_4][PF_6] in THF, 298 K) for [Mo_2(DAniF)$_3$]$_2$(μ-*trans*-A_2B_2Porphyrin) (**8**) **a)** Cyclic voltammogram showing irreversible oxidation (100 mV/s), **b)** Scan rate overlay for 1st paddlewheel oxidation, **c)** Peak potential vs scan rate for 1st paddlewheel oxidation, **d)** Peak current vs √scan rate for 1st paddlewheel oxidation

The cyclic voltammograms for the two conjugates were essentially identical when overlayed alongside each other in **Figure 64**, and the position of the paddlewheel oxidation did not shift from the reference paddlewheel $Mo_2(DAniF)_3(OAc)$. Thus, the electrochemistry results provided no evidence for electronic communication between the paddlewheel and porphyrin units, as communication should lead to a shift in the $\Delta E_{1/2}$ values if at least one of the oxidised/reduced states could be stabilised by resonance owing to orbital mixing between the paddlewheel and porphyrin units.

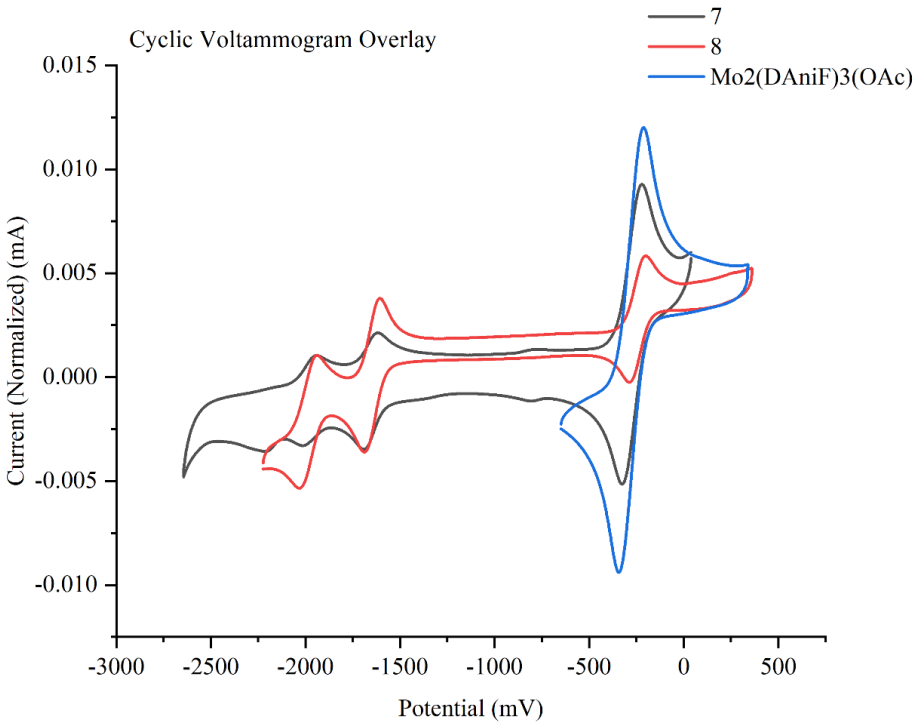

Figure 64: CV Overlay for $Mo_2(DAniF)_3(A_3BPorphyrin)$ (**7**), $[Mo_2(DAniF)_3]_2$(μ-*trans*-A_2B_2Porphyrin) (**8**) and $Mo_2(DAniF)_3(OAc)$ (Starting complex) (100 mV/s vs Fc/Fc^+, 0.1 M $[n\text{-}Bu_4][PF_6]$ in THF, 298 K)

UV/Vis analysis of **7** and **8** showed similar spectral features for both the conjugates and the starting A_3BPorphyrin (**Figure 65**, **Table 14**). Each consists of an intense Soret band at 418 nm and 4 Q-bands in the region 510-650 nm. The spectral features of the paddlewheel units are swamped by the intense porphyrin absorptions but would be expected to consist of a δ-δ* absorption band around 400 nm (for $Mo_2(DAniF)_3(OAc)$ appears at 416 nm), hidden here by the Soret band, and a δ→π* transition around 300 nm. The spectral characteristics of the porphyrin appear essentially unaffected by covalent attachment to the paddlewheel unit(s), although for $[Mo_2(DAniF)_3]_2$(μ-*trans*-A_2B_2Porphyrin) the Q-bands appear less well resolved. Overall, similar to the electrochemistry results, UV/Vis analysis did not evidence electronic communication between the paddlewheels and porphyrins.

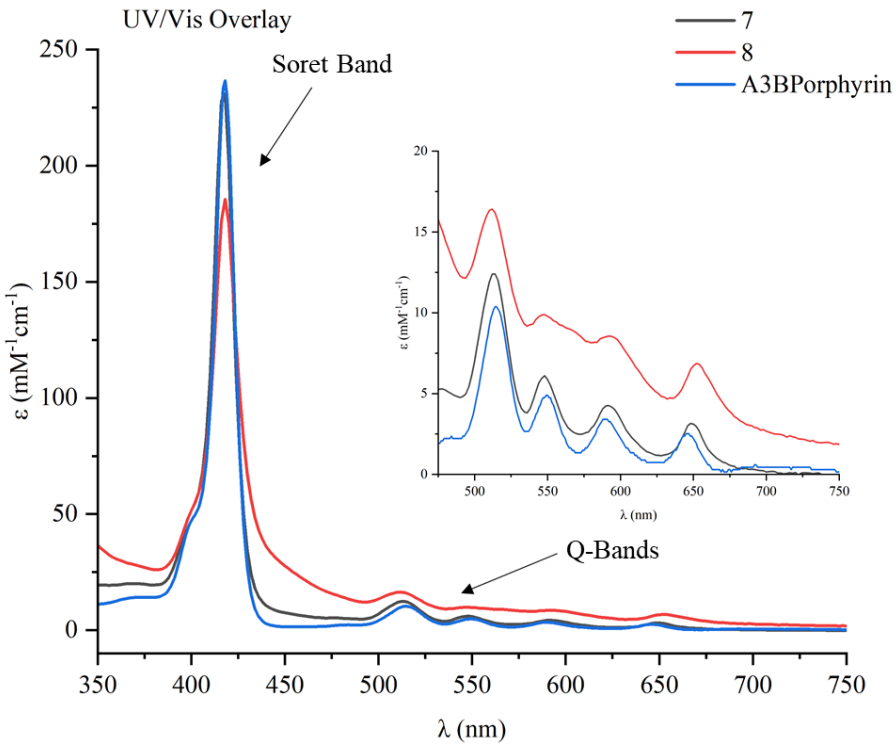

Figure 65: UV/Vis Spectra for $Mo_2(DAniF)_3(A_3BPorphyrin)$ (**7**) (0.0044mM in THF, 298 K), $[Mo_2(DAniF)_3]_2$(μ-*trans*-A_2B_2Porphyrin) (**8**) (0.0047 mM in THF, 298K), $A_3BPorphyrin$* (0.0068 mM in THF, 298 K) (*Data collected by Imogen Walsh)

Table 14: UV/Vis data for Paddlewheel/Porphyrin Conjugates **7** and **8**

Sample	**Soret Band (nm)**	**Q-band (nm)**			
$Mo_2(DAniF)_3(A_3BPorphyrin)$ (**7**)	418	512	548	592	650
$[Mo_2(DAniF)_3]_2$(μ-*trans*-A_2B_2Porphyrin) (**8**)	418	512	548	592	652
$A_3BPorphyrin$	418	514	549	590	646

Computational studies

To gain a rationale for these observations, DFT (density functional theory) calculations on model complexes **7'** and **8'** were conducted, where TiPB$^-$ was replaced with ^-O_2CMe and DAniF was replaced with dimethylformamidinate (DMeF$^-$) to reduce computational expense. Calculations were conducted using the Gaussian 16 suite with B3LYP/genecp functional, and a mixed basis set approach utilising 6-31g (d) for H, C, N, O and def2svpp for Mo.[76]

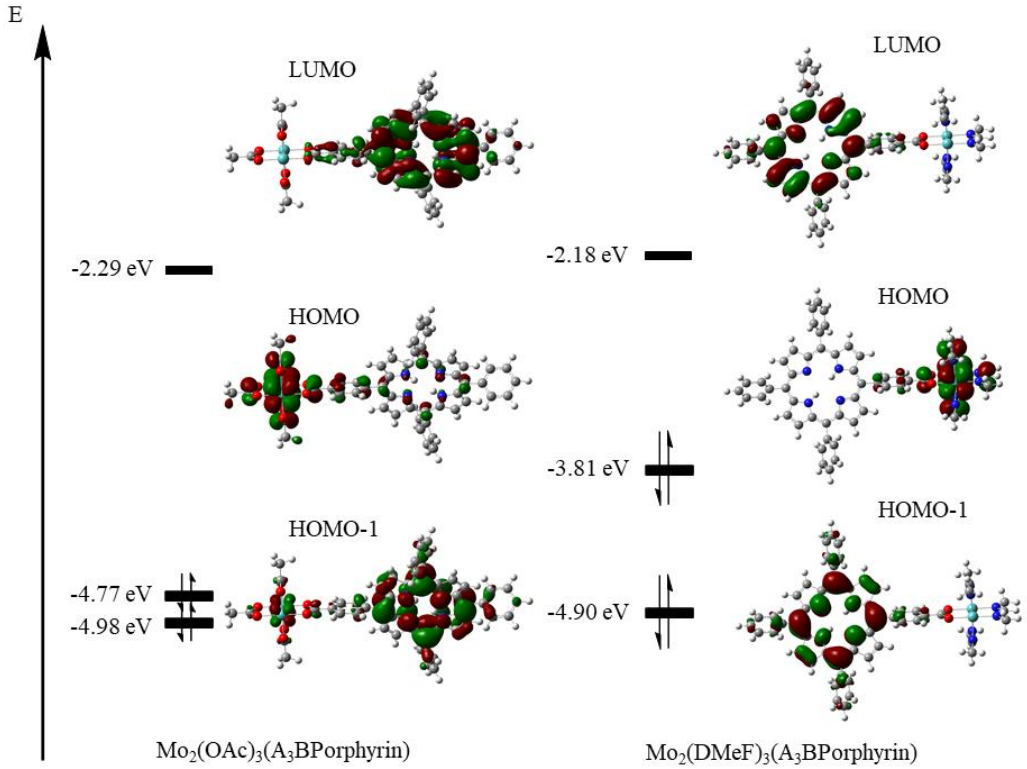

Figure 66: Frontier molecular orbitals for (left) $Mo_2(OAc)_3(A_3BPorphyrin)$ (**1'**) and (right) $Mo_2(DMeF)_3(A_3BPorphyrin)$ (**7'**). B3LYP/genecp, 6-31g (d): H C N O, def2svpp: Mo

DFT calculations for the carboxylate paddlewheel-porphyrin conjugate **1'** show slight Mo_2-porphyrin electronic coupling in the paddlewheel δ-based HOMO and the porphyrin π-based HOMO-1 (**Figure 66**, left). This effect arises because the porphyrin π system lies relatively close in energy to the Mo_2 δ orbitals, and for calculations of **1'** the HOMO and the HOMO-1 lie only 0.21 eV apart. However, when the O-donor based ^-OAc ligand is swapped for the more electron donating N-donor DMeF (**7'**) (**Figure 66**, right) the energy of the Mo_2 δ HOMO is raised from -4.77 eV to -3.81 eV, an increase of 0.96 eV, while the porphyrin-based HOMO-1 stays at roughly the same energy (-4.98 vs -4.90 eV). Due to the rise in the Mo_2 energy, the δ orbitals cannot overlap effectively with the porphyrin π-system. The same is true for the porphyrin-bridged system $[Mo_2(DMeF)_3]_2$(μ-*trans*-A_2B_2Porphyrin) (**8'**) (**Figure 67**). In this case there are two filled Mo_2 based δ orbitals at almost identical energies, presumably due to some asymmetry

between the two paddlewheel units, but a drop of 1.01 eV to the highest filled porphyrin π orbital- too large once again for any meaningful interaction between the two. The more electron donating nature of the formamidinate ligands, and their resultant non-lability was the very property that allowed the complexes to be prepared cleanly without the over-substitution seen for the TiPB based complexes, but these computational data show that this also removes the possibility for significant electronic interaction between the paddlewheel and the porphyrin.

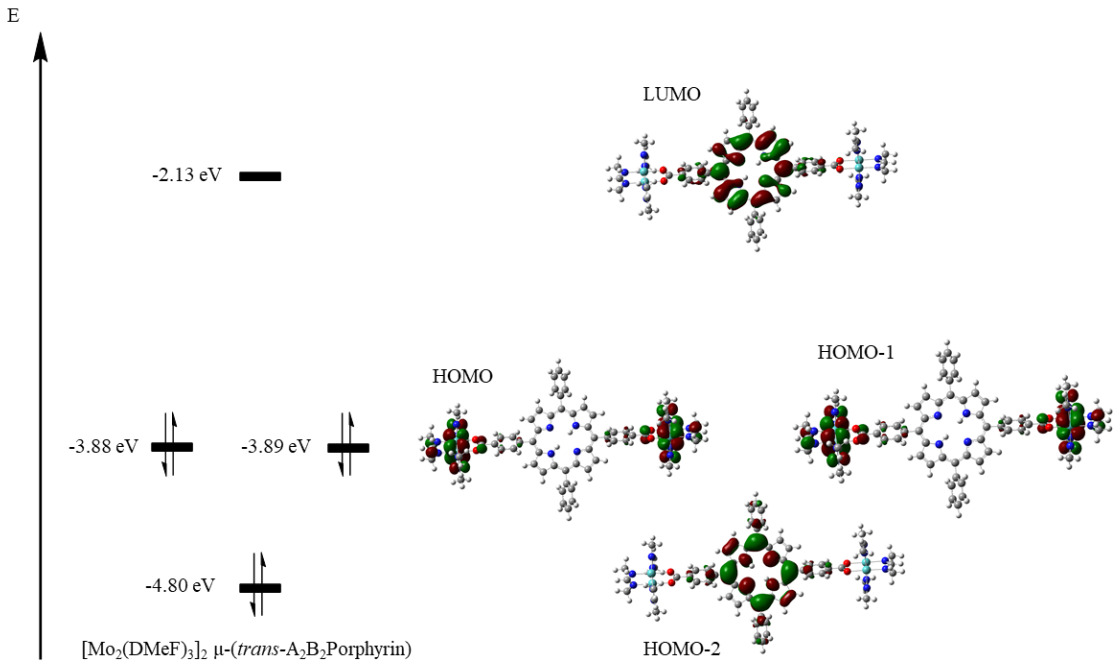

Figure 67: Frontier orbitals for $[Mo_2(DMeF)_3]_2$(μ-*trans*-A_2B_2Porphyrin). B3LYP/genecp, 6-31g (d): H C N O, def2svpp: Mo

Tuning of the energy levels of the frontier orbitals will be required for meaningful electronic communication in formamidine-based paddlewheel-porphyrin conjugates. However, there are several different ways this could be achieved. For instance, the gap between the filled Mo_2 δ HOMO and the porphyrin-based LUMO could be reduced to facilitate δ-π* mixing. This would involve either raising the Mo_2 δ orbitals with a highly electron donating ligand set (although this could increase air-sensitivity) and/or reducing the porphyrin π* energy with electron withdrawing porphyrin substituents. Alternatively, Mo_2 δ-porphyrin π orbital mixing could be encouraged by either raising the energy of the porphyrin π system with peripheral electron-donating substituents or, reducing the Mo_2 δ energy by introducing highly electron-withdrawing formamidinates.

Fluorinated Paddlewheel complexes

A series of fluorinated paddlewheel complexes were prepared with a view to determine how different fluorination patterns affect the redox and spectroscopic properties of quadruply bonded dimolybdenum paddlewheel complexes. Of particular interest was the energy of the Mo_2 δ energy levels, which is known to affect metal ligand coupling when tethered to organic linker units, and DFT calculations have suggested that reducing the δ energy with electron withdrawing substituents could potentially improve communication with porphyrins in the systems discussed above. It was also of interest to investigate whether fluorination could improve the air stability of paddlewheel complexes.

The homoleptic fluorinated paddlewheel complexes depicted in **Figure 68** were prepared directly from $Mo(CO)_6$ and the relevant N,N'-di(fluoroaniline)formamidinate (DFArF) ligand, with the reaction scheme outlined in **Figure 69**. Samples were characterised by MALDI-TOF MS, ^{1}H and ^{19}F NMR spectroscopy, and single crystal x-ray diffraction (XRD). The redox properties of these paddlewheels were subsequently evaluated by CV (THF solution, vs Fc/Fc^{+}), and the optical properties by UV/Vis spectroscopy.

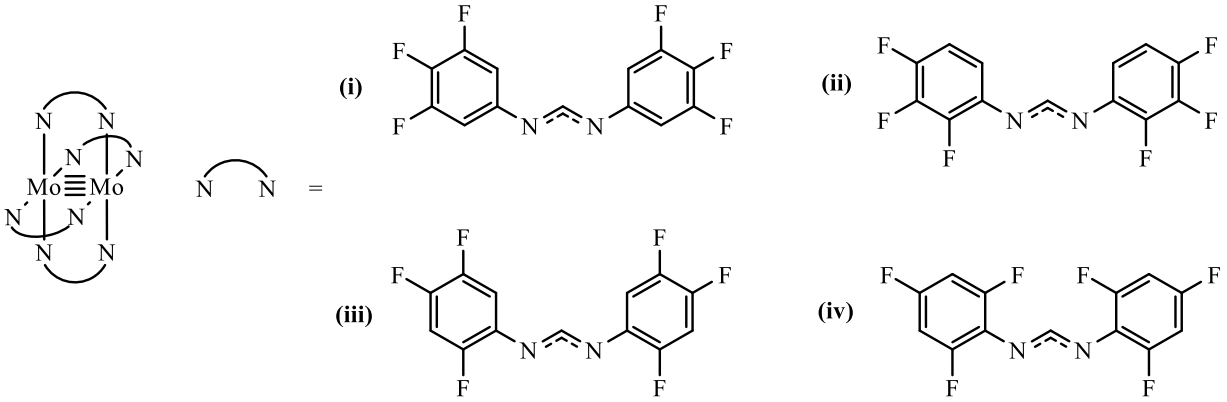

Figure 68: Fluorinated paddlewheel complexes **i-iv** prepared from DFArF ligands

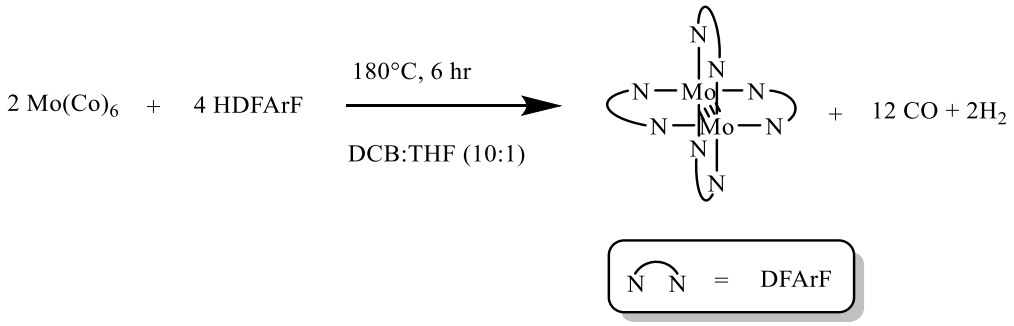

Figure 69: Generalised reaction scheme for $Mo_2(DFArF)_4$

Cyclic Voltammetry

A fully reversible 1 electron oxidation of Mo_2(2,3,4-DFArF)$_4$ (**ii**) was observed at +164 mV relative to the Fc/Fc^+ couple (**Figure 70**, a). The forward and reverse peaks drift apart as the scan rate increases (**Figure 70**, **b**,**c**), indicative of slightly sluggish electron transfer kinetics- limited by diffusion of the paddlewheel complex through solution. The only major difference in the CV data for the different fluorinated paddlewheels was the redox potential this oxidation process occurs, depicted graphically in **Figure 71**.

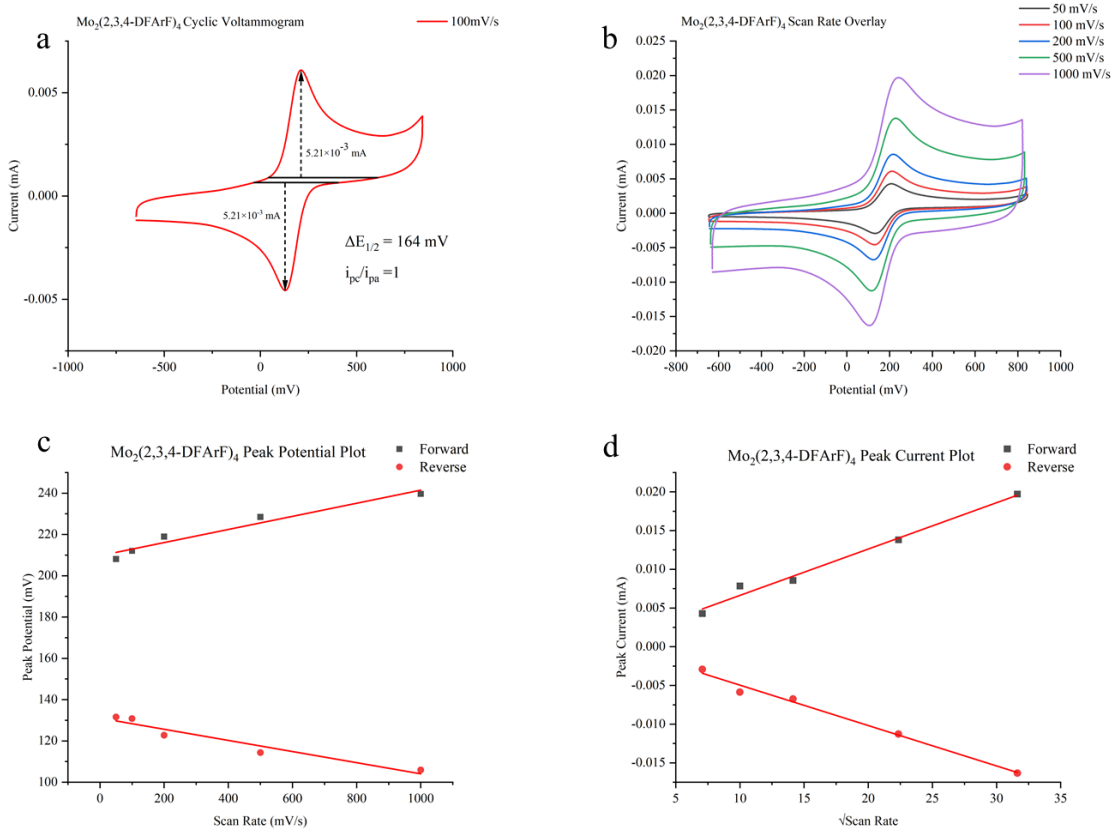

Figure 70: CV Plots (vs Fc/Fc^+, 0.1 M [n-Bu_4][PF_6] in THF, 298 K) for Mo_2(2,3,4-DFArF)$_4$ (**ii**) **a)** Cyclic voltammogram showing 1st paddlewheel oxidation (100 mV/s), **b)** Scan rate overlay for 1st paddlewheel oxidation, **c)** Peak potential vs scan rate for 1st paddlewheel oxidation, **d)** Peak current vs √scan rate for 1st paddlewheel oxidation

The redox potentials (for the 1st paddlewheel oxidation) varied over a 230 mV range depending on the substitution pattern at the ligand periphery. It is thought that the redox potential of the paddlewheel is directly linked to the electron withdrawing ability of the fluorinated ligands, as pulling electron density away from the dimolybdenum core lowers the δ energy level with the consequence that the complex becomes more difficult to oxidize. This is most clear when comparing the fluorinated formamidinates to the more electron donating DAniF, which has an $Mo_2^{4+/5+}$ potential more than 300 mV lower than any of the fluorinated variants (**Table 15**). It is currently suggested that the electron withdrawing ability of the 4 fluorinated formamidinates

prepared here is strongly dependent on whether fluorination has taken place at the *ortho*-position. Fluorination at the *ortho* position may introduce additional steric strain on the ligand, causing the aromatic groups to twist out of plane hindering through-bond electron withdrawal. This would explain the relatively high redox potential of **i**, the similar potentials for **ii** and **iii** (both fluorinated once at the *ortho*- position), and the greatly lowered potential for **iv.** In the literature, this effect was demonstrated by a loose correlation between the torsion angle (defined between the aromatic ring and the M_2 centre), and the $M_2^{4+/5+}$ redox potential (although in this case different ancillary ligands were used).[32] A similar investigation was conducted here, but no convincing correlation between the two was found. It is worth noting the torsion angles were extracted from the solid-state crystal structures of the paddlewheel complexes whilst the CV experiments took place in solution where the aromatic groups are likely to have much more rotational freedom. A better understanding of the barrier to rotation of the aromatic groups under experimental conditions would be required to probe this effect further.

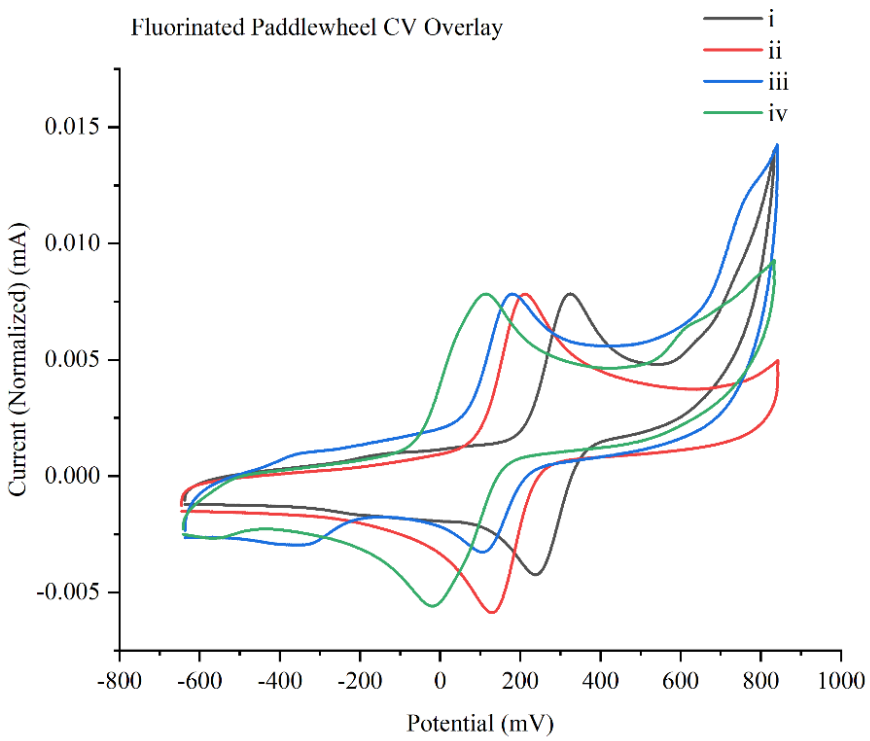

Figure 71: CV overlay (100 mV/s vs Fc/Fc^+, 0.1 M $[n\text{-}Bu_4][PF_6]$ in THF, 298 K) for fluorinated paddlewheel complexes Mo_2(3,4,5-DFArF)$_4$ (**i**), Mo_2(2,3,4-DFArF)$_4$ (**ii**), Mo_2(2,4,5-DFArF)$_4$ (**iii**), Mo_2(2,4,6-DFArF)$_4$ (**iv**)

Table 15: $\Delta E_{1/2}$ (vs Fc/Fc^{+}) values for the 1st oxidation of fluorinated paddlewheel complexes **i-iv**

Paddlewheel	$\Delta E_{1/2}$ (mV)
Mo_2(3,4,5-DFArF)$_4$ (i)	281
Mo_2(2,3,4-DFArF)$_4$ (ii)	164
Mo_2(2,4,5-DFArF)$_4$ (iii)	141
Mo_2(2,4,6-DFArF)$_4$ (iv)	48
Mo_2(DAniF)$_3$(OAc) (Reference)	-277

Crystallography

The crystal structures of the fluorinated paddlewheel complexes are depicted in **Figures 72-75**, and clearly show the central paddlewheel motif, which is surrounded by aromatic ligands twisting out of plane to varying degrees. The Mo-Mo bond lengths from the XRD structures were ~2.1 Å for all the fluorinated paddlewheel complexes (**Table 16**). This is consistent with Mo-Mo quadruple bond formation and matches values reported in the literature for similar complexes.[27] There were small changes to the (average) Mo-N bond length upon variation of the fluorination pattern, which vary from 2.157 to 2.170 Å (**Table 16**). Furthermore, there is a loose negative correlation between the Mo-N bond length and the potential of the $Mo_2^{4+/5+}$ redox couple (**Figure 76**). Since the Mo-N bond length is an indirect measure for the strength of the interaction between the ligand and the metal centre, it is perhaps an intuitive result that the ligands that interact strongly with the metal centre and have short Mo-N bonds raise the redox potential higher than ligands with weaker interactions and longer metal-ligand bonds.

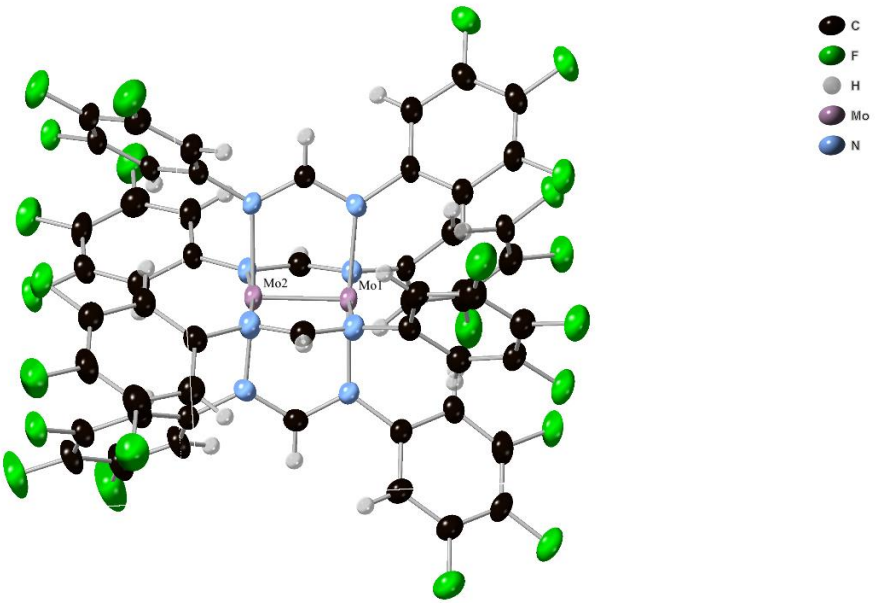

Figure 72: Crystal structure (thermal ellipsoid plot) of Mo_2(3,4,5-DFArF)$_4$ (**i**) from XRD

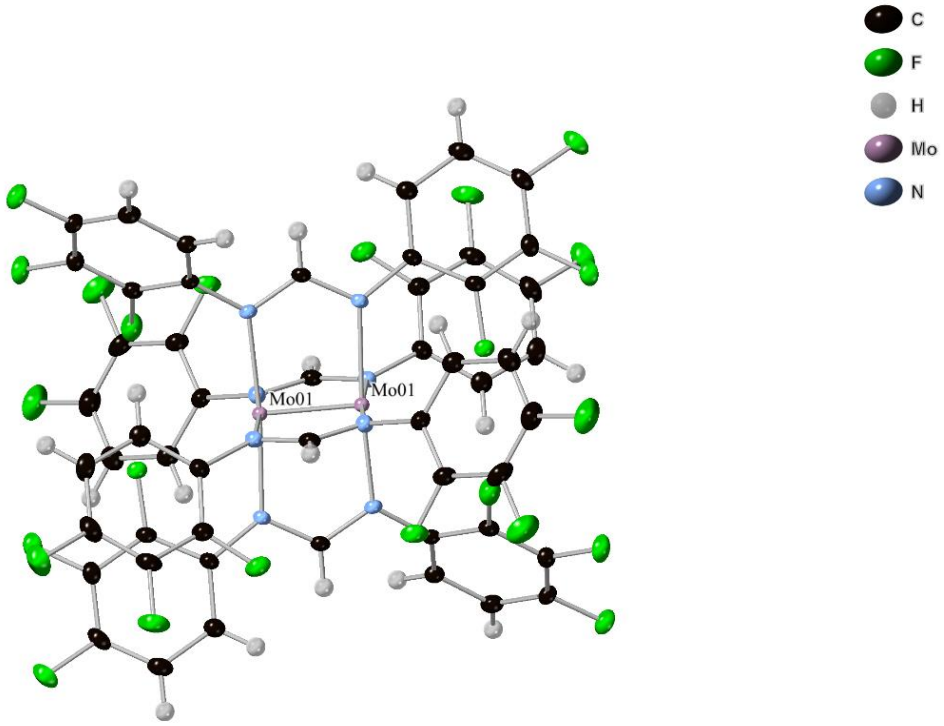

Figure 73: Crystal structure (thermal ellipsoid plot) of Mo_2(2,3,4-DFArF)$_4$ (**i**) from XRD

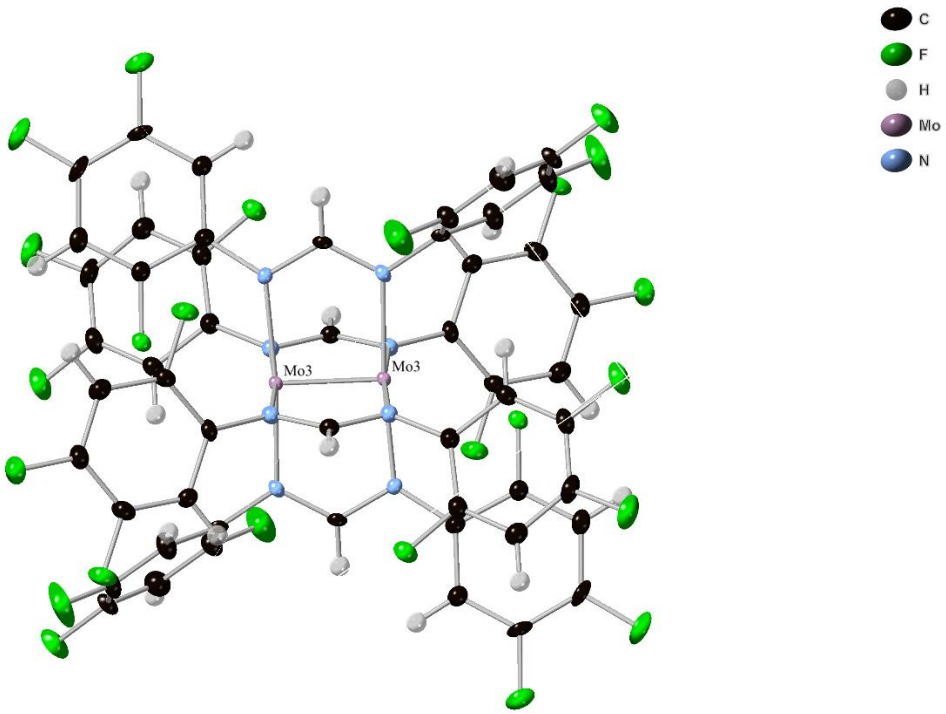

Figure 74: Crystal structure (thermal ellipsoid plot) of Mo_2(2,4,5-DFArF)$_4$ (**i**) from XRD

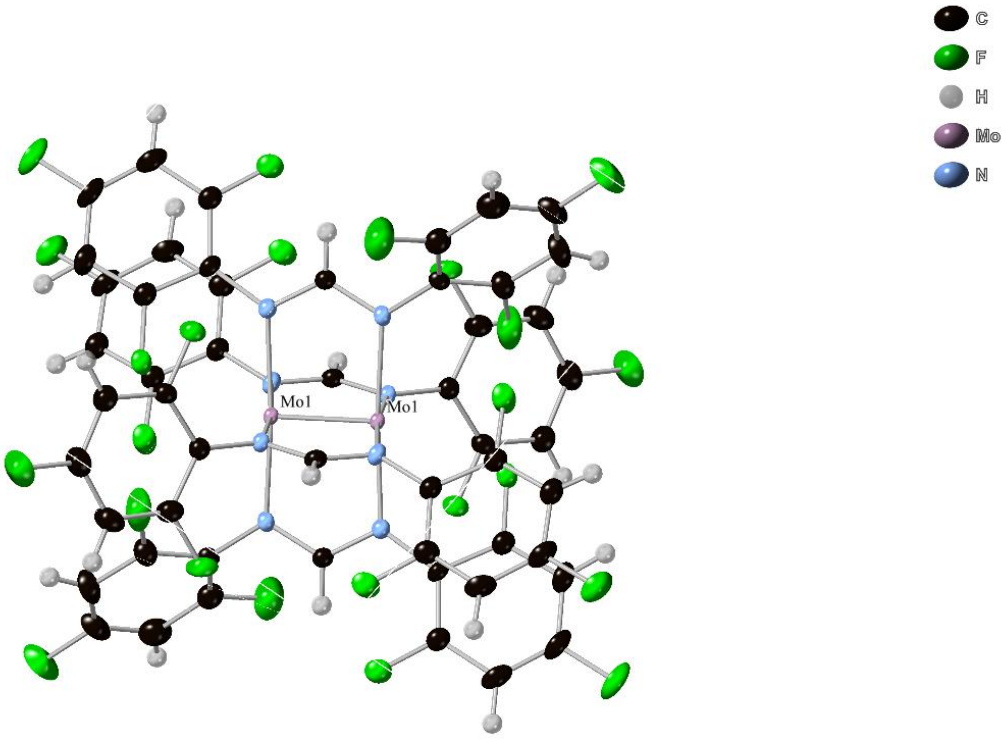

Figure 75: Crystal structure (thermal ellipsoid plot) of Mo_2(2,4,6-DFArF)$_4$ (**i**) from XRD

Table 16: Mo-Mo and Mo-N bond lengths for fluorinated paddlewheel complexes (from single crystal structures)

Fluorinated Paddlewheel	Mo-Mo bond length (Å) (esd)	Average Mo-N bond length (Å) (esd)
Mo_2(3,4,5-DFArF)$_4$ (i)	2.092 (7)	2.157 (10)
Mo_2(2,3,4-DFArF)$_4$ (ii)	2.102 (12)	2.165 (7)
Mo_2(2,4,5-DFArF)$_4$ (iii)	2.100 (52)	2.158 (12)
Mo_2(2,4,6-DFArF)$_4$ (iv)	2.102 (59)	2.170 (7)

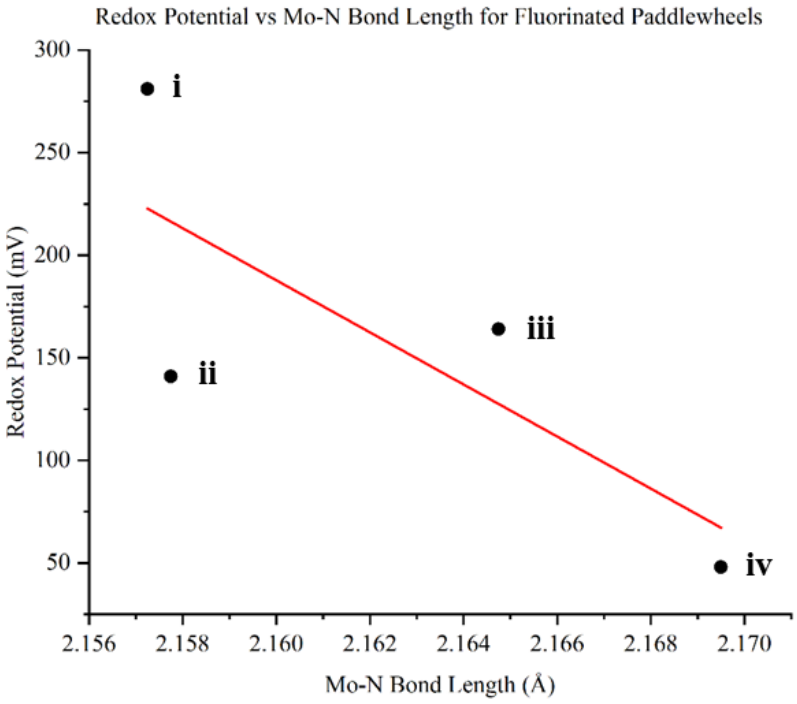

Figure 76: Graph showing relationship between $Mo_2^{4+/5+}$ redox potential and (average) Mo-N bond length for the fluorinated paddlewheel complexes **i-iv**

UV/Vis

The UV/Vis spectra for all the formamidinate paddlewheel variants are remarkably similar, consisting of an intense peak at 300 nm, likely a MLCT from the Mo_2 δ system to one of the ligand π combinations (**Figure 77**, **Table 17**).[31] There is also a less intense, lower energy peak at around 416 nm corresponding to the Mo_2 δ→δ*, the HOMO→LUMO transition in these complexes. The broad peak at around 400 nm for (**iii**) is thought to be a consequence of impurities in the sample and masks the δ→δ* transition. Overall, the peripheral substitution makes little to no difference to the spectral features of these formamidinate based paddlewheel complexes, even when comparing the fluorinated analogues to the much more electron donating methoxy analogue ($Mo_2(DAniF)_3(OAc)$. This is because although fluorination pulls electron density away from the Mo_2, lowering the Mo_2 δ HOMO, the LUMO is similarly reduced in energy so the gap between them remains the same.

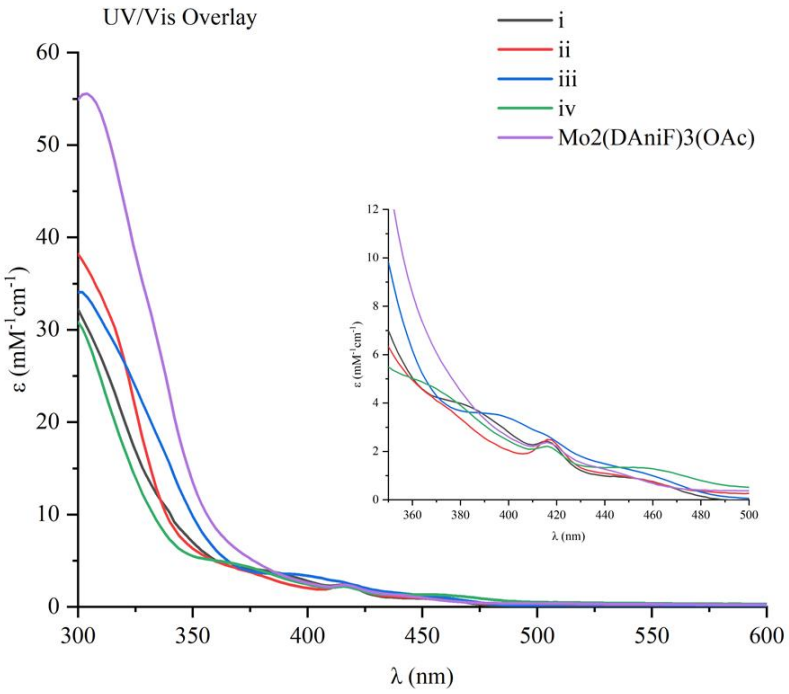

Figure 77: UV/Vis Spectra for Mo_2(3,4,5-DFArF)$_4$ (**i**) (0.021 mM in THF, 298 K), Mo_2(2,3,4-DFArF)$_4$ (**ii**) (0.021 mM in THF, 298 K), Mo_2(2,4,5-DFArF)$_4$ (**iii**) (0.035 mM in THF, 298 K), Mo_2(2,4,6-DFArF)$_4$ (**iv**) (0.026 mM in THF, 298 K), Mo_2(DAniF)$_3$(OAc) (0.020 mM in THF, 298 K)

Table 17: UV/Vis data for fluorinated paddlewheel complexes **i-iv**

Compound	δ→π transition (nm)	δ→δ* transition (nm)
Mo_2(3,4,5-DFArF)$_4$ (**i**)	300	416
Mo_2(2,3,4-DFArF)$_4$ (**ii**)	300	418
Mo_2(2,4,5-DFArF)$_4$ (**iii**)	302	-
Mo_2(2,4,6-DFArF)$_4$ (**iv**)	300	416
Mo_2(DAniF)$_3$(OAc)	304	416

The effect of fluorination on the air-stability of these complexes is also of interest to this project. Ideally, this would be determined by taking repeated UV/Vis measurements over time of these complexes exposed to air, and charting decomposition through changes to the key spectral features, but time constraints in the laboratory prevented this. Anecdotally however, fluorination makes a significant difference to air stability. The reference paddlewheel complex Mo_2(DAniF)$_3$(OAc) is very sensitive to air and decomposes within seconds of exposure, observed as a swift colour change from yellow to black. All the fluorinated variants, however, are tolerant to atmospheric oxygen in the solid state and are bench stable (by eye) on the timescale of days to weeks.

Conclusions and Further Work

Synthetic procedures for paddlewheel-porphyrin conjugates with carboxylate and formamidinate ligands have been developed over the course of this project. The use of carboxylate ligands however, invariably led to a degree of over-substitution and a mixture of products, which could not easily be separated to give a pure final product. The synthesis of conjugates with formamidinate ancillary ligands proved more successful and could be isolated cleanly provided an excess of porphyrin was added to the reaction mixture. Two of these complexes, $Mo_2(DAniF)_3(A_3BPorphyrin)$ (**7**) and $[Mo_2(DAniF)_3]_2$(μ-*trans*-A_2B_2Porphyrin) (**8**) were analysed by cyclic voltammetry and UV/Vis spectroscopy. Covalent attachment of paddlewheel to porphyrin appeared to have no effect on the redox potential of the $Mo_2^{4+/5+}$ redox couple, and in the case of (**8**), no mixed valence characteristics were found. It was therefore concluded that there was little to no electronic communication between paddlewheel and porphyrin. Furthermore, the intense absorption of the porphyrin swamped paddlewheel spectral features in the UV/Vis spectra, and the key features of the porphyrin remained unchanged from the starting material. These results were rationalised by DFT calculations, which suggested that the more electron donating formamidinate ligands raised the Mo_2 δ energy by around 1 eV so that overlap with porphyrin π-system was no longer possible. Therefore, tuning of the electronic structure of these complexes will be required to observe orbital overlap between the two components, which could be achieved by changing the peripheral substitution on either the paddlewheel or the porphyrin. Work is currently being undertaken to assess the suitability of fluorinated formamidinates for this, which may have the added effect of improving air-stability, although thus far these have only been explored in homoleptic systems. Alternatively, size exclusion chromatography could potentially be employed to separate the mixtures generated by the carboxylate-based paddlewheel-porphyrin conjugate syntheses, which yielded complexes with similar solubilities but different sizes, although this is currently untested on these air-sensitive systems. Once a next generation of paddlewheel-porphyrin conjugates have been prepared, further characterisation such as XRD analysis and spectroelectrochemistry will be required, alongside more in-depth computational studies to better understand both the chemical and electronic structures of these complexes.

Experimental

Materials and Methods

Tetracarboxphenylporphyrin (B_4Porphyrin) was synthesised according to a procedure previously reported in Imogen Walsh's BSc thesis, and the sample used here was left over from a previous project. All other reagents were obtained from commercial sources and used as received. NaOMe (0.5 M in methanol) was stored under an inert atmosphere. Ethanol, 1,2-dichlorobenzene, and chloroform-*d* were distilled, sparged with nitrogen and stored in an inert atmosphere prior to use. All other solvents were obtained from a Grubbs-type solvent purification system and were sparged with nitrogen prior to use, and in the case of THF stored over activated molecular sieves. All reactions involving paddlewheel complexes were performed and worked-up under an inert atmosphere using standard Schlenk line techniques.

Instrumentation

All NMR spectra were recorded on a Bruker Advance 300, 400, or 600 MHz spectrometer and referenced to the residual solvent peaks of chloroform-*d* at 7.26 or 77.2 ppm, or in some cases DMSO-d_6 at 2.50 or 39.52 ppm. Mass spectrometry analyses were conducted by Karl Heaton and Chris Goult, University of York, using a Bruker compact® time of flight mass spectrometer for ESI, and an ultrafleX III MALDI-TOF/TOF instrument for MALDI (with a dithranol maxtrix). X-ray crystallography was conducted by Adrian Whitwood and Theo Tanner, University of York using an Oxford Diffraction SuperNova equipped with a 4-circle goniometer, microfocus Mo & Cu X-ray sources and CCD detector. Elemental analysis was also conducted by Adrian Whitwood, using an Exeter Analytical Inc. CE-440 analyser. UV/Vis spectra were measured on a Jasco V-560 UV/Vis spectrophotometer with a Young's tap adapted cuvette. Cyclic voltammograms were recorded under an argon atmosphere, in a 0.1 M [n-Bu_4][PF_6] THF solution with a Gamry reference 600TM potentiostat, with a glassy carbon working electrode (diameter = 3.3 mm), an Ag/AgCl reference electrode, and a Pt wire counter electrode. Potentials are reported relative to Fc/Fc^+ couple, with ferrocene added as an internal reference at the end of each experiment.

Synthesis

General Procedure for A_nB_{4-n}Porphyrin methyl ester

Methyl 4-formylbenzoate (2.00 g, 12.18 mmol) and benzaldehyde (2.87 g, 27.04 mmol) were dissolved in 100 cm^3 of propionic acid. The solution was heated to 140°C, and pyrrole (2.41 g, 35.92 mmol) as added dropwise by syringe over 30 min, and the solution was heated at reflux temperature for 2 hr. The solution was cooled to room temperature and the solvent was removed under reduced pressure. The resultant solid was washed with ethanol and filtered. The precipitate was extracted into THF, and the solvent subsequently removed by rotary evaporation to leave a solid product. The crude product was purified by silica gel chromatography with a DCM mobile phase and was dry-loaded with celite onto the column.

The first fraction to elute was tetraphenyl porphyrin, which was discarded.

The second fraction to elute was A_3BPorphyrin methyl ester, which upon removal of solvent was obtained as a dark purple crystalline solid. Yield: 11% (0.71 g, 1.06 mmol). **^{1}H NMR** (400 MHz, chloroform-*d*) δ_H ppm: 8.87-8.84 (6H, m, *d*), 8.79 (2H, d, $^3J_{H-H}$ = 5 Hz, *c*) 8.44 (2H, d, $^3J_{H-H}$ = 8.5 Hz, *a*/*b*), 8.30 (2H, d, $^3J_{H-H}$ = 8.5 Hz), 8.23-8.19 (6H, m, *f*), 7.80-7.72 (9H, m, *e*,*g*), 4.11 (3H, s, *h*), -2.79 (2H, s, *i*). **ESI MS:** calc. for $C_{46}H_{32}N_4O_2$ $[M-H]^+$ m/z 672.2525, found m/z 673.2615 $[M + H]^+$.

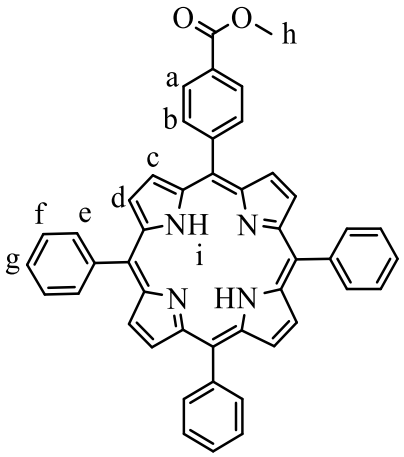

Third fraction to elute was a mixture of *cis/trans*-A_2B_2Porphyrin methyl ester. This fraction was re-columned under the same conditions multiple times to separate the two. The *trans*-A_2B_2Porphyrin methyl ester was isolated as a dark purple crystalline powder. Yield: 6% (0.42 g, 0.58 mmol). **^{1}H NMR** (400 MHz, chloroform-*d*) δ_H ppm: 8.87 (d, $^3J_{H-H}$ = 4.9 Hz, 4H, *c/d*), 8.79 (d, *J* = 4.9 Hz, 4H, *c/d*), 8.44 (d, $^3J_{H-H}$ = 7.9 Hz, 4H *a/b*), 8.30 (d, $^3J_{H-H}$ = 8.1 Hz, 4H, *a/b*), 8.21 (m, 4H, *f*), 7.77 (m, 6H, *e*,*g*), 4.11 (s, 6H, *h*), -2.80 (s, 2H, *i*). **ESI MS:** calc. for $C_{48}H_{34}N_4O_4$ $[M-H]^+$ m/z 730.2580, found m/z 731.2662 $[M + H]^+$.

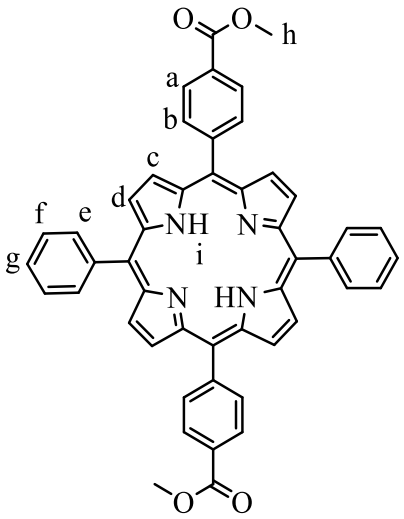

Zn-A$_3$BPorphyrin methyl ester

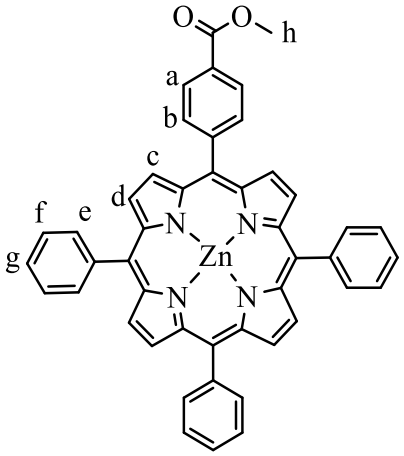

A_3BPorphyrin methyl ester (0.25g, 0.36 mmol) was dissolved in 30 cm^3 of DCM. $Zn(OAc)_2$ (0.66 g, 3.6 mmol) was dissolved in 15 cm^3 methanol, and added to the porphyrin solution. The resulting solution was stirred at room temperature for 2 hr. The solvent was removed under reduced pressure, and the product extracted into the organic phase with a 1:2 DCM: water mixture. The DCM layer was separated and dried under magnesium sulfate. The product was recrystallized with methanol, and the solvent removed by rotary evaporation to isolate a dark purple powder. The yield was not calculated. **^{1}H NMR** (400 MHz, chloroform-*d*) δ_H ppm: 8.97-8.94 (6H, m, *d*), 8.89 (2H, d, $^3J_{H-H}$ = 5 Hz, *c*) 8.43 (2H, d, $^3J_{H-H}$ = 8 Hz, *a*/*b*), 8.31 (2H, d, $^3J_{H-H}$ = 8 Hz), 8.24-8.20 (6H, m, *f*), 7.80-7.72 (9H, m, *e* and *g*), 4.10 (3H, s, *h*). **ESI MS:** calc. for $C_{46}H_{30}N_4O_2Zn$ $[M + H]^+$ m/z 734.1660, found m/z 735.1733 $[M + H]^+$.

General procedure for hydrolysis of porphyrin methyl ester

The porphyrin methyl ester was dissolved in 40 cm^3 of THF and 25 cm^3 distilled water. 20 cm^3 of 1 M aqueous KOH solution was added, and the mixture was heated at reflux temperature at 66°C for 48 hr. 20 cm^3 1 M aqueous HCl was added dropwise to adjust to pH 3. The mixture was filtered and washed with water, and the precipitate reclaimed by dissolution in DCM. The DCM was removed by rotary evaporation to yield a solid product.

(1) A_3BPorphyrin methyl ester (1.19 g, 1.77 mmol). The product was isolated as a dark purple powder. Yield: 33% (0.38g, 0.58 mmol). **^{1}H NMR:** (300 MHz, chloroform-d) δ_H ppm: 8.89-8.79 (8H, m, c and d), 8.51 (2H, d, $^3J_{H-H}$ = 8 Hz, a/b), 8.35 (2H, d, $^3J_{H-H}$ = 8Hz, a/b), 8.23-8.20 (6H, m, f), 7.81-7.73 (9H, m, e and g). **ESI MS:** calc. for $C_{45}H_{30}N_4O_2$ $[M-H]^+$ m/z 672.2525, found m/z 673.2616$[M + H]^+$

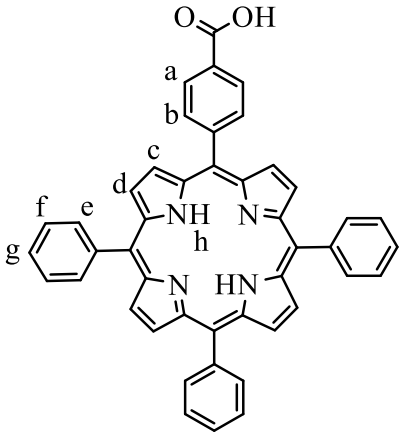

(2) Zn-A_3BPorphyrin methyl ester. The product was obtained as a dark purple powder. Yield: 27% (combined for zincation and hydrolysis) (0.071 g, 0.098 mmol) **^{1}H NMR:** (300 MHz, chloroform-*d*) δ_H ppm: 8.97-8.83 (8H, m, c and d), 8.48 (2H, d, $^3J_{H-H}$ = 8 Hz, a/b), 8.33 (2H, d, $^3J_{H-H}$ = 8 Hz, a/b), 8.22-8.18 (6H, m, f), 7.78-7.72 (9H, m, e and g). **APCI MS:** calc. for $C_{45}H_{28}N_4O_2Zn$ $[M-H]^+$ m/z 736.1817, found m/z 737.1779 [M + H]$^+$

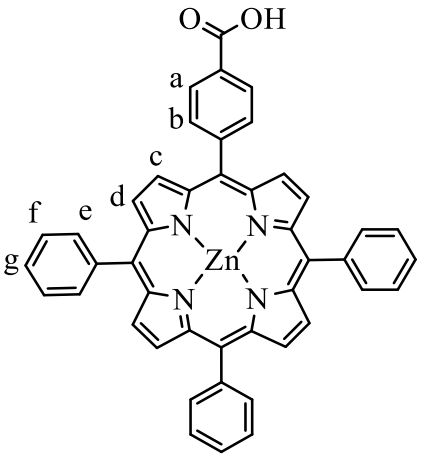

(3) Trans-A_2B_2Porphyrin methyl ester (0.43 g, 0.58 mmol). The product was isolated as a dark purple powder. Yield: 91% (0.37 g, 0.53 mmol). Confirmation reaction had gone to completion was provided by thin layer chromatography in DCM solution.

HDAniF

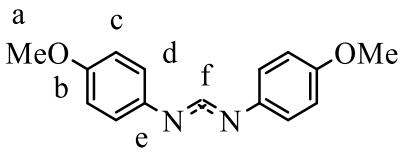

Triethyloformate (10 g, 67.5 mmol) and *p*-anisidine (6.70 cm^3, 58.2 mmol) were heated at reflux temperature (140°C) overnight. The crude product was recrystallized first with toluene, and subsequently with a toluene/petroleum ether mixture, and dried by rotary evaporation. The product was isolated as a white crystalline solid. Yield: 38.5% (5.75 g, 22.4 mmol). **^{1}H NMR** (300 MHz, chloroform-*d*) δ_H ppm: 8.01 (1H, s, *f*), 6.98 (4H, d, $^3J_{H-H}$ = 9 Hz, *c*), 6.84 (4H, d, $^3J_{H-H}$ = 9 Hz, *d*), 3.79 (6H, s, *a*). **^{13}C NMR** (75.5 MHz, chloroform-*d*) δ_C ppm: 158 (*b*), 148 (*f*), 139 (*e*), 120 (*c*), 115 (*d*), 56 (*a*).

Mo_2(TiPB)$_4$

$Mo(CO)_6$ (0.66 g, 2.50 mmol) and HTiPB (1.24 g, 5.00 mmol) were added to a 2-necked found-bottomed flask fitted with a condenser. The flask was placed under inert atmosphere, then 30 cm^3 1,2-DCB and 2 cm^3 THF were added by syringe. The mixture was heated at reflux temperature (160°C) for 48 hr. The solvent was removed under reduced pressure and the resulting solid was washed with hexane. The supernatant was removed by cannula and the process repeated. The resulting yellow powder was dried under reduced pressure and stored under an inert atmosphere. Yield: 35% (0.51 g, 0.44 mmol). **^{1}H NMR** (400 MHz, chloroform-*d*) δ_H ppm: 7.11 (s, 8H, *c*), 3.37 (spt, $^3J_{H-H}$ = 7 Hz, 8H, *b*), 2.94 (spt, $^3J_{H-H}$ = 7 Hz, 4H, *e*), 1.29 (d, $^3J_{H-H}$ = 6.9 Hz, 24H, *d*), 1.17 (d, $^3J_{H-H}$ = 6.7 Hz, 48H, *a*).

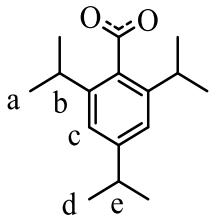

$Mo_2(TiPB)_3(A_3BPorphyrin)$ (1), reaction A

$Mo_2(TiPB)_4$ (0.1 g, 0.085 mmol) and $A_3BPorphyrin$ (0.056 g, 0.085 mmol) were added to a Schlenk tube under an inert atmosphere. 20 cm^3 THF and 0.5 M NaOMe in methanol (0.17 cm^3 0.085 mmol) were added by cannula and the solution was stirred for 48 hr at room temperature. The solvent was then evacuated under reduced pressure and the remaining solid washed with hexane. The mixture was filtered through celite, and the precipitate recovered by dissolution in THF. The THF was then evacuated to leave behind a greasy brown solid. Yield: 20% (0.027 g, 0.017 mmol). **^{1}H NMR** (400 MHz, chloroform-*d*) δ_H ppm: 8.94-8.80 (8H, m, *c* and *d*), 8.73 (2H, d, $^3J_{H-H}$ = 8.5 Hz, *a/b*), 8.39 (2H, d, $^3J_{H-H}$ = 8.5 Hz, *a/b*), 8.25-8.21 (6H, m, *f*), 7.80-7.74 (9H, m, *e* and *g*), 7.17 (2H, s, *n*), 7.15 (4H, s, *i*), 3.38, 3.21, 2.94 (9H, m, *j, k, o* and *p*), 1.41-1.11 (54H, m, *l, m, q* and *r*), -2.74 (2H, s, *h*). **MALDI-TOF MS:** Product not present. $Mo_2(TiPB)_2(A_3BPorphyrin)_2$ calc. for $Mo_2C_{122}H_{104}N_8O_8$ 2004.61 $[M]^+$ m/z, found m/z 2003.62 $[M]^+$. $Mo_2(TiPB)(A_3BPorphyrin)_3$ $Mo_2C_{151}H_{110}N_{12}O_8$ $[M]^+$ m/z 2414.67, found m/z 2413.68 $[M]^+$.

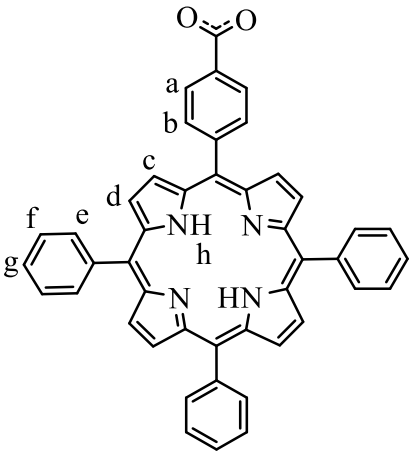

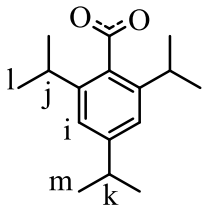

cis-(to porphyrin)

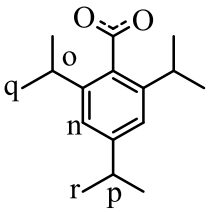

trans-(to porphyrin)

General procedure for *trans*- $Mo_2(TiPB)_2(A_3BPorphyrin)_2$ (2)

$Mo_2(TiPB)_4$ and $A_3BPorphyrin$ were added to a Schlenk tube under an inert atmosphere. 20 cm^3 THF was added by cannula and the resulting solution was stirred at room temperature.

(1) Reaction **B**. $Mo_2(TiPB)_4$ (0.1 g, 0.085 mmol), $A_3BPorphyrin$ (0.11 g, 0.17 mmol). Reaction mixture left stirring for 48 hr. The solvent was removed under reduced pressure, and the crude product was washed with hexane and filtered through celite. The precipitate was recovered with THF, which was subsequently evacuated under reduced pressure to leave behind a greasy brown powder. Yield: 17% (0.028 g, 0.014 mmol). **^{1}H NMR** (600 MHz, chloroform-d) showed product decomposition. **MALDI-TOF MS:** calc. for $Mo_2C_{122}H_{104}N_8O_8$ 2004.61 $[M]^+$ m/z, found m/z 2005.62 $[M]^+$. $Mo_2(TiPB)(A_3BPorphyrin)_3$ also present calc. $Mo_2C_{151}H_{110}N_{12}O_8$ $[M]^+$ m/z 2414.67 found m/z 2412.67.

(2) Reaction **C**. $A_3BPorphyrin$ (0.12 g, 0.18 mmol) was dissolved in 20 cm^3 THF and the resultant solution was added by cannula to $Mo_2(TiPB)_4$ (0.11 g, 0.089 mmol). The solution was left stirring at room temperature for 48 hr. The solvent was removed under reduced pressure and the crude product was washed with diethyl ether and filtered through celite. The precipitate was recovered with THF, which was subsequently evacuated under reduced pressure to yield a brown powder. Yield: 76% (0.14 g, 0.068 mmol). **^{1}H NMR** (400 MHz, chloroform-*d*) (selected peaks) δ_H ppm: 8.90 – 8.71 (m, 20H, c,d,h,i,a/b), 8.37 (d, $^3J_{H-H}$ = 7.8 Hz, 4H, a/b, 8.15 (m, 12H, f), 7.69 (m, 18H, e,g), 7.07 (s, 4H, j). $Mo_2(TiPB)(A_3BPorphyrin)_3$ also present. δ 8.90 – 8.71 (m, 30H, m,n,r,s,v,w,a',b',l/k,t/u), 8.37 (d, 4H, $^3J_{H-H}$ =7.8 Hz, l/k) 8.31 (d, $^3J_{H-H}$ = 8.1 Hz, 2H, t/u), 8.15 (m, 18H, p,y), 7.69 (m, 27H, o,q,x,z), 7.14 (s, 2H, c'). **MALDI-TOF MS:** calc. for $Mo_2C_{122}H_{104}N_8O_8$ 2004.61 $[M]^+$ m/z, found m/z 2005.62 $[M]^+$. $Mo_2(TiPB)(A_3BPorphyrin)_3$ also present calc. $Mo_2C_{151}H_{110}N_{12}O_8$ $[M]^+$ m/z 2414.67, found 2413.67.

(3) Reaction **D**. $Mo_2(TiPB)_4$ (0.1346 g, 0.1139 mmol) was dissolved in 20 cm^3 toluene and the resultant solution was added by cannula to $A_3BPorphyrin$ (0.15 g, 0.2277 mmol). The solution was left stirring at room temperature for 48 hr. The solvent was removed under reduced pressure, and the crude product was washed with diethyl ether and filtered through celite. The precipitate was recovered with THF, which was subsequently evacuated under reduced pressure to leave a purple/brown powder. Yield: 58% (0.13 g, 0.066 mmol). **^{1}H NMR** (400 MHz, chloroform-*d*) poorly resolved and not useful for rigorous structural analysis. **MALDI-TOF MS:** calc. for $Mo_2C_{122}H_{104}N_8O_8$ 2004.61 $[M]^+$ m/z, found m/z 2003.62 $[M]^+$. $Mo_2(TiPB)(A_3BPorphyrin)_3$ also present calc. 2413.67 found m/z 2414.68.

trans-$Mo_2(TiPB)_2(A_3BPorphyrin)_2$

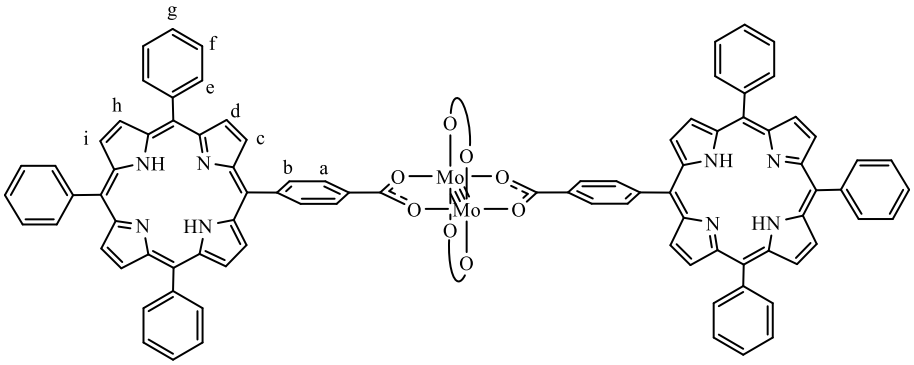

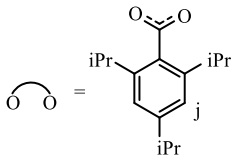

$Mo_2(TiPB)(A_3BPorphyrin)_3$

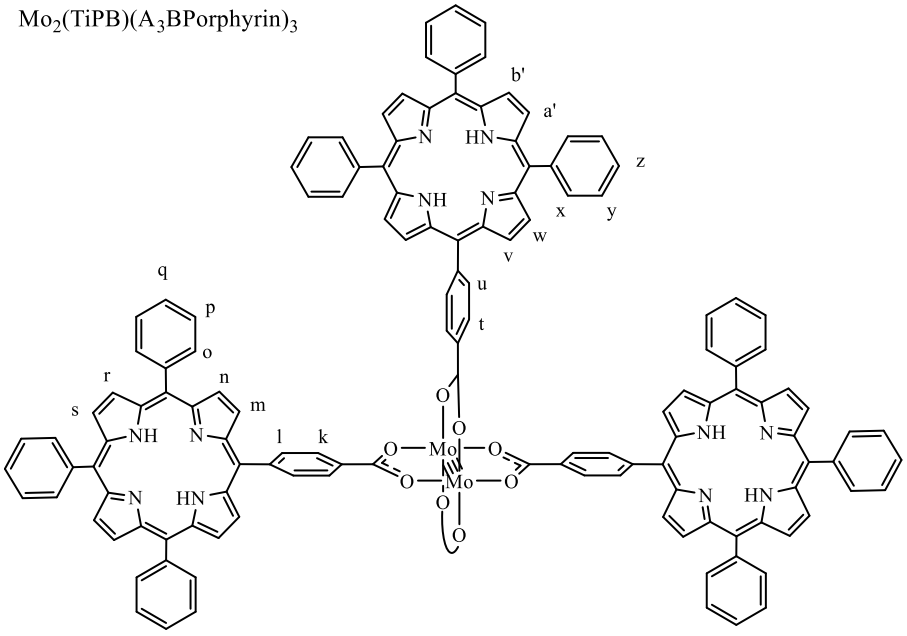

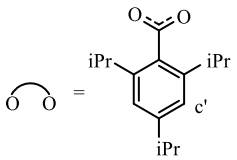

Cis-[Mo_2(TiPB)$_2$(NCMe)$_4$][BF_4]$_2$ (3)

Mo_2(TiPB)$_4$ (0.1 g, 0.085 mmol) was added to a Schlenk tube under an inert atmosphere. 20 cm^3 MeCN and 1 M Et_3OBF_4 in DCM (0.5 cm^3, 0.5 mmol) were added by syringe, and the solution was left stirring at room temperature for 16 hr. The solvent was evacuated under reduced pressure, and the crude product was washed with diethyl ether. The diethyl ether supernatant was subsequently decanted, and this washing process was repeated 4 times. The remaining diethyl ether was evacuated under reduced pressure to leave behind a purple powder. Yield: 48% (0.038 g, 0.041 mmol). No characterisation undertaken, as product immediately used as starting material for the next reaction (see below).

Cis-Mo_2(TiPB)$_2$(A_3BPorphyrin) (4), rection E

A_3B Porphyrin (0.041 g, 0.062 mmol) was weighed out into a Schlenk tube under an inert atmosphere and dissolved in 20 cm^3 of 1:1 a DCM:THF solvent system. 0.5 M NaOMe in methanol (0.12 cm^3, 0.062 mmol) was added to the porphyrin by syringe, and the resulting solution transferred into a separate Schlenk tube with *cis*-[Mo_2(TiPB)$_2$(NCMe)$_4$](BF_4)$_2$ (0.029 g, 0.031 mmol) under an inert atmosphere. The resulting solution was left stirring at room temperature for 48 hr. The reaction mixture was filtered through celite, and the filtrate retained. The solvent was evacuated under reduced pressure, and the crude product was washed with diethyl ether. The mixture was filtered through celite, and the precipitate retained by dissolution in THF. The THF was then removed under reduced pressure to yield a dark brown powder. Yield: 156% (0.0097 g, 0.0049 mmol). **^{1}H NMR** analysis (400 MHz, chloroform-*d*), (400 MHz, pyridine-d_5) poorly resolved and inconclusive. **MALDI-TOF MS:** product not visible.

[Mo_2(TiPB)$_3$]$_2$(μ-*trans*-A_2B_2Porphyrin) (5), reaction F

Mo_2(TiPB)$_4$ (0.67 g, 0.57 mmol) was dissolved in 20 cm^3 THF. The resulting solution was added by cannula to *trans*-A_2B_2Porphyrin (0.2 g, 0.28 mmol) and stirred at room temperature for 56 hr. Solvent subsequently removed under reduced pressure and crude product washed with toluene and filtered through celite. Both precipitate and filtrate retained for analysis. No yield obtained. **^{1}H NMR** (400 MHz, chloroform-*d*) δ_H ppm: 8.95 (d, $^3J_{H\text{-}H}$ = 5.0 Hz, 4H, *c/d*), 8.85 (d, $^3J_{H\text{-}H}$ = 4.8 Hz, 4H *c/d*), 8.75 (d, $^3J_{H\text{-}H}$ = 8.1 Hz, 4H, *a/b*), 8.41 (d, $^3J_{H\text{-}H}$ = 8.0 Hz, 4H, *a/b*), 8.30 – 8.23 (m, 4H, *f*), 7.81 (m, 6H, *e*,*g*), 7.15 (s, 8H, *h*). **MALDI-TOF-MS:** product not visible.

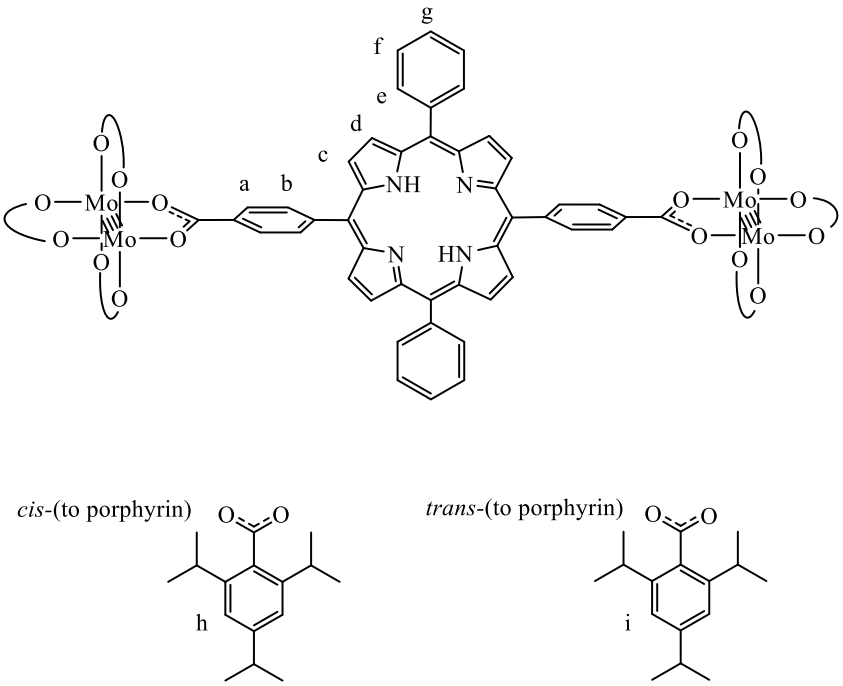

Mo_2(TiPB)(A_3BPorphyrin)$_3$ (6), reaction G

$Mo_2(TiPB)_4$ (0.12 g, 0.1012 mmol) was dissolved in 25 cm^3 THF. The resultant orange solution was added by cannula to A_3BPorphyrin (0.20 g, 0.30 mmol). The solution was left stirring for 16 hr. The solvent was removed under reduced pressure, and 25 cm^3 diethyl ether added by cannula. The mixture was stirred and sonicated, and subsequently filtered through celite. The precipitate was reclaimed by dissolution in THF. The THF was then removed under reduced pressure to yield a purple/brown powder. Yield: 26% (0.062 g, 0.026 mmol) **^{1}H NMR** (400 MHz, chloroform-*d*) only showed decomposition and no product. **MALDI-TOF MS:** calc. for $Mo_2C_{151}H_{110}N_{12}O_8$ $[M]^+$ m/z 2414.67, found m/z 2414.68 $[M]^+$, ($Mo_2(TiPB)_2(A_3BPorphyrin)_2$ also present at 2004.61 m/z).

$Mo_2(OAc)_4$

Acetic acid (80 cm^3) and acetic anhydride (20 cm^3) were heated at reflux temperature (145°C) for 45 min under a dynamic nitrogen atmosphere. $Mo(CO)_6$ (4.20 g, 15.49 mmol) was added under a flow of nitrogen and the mixture was heated at reflux temperature (145°C) for 16 hr. The reaction mixture was then allowed to cool slowly with stirring. The resulting mixture was exposed to air and filtered to obtain yellow crystals. The crystals were washed first with ethanol, and then with diethyl ether and finally with petroleum ether to remove any impurities. The crystals were then dried under reduced pressure and stored under an inert atmosphere. Yield: 54% (1.79 g, 4.18 mmol). **Elemental Analysis:** %C calc. 22.44 found 22.47, %H calc. 2.83 found 2.79, %Remainder calc. 74.73, found 74.74.

$Mo_2(DAniF)_3(OAc)$

$Mo_2(OAc)_4$ (5.00 g, 1.17 mmol), and DAniF (0.90 g, 3.50 mmol) were weighed into a Schlenk tube under an inert atmosphere. 30 cm^3 THF was added by cannula and 7.01 cm^3 of 0.5 M NaOMe added by syringe. The mixture was left to stir at room temperature for 5 hr. The THF was removed under reduced pressure and 20 cm^3 DCM added to the mixture. The resultant solution was filtered through celite, and the filtrate was retained. The DCM was subsequently removed under reduced pressure and 20 cm^3 ethanol was added to the flask. The resultant mixture was stirred and sonicated and the supernatant was removed by cannula. This procedure was repeated 3 times until a bright yellow solid remained, which was stored under an inert atmosphere. Yield: 59% (0.71 g, 0.69 mmol). **^{1}H NMR** (400 MHz, chloroform-*d*) δ_H ppm: 8.47 (s, 2H, e), 8.40 (s, 1H, i), 6.66 (d, $^3J_{H\text{-}H}$ = 8.8 Hz, 8H, *c/d*), 6.53 (d, $^3J_{H\text{-}H}$ = 8.8 Hz, 8H, *c/d*), 6.45 (d, $^3J_{H\text{-}H}$ = 8.9 Hz, 4H, *g/h*), 6.23 (d, $^3J_{H\text{-}H}$ = 8.8 Hz, 4H, *g/h*), 3.72 (s, 12H, b), 3.66 (s, 6H, *f*), 2.62 (s, 3H, *a*).

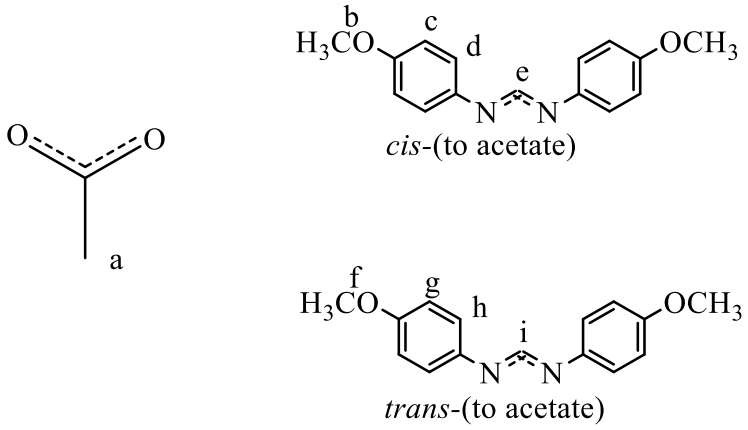

General Procedure for $Mo_2(DAniF)_3(A_3BPorphyrin)$ (7)

$Mo_2(DAniF)_3(OAc)$ and $A_3BPorphyrin$ were stirred together in 20 cm^3 THF. 0.5 M NaOMe in MeOH was added by syringe and the resultant solution was left to stir under an inert atmosphere at room temperature. The THF was removed under reduced pressure and DCM was added by cannula. The resultant mixture was filtered through celite and the filtrate retained. The DCM was removed under reduced pressure. Ethanol was added by cannula and the resultant mixture was stirred and sonicated, followed by filtration through celite. The precipitate was redissolved in THF, and the solvent subsequently removed under reduced pressure to yield a solid product.

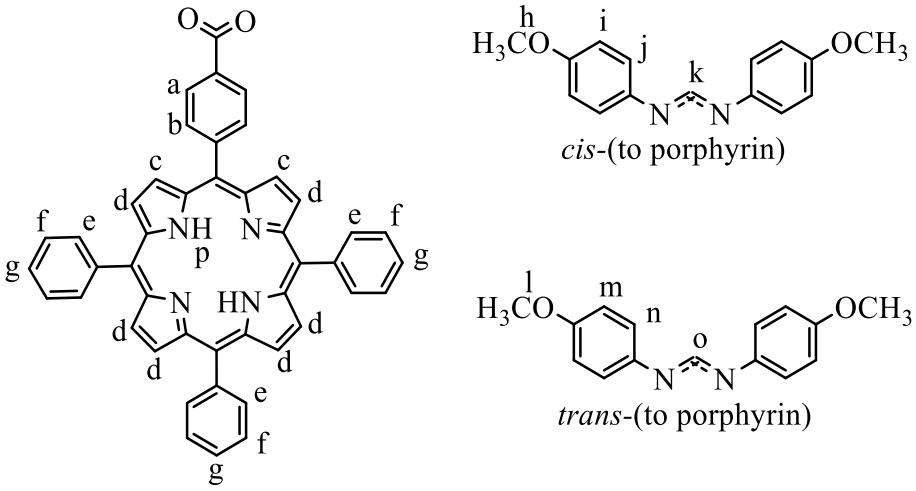

(1) Reaction **H**. $Mo_2(DAniF)_3(OAc)$ (0.1 g, 0.098 mmol) and A_3BPorphyrin (0.065 g, 0.098 mmol) were stirred together with 0.22 cm^3 0.5 M NaOMe for 16 hr. The product was isolated as a dark brown solid. Yield: 44% (0.071 g, 0.044 mmol). **^{1}H NMR** (600 MHz, chloroform-d) δ_H ppm: 8.94 (2H, d, $^3J_{H-H}$ = 6 Hz , c), 8.88-8.82 (6H, m, d), 8.71 (2H, d, $^3J_{H-H}$ = 8 Hz , a/b), 8.56 (2H, s, k), 8.55 (1H, s, o) 8.32 (2H, d, $^3J_{H-H}$ = 8 Hz , a/b), 8.26-8.20 (6H, m, f), 7.80-7.70 (9H, m, e and g), 6.72 (16H, s, i and j), 6.50 (4H, d, $^3J_{H-H}$ = 9 Hz, m/n), 6.33 (4H, d, $^3J_{H-H}$ = 9 Hz , m/n), 3.77-3.66 (18H, m, h and l), -2.74 (2H, s, p). **MALDI-TOF MS:** calc. for $Mo_2C_{90}H_{74}N_{10}O_8$ $[M]^+$ m/z 1618.38, found m/z 1617.38 $[M]^+$.

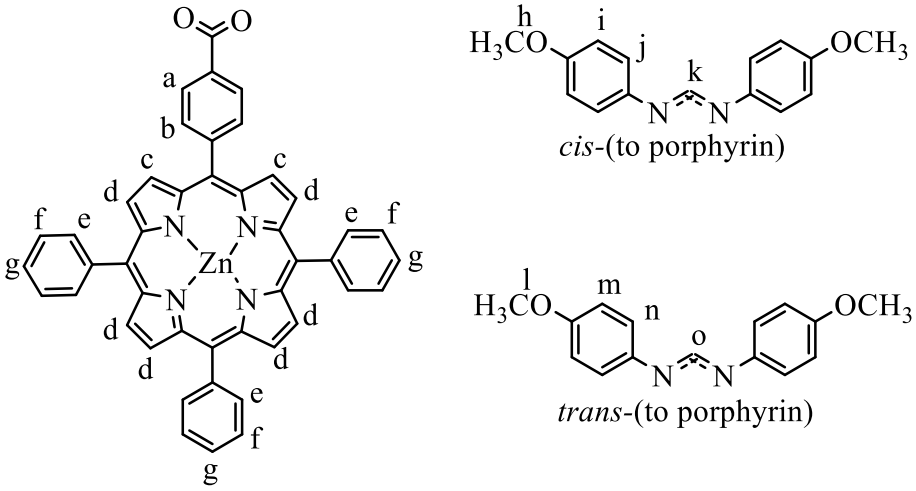

(2) Reaction **K**. $Mo_2(DAniF)_3(OAc)$ (0.1 g, 0.098 mmol) and Zn-A_3BPorphyrin (0.071 g, 0.098 mmol) were stirred together with 0.22 cm^3 0.5 M NaOMe for 16 hr. The product was isolated as a black solid. Yield: 19% (0.03 g, 0.018 mmol). **^{1}H NMR** (400 MHz, chloroform-*d*) δ_H ppm: 8.96 (2H, d, $^3J_{H-H}$ = 4.5 Hz , c), 8.89-8.86 (6H, m, d), 8.66 (2H, d, $^3J_{H-H}$ = 8 Hz , a/b), 8.54 (2H, s, k), 8.53 (1H, s, o) 8.25 (2H, d, $^3J_{H-H}$ = 8 Hz , a/b), 8.18-8.14 (6H, m, f), 7.76-7.69 (9H, m, e and g), 6.71 (16H, s, i and j), 6.49 (4H, d, $^3J_{H-H}$ = 9 Hz, m/n), 6.31 (4H, d, J = 9 Hz , m/n), 3.74-3.68 (18H, m, h and l), -2.74 (2H, s, p) **MALDI-TOF MS:** calc. for $Mo_2C_{90}H_{72}O_8N_{10}Zn$ $[M]^+$ m/z 1680.29, found m/z 1681.30 $[M]^+$.

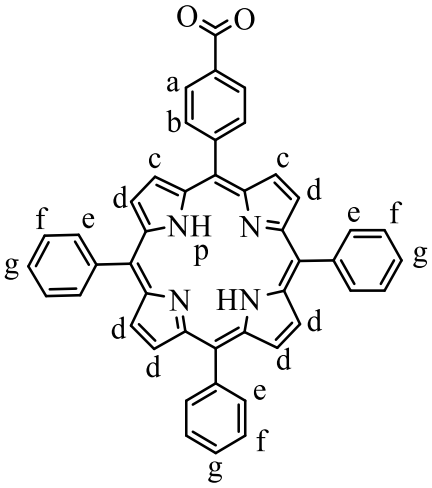

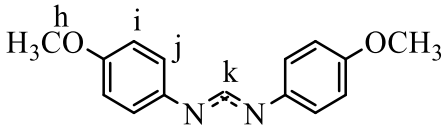

cis-(to porphyrin)

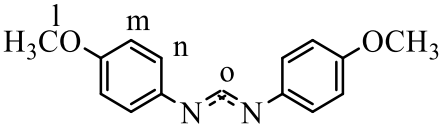

trans-(to porphyrin)

(3) Reaction **I**. $Mo_2(DAniF)_3(OAc)$ and A_3BPorphyrin were stirred together with 0.22 cm^3 0.5 M NaOMe for 3 hr. After the first filtration with DCM, the solution appeared green due to deprotonation of porphyrin ring protons. A few drops of p-tolunesulfonic acid in DCM were added to the solution until the colour changed to brown. Then the general procedure was continued as normal. The product was isolated as a dark brown solid. Yield: 16% (0.026 g, 0.016 mmol). **^{1}H NMR** (400 MHz, chloroform-d) δ_H ppm: 8.93 (2H, d, $^3J_{H-H}$ = 5 Hz , c), 8.86-8.83 (6H, m, d), 8.69 (2H, d, $^3J_{H-H}$ = 8 Hz , a/b), 8.54-8.53 (3H, m, k and o) 8.30 (2H, d, $^3J_{H-H}$ = 8 Hz , a/b), 8.23-8.20 (6H, m, f), 7.79-7.73 (9H, m, e and g), 6.71 (16H, s, i and j), 6.49 (4H, d, $^3J_{H-H}$ = 9 Hz, m/n), 6.32 (4H, d, $^3J_{H-H}$ = 8 Hz , m/n), 3.77-3.66 (18H, m, h and l), -2.77 (2H, s, p) **MALDI-TOF MS:** calc. for $Mo_2C_{90}H_{74}N_{10}O_8$ $[M]^+$ m/z 1618.38, found m/z 1619.39 $[M]^+$.

(4) Reaction **J**. $Mo_2(DAniF)_3(OAc)$ (0.21 g, 0.20 mmol) was stirred with 1.5 equivalents of A_3BPorphryin (0.20 g, 0.31 mmol) with 0.61 cm^3 of 0.5 M NaOMe in methanol for 16 hr. Instead of evacuating solvent and adding DCM, the solvent was reduced to 10% of its initial volume under reduced pressure and was washed with 2 additions of 20 cm^3 of ethanol. The mixture was sonicated, and the supernatant was removed by cannula filtration to leave behind a sticky brown solid. The solid was washed twice with 20 cm^3 diethyl ether, sonicated and the supernatant removed via cannula. The residual solid was a fine brown powder, which was dried under reduced pressure and stored under an inert atmosphere. Yield: 39% (0.13 g, 0.081 mmol). **^{1}H NMR** (400 MHz, chloroform-

d) δ_H ppm: 8.93 (d, $^3J_{H-H}$ = 4.8 Hz, 2H, c), 8.85 (d, $^3J_{H-H}$ = 6.7 Hz, 6H, d), 8.69 (d, $^3J_{H-H}$ = 6.5 Hz, 2H, a/b), 8.54 (s, 3H, k,o), 8.30 (d, $^3J_{H-H}$ = 7.7 Hz, 2H, a/b), 8.22 (dd, $^3J_{H-H}$ = 7.8, 1.7 Hz, 6H, f), 7.77 (m, 9H, e,g), 6.71 (s, 16H, i,j), 6.49 (d, $^3J_{H-H}$ = 9.0 Hz, 4H, m/n), 6.31 (d, $^3J_{H-H}$ = 9.0 Hz, 4H, m/n), 3.74 (s, 12H, h), 3.69 (s, 6H, l), -2.76 (s, 2H, p). **MALDI-TOF MS:** calc. for $Mo_2C_{90}H_{74}N_{10}O_8$ $[M]^+$ m/z 1618.38, found m/z 1618.37 $[M]^+$. UV/Vis measurement taken in a 0.0044 mM solution in THF, 298 K.

[Mo_2(DAniF)$_3$]$_2$(μ-*trans*-A_2B_2Porphyrin) (8), reaction L

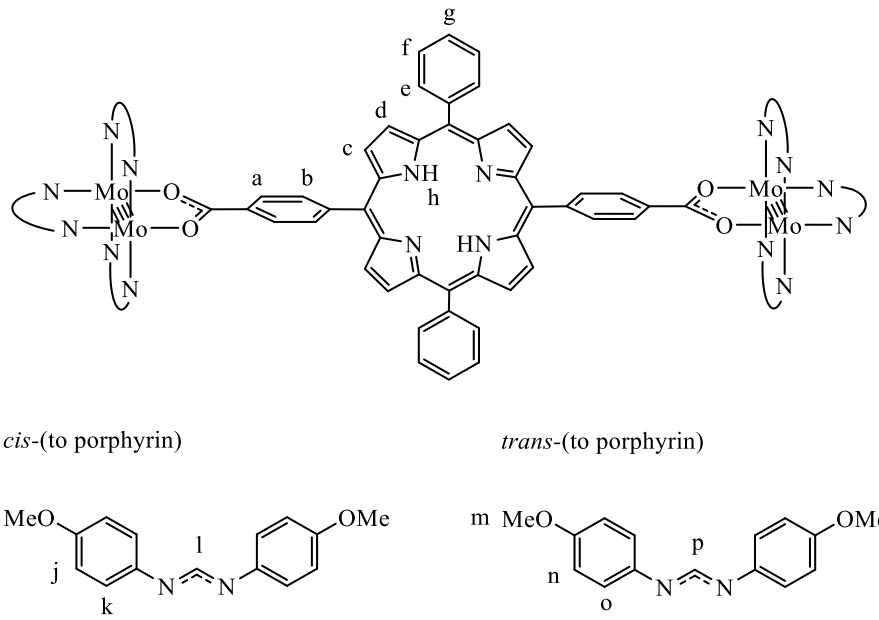

Mo_2(DAniF)$_3$(OAc) (0.44 g, 0.43 mmol) was dissolved in 20 cm^3 THF and 0.86 cm^3 of 0.5 M NaOMe in methanol added by syringe. This solution was added by cannula to *trans*-A_2B_2Porphyrin (0.15 g, 0.22 mmol) and the resulting solution was stirred at room temperature for 3 hr. The solvent was removed under reduced pressure and replaced with 20 cm^3 ethanol. The mixture was stirred and sonicated, before allowing solid to settle at the bottom of the flask. The supernatant was then removed by cannula filtration. This washing procedure was then repeated with 20 cm^3 diethyl ether. Once the diethyl ether had been removed by cannula, the remaining solid was dried under reduced pressure to yield a fine brown powder. Yield 46% (0.26 g, 0.098 mmol). **^{1}H NMR** (400 MHz, chloroform-*d*) δ_H ppm: 8.93 (d, $^3J_{H-H}$ = 4.8 Hz, 4H, *c/d*), 8.85 (d, $^3J_{H-H}$ = 4.9 Hz, 4H, *c/d*), 8.69 (d, $^3J_{H-H}$ = 8.1 Hz, 4H, *a/b*), 8.54 (s, 4H, *l*), 8.45 (s, 2H, *p*), 8.30 (d, $^3J_{H-H}$ = 8.1 Hz, 4H, *a/b*), 8.22 (m, 4H, *f*), 7.76 (m, 6H, *e,g*), 6.71 (s, 32H, *j, k*), 6.51 (d, $^3J_{H-H}$ = 8.7 Hz, 4H, *n/o*), 6.31 (d, $^3J_{H-H}$ = 8.9 Hz, 4H, *n/o*), 3.74 (s, 24H, *i*), 3.72 (s, 12H, *m*), -2.76 (s, 2H, *h*). **MALDI-TOF MS:** calc. for $Mo_4C_{136}H_{118}N_{16}O_{16}$ $[M]^+$ m/z 2622.51, found m/z 2612.51. $[M]^+$. UV/Vis measurement taken in a 0.0047 mM solution in THF, 298 K.

[Mo_2(DAniF)$_3$]$_4$(μ-B_4Porphyrin) (9), reaction M

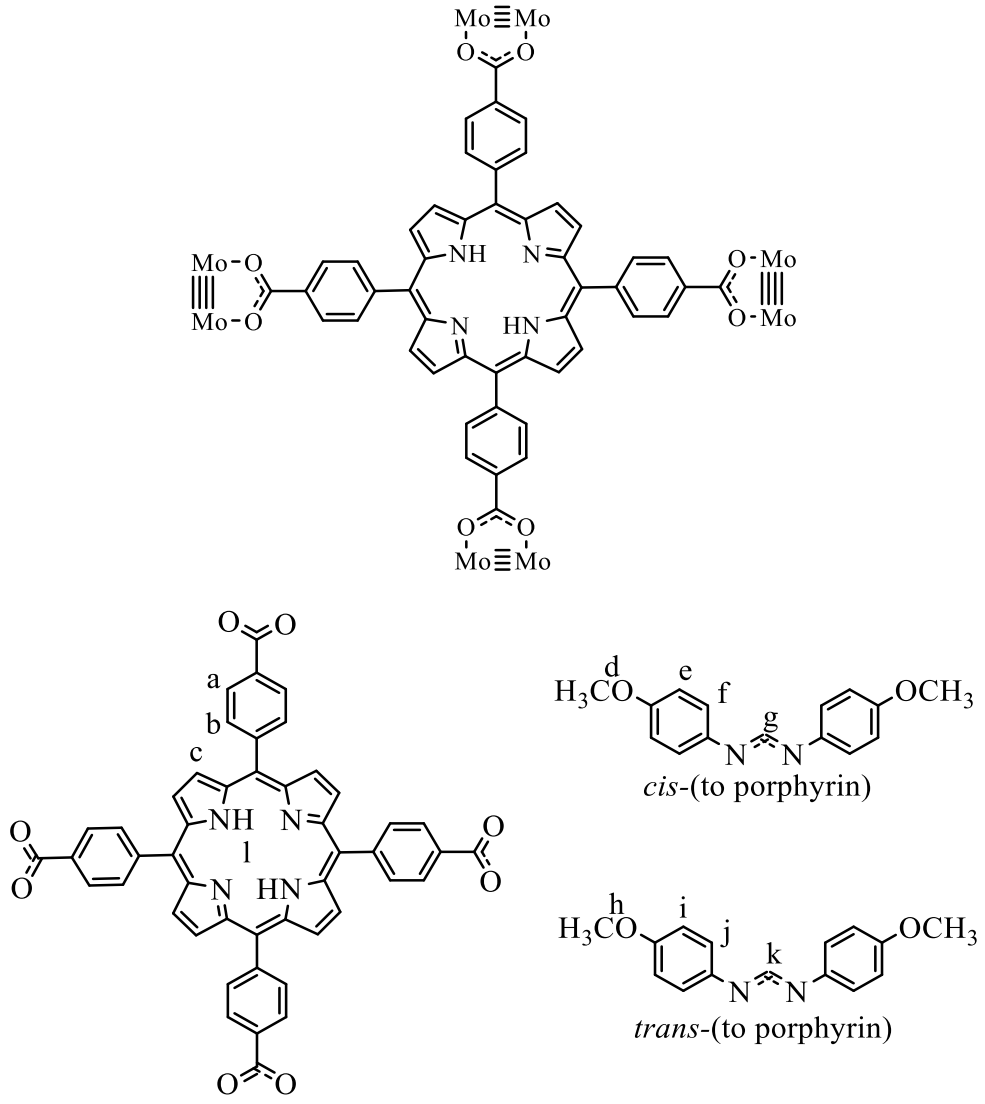

Mo_2(DAniF)$_3$(OAc) (0.10 g, 0.098 mmol) was mixed with B_4Porphyrin (0.019 g, 0.025 mmol). 30 cm^3 THF and 0.22 cm^3 of 0.5 M NaOMe in methanol were added and the resultant solution was stirred at room temperature for 2 hr. The THF evacuated under reduced pressure and replaced by DCM. The mixture was filtered through celite and the filtrate retained. The solution was re-acidified by addition of a few drops of *p*-toluenesulfonic acid dissolved in DCM until the colour changed from green to brown. The solvent was removed under reduced pressure and resulting solid washed with ethanol. The mixture was filtered through celite again, and the precipitate recovered by dissolution in THF. The THF was subsequently removed under reduced pressure to leave behind a sticky black solid. Yield: 10% (0.011 g, 0.0024 mmol). **^{1}H NMR** (400 MHz, chloroform-*d*) δ_H ppm: 8.95 (8H, s, *c*), 8.69 (8H, d, $^3J_{H-H}$ = 8 Hz, *a/b*), 8.53 (12H, s, *g* and *k*), 8.30 (8H, d, $^3J_{H-H}$ = 8 Hz, *a/b*), 6.70 (64H, s, *e* and *f*), 6.53-6.46 (16H, m, *i/j*), 6.30 (16H, d, $^3J_{H-H}$ = 9 Hz, *i/j*), 3.81-3.64 (72H, m, *d* and *h*), -2.74 (2H, s, *l*).

General Procedure for DFArF

Triethyl orthoformate and the relevant fluorinated aniline were weighed out with 1:2 stoichiometry and heated at reflux temperature (120°C) for 3 hr. After 3 hr, the condenser was removed, and the ethanol allowed to boil away. The resulting solid was cooled to room temperature. The crude product was recrystallized with a 1:1 toluene:petroleum ether mixture and filtered to remove impurities, retaining the precipitate. This process was repeated (in general 3-5 times) until colourless crystals were obtained.

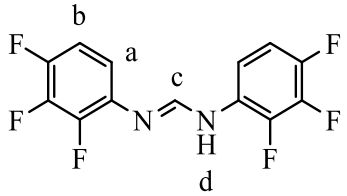

(1) **2,3,4-DFArF**. Triethyl orthoformate (0.5 g, 3.40 mmol) and 2,3,4-trifluoroaniline (1.00 g, 6.80 mmol). Yield: 84% (0.87 g, 2.86 mmol). **^{1}H NMR** (300 MHz, DMSO-d_6) δ_H ppm: 9.97 (s, 1H, d), 8.08 (s, 1H, c), 7.26 (m, 4H, a, b). **^{19}F NMR** (282 MHz, DMSO-d_6) δ_F ppm: -142.71, -147.73, -161.13. **ESI MS:** calc. for $C_{13}H_6N_2F_6$ 305.04 $[M]^+$, found 305.04 $[M]^+$.

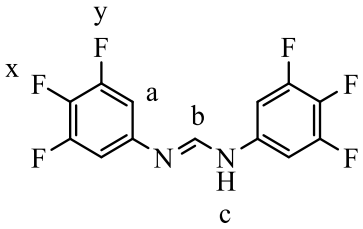

(2) **3,4,5-DFArF**. Triethyl orthoformate (0.5 g, 3.40 mmol) and 3,4,5-trifluoroaniline (1.00 g, 6.80 mmol). Yield: 35% (0.36 g, 1.19 mmol). **^{1}H NMR** (300 MHz, DMSO-d_6) δ_H ppm: 10.20 (s, 1H, c), 8.29 (s, 1H, b), 7.15 (m, 4H, a). ^{19}F NMR (282 MHz, DMSO-d_6) δ_F ppm: -135.35 (y), -169.37 (x). **ESI MS:** calc. for $C_{13}H_6N_2F_6$ 305.04 $[M]^+$, found 305.05 $[M]^+$

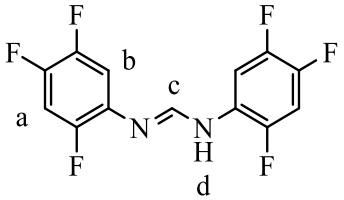

(3) **2,4,5-DFArF**. Triethyl orthoformate (0.5 g, 3.40 mmol) and 3,4,5-trifluoroaniline (1.00 g, 6.80 mmol). Yield: 54% (0.56 g, 1.83 mmol). **^{1}H NMR** (300 MHz, DMSO-d_6) δ_H ppm: 9.96 (s, 1H, d), 8.07 (s, 1H, c), 7.82 – 7.25 (m, 4H, a, b). **^{19}F NMR** (282 MHz, DMSO-d_6) δ_F ppm: -128.76, -142.41.**ESI MS:** calc. for $C_{13}H_6N_2F_6$ 305.04 $[M]^+$, found 305.05 $[M]^+$

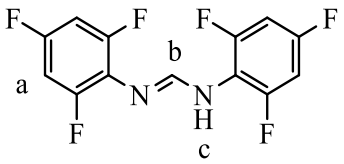

(4) **2,4,6-DFArF**. Triethyl orthoformate (0.5 g, 3.40 mmol) and 3,4,5-trifluoroaniline (1.00 g, 6.80 mmol). Yield: 64% (0.66 g, 2.17 mmol). **^{1}H NMR** (300 MHz, DMSO-d_6) δ 9.28 (s, 1H, c), 7.98 (s, 1H, b), 7.21 (s, 4H, a). **^{19}F NMR** (282 MHz, DMSO-d_6) δ -110.74, -113.96, -117.47, -122.96.

General Procedure for $Mo_2(DFArF)_4$

$Mo(CO)_6$ and the relevant fluorinated formamidine were weighed out with 1:2 stoichiometry into a Schlenk tube fitted with a condenser. 20-30 cm^3 of 1,2-DCB and 2-4 cm^3 THF were added by syringe and the resulting solution was stirred at reflux temperature (160°C) for 16 hr. The solvent system was removed under reduced pressure to leave behind a black solid, and 20 cm^3 ethanol was added by cannula. The resultant mixture was stirred and sonicated, and then left to allow the solid to settle to the bottom of the flask. The supernatant was then removed by cannula. This washing procedure was repeated 3 times until the resultant solid bright was yellow in colour. The solid was then dried under reduced pressure to remove any residual ethanol.

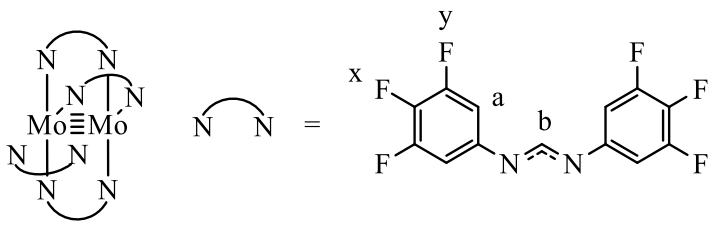

(1) Compound (**i**). $Mo(CO)_6$ (0.26 g, 0.99 mmol) and 3,4,5-DFArF (0.60 g, 1.98 mmol) were stirred together. Yield: 29% (0.20 g, 0.14 mmol). **^{1}H NMR** (300 MHz, DMSO-d6) δ_H ppm: 8.57 (s, 4H, b), 6.51 (dd, $^3J_{H-F}$ = 9.9 Hz, $^4J_{H-F}$ = 6.3 Hz, 16H, a). **^{19}F NMR** (282 MHz, DMSO-d_6) δ_F ppm: -135.58 (dd, $^3J_{F-F}$ = 22.2 Hz, $^4J_{F-F}$ = 10.2 Hz, y), -166.92 – -169.37 (m, x). **MALDI-TOF MS:** calc. for $Mo_2C_{52}H_{20}N_8F_{24}$ $[M]^+$ m/z 1407.95, found m/z 1436.95 $[M]^+$. UV/Vis measurement taken in a 0.021 mM solution in THF, 298 K. Single crystals were grown by heating a sample in 1,2-difluorobenzene and allowing it to cool back to room temperature, and the crystals were analysed by XRD. Crystal data and structure refinement given in table below. Data collected and refined by Theo Tanner.

Empirical formula	$C_{64}H_{28}F_{28}Mo_2N_8$
Formula weight	1632.82
Temperature/K	110.00(10)
Crystal system	monoclinic
Space group	$P2_1/n$
a/Å	13.8788(3)
b/Å	25.1728(5)
c/Å	18.6471(5)
α/°	90
β/°	108.714(3)
γ/°	90
Volume/Å^3	6170.3(3)
Z	4
ρ_{calc}g/cm^3	1.758
μ/mm^{-1}	4.557
F(000)	3216.0

Crystal size/mm^3	0.134 × 0.083 × 0.056
Radiation	Cu Kα (λ = 1.54184)
2Θ range for data collection/°	6.976 to 134.158
Index ranges	-16 ≤ h ≤ 14, -30 ≤ k ≤ 27, -21 ≤ l ≤ 22
Reflections collected	24349
Independent reflections	11018 [R_{int} = 0.0562, R_{sigma} = 0.0687]
Data/restraints/parameters	11018/12/932
Goodness-of-fit on F^2	1.076
Final R indexes [I>=2σ (I)]	R_1 = 0.0638, wR_2 = 0.1574
Final R indexes [all data]	R_1 = 0.0865, wR_2 = 0.1751
Largest diff. peak/hole / e Å^{-3}	2.14/-0.89

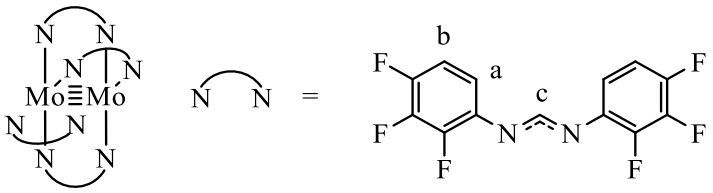

(2) Compound (**ii**). $Mo(CO)_6$ (0.32 g, 1.20 mmol) and 2,3,4-DFArF (0.73 g, 2.39 mmol) were stirred together. Yield: 25 % (0.21 g, 0.15 mmol) **^{1}H NMR** (400 MHz, DMSO-d_6) δ_H ppm: 8.82 (s, 4H, c), 7.10 (q, $^3J_{H-F}$ = 9.3 Hz, 8H, b), 6.54 (d, $^3J_{H-F}$ = 9.4 Hz, 2H, b). **^{19}F NMR** (376 MHz, DMSO-d_6) δ_F ppm: -140.76, -149.93, -160.84. **MALDI-TOF MS:** calc. for $Mo_2C_{52}H_{20}N_8F_{24}$ $[M]^+$ m/z 1407.95, found m/z 1404.96 $[M]^+$. UV/Vis measurement taken in a 0.021 mM solution in THF. Single crystals were grown by layering THF and hexane (1:3 ratio) and resulting crystals analysed by XRD. Crystal data and structure refinement given in table below. Data collected and refined by Theo Tanner and Adrian Whitwood.

Empirical formula	$C_{104}H_{40}F_{48}Mo_4N_{16}$
Formula weight	2809.28
Temperature/K	110.00(10)
Crystal system	monoclinic

Space group	$P2_1/n$
a/Å	11.6998(3)
b/Å	14.6607(3)
c/Å	18.4878(3)
α/°	90
β/°	107.805(2)
γ/°	90
Volume/$Å^3$	3019.27(12)
Z	1
$\rho_{calc}g/cm^3$	1.545
μ/mm^{-1}	4.453
F(000)	1376.0
Crystal size/mm^3	0.184 × 0.141 × 0.118
Radiation	Cu Kα (λ = 1.54184)
2Θ range for data collection/°	7.848 to 142.106
Index ranges	$-13 \leq h \leq 14$, $-13 \leq k \leq 17$, $-22 \leq l \leq 18$
Reflections collected	7206
Independent reflections	4374 [R_{int} = 0.0151, R_{sigma} = 0.0230]
Data/restraints/parameters	4374/0/388
Goodness-of-fit on F^2	1.048
Final R indexes [I>=2σ (I)]	R_1 = 0.0222, wR_2 = 0.0582
Final R indexes [all data]	R_1 = 0.0241, wR_2 = 0.0596
Largest diff. peak/hole / e $Å^{-3}$	0.39/-0.52

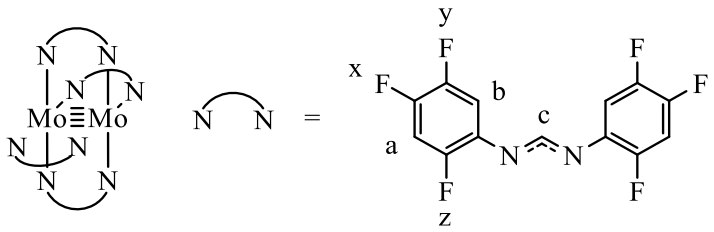

(3) Compound (**iii**). $Mo(CO)_6$ (0.25 g, 0.95 mmol) and 2,4,5-DFArF (0.58 g, 1.90 mmol) were stirred together. Yield: 11% (0.075 g, 0.053 mmol). **^{1}H NMR** (400 MHz, DMSO-d_6) δ_H ppm: 8.75 (s, 1H, c), 7.26 (m, 2H, a/b), 6.93 (m, 2H, a/b) **MALDI-TOF MS:** calc. for $Mo_2C_{52}H_{20}N_8F_{24}$ $[M]^+$ m/z 1407.95, found m/z 1408.96 $[M]^+$. UV/Vis measurement taken in a 0.035 mM solution in THF, 298 K. UV/Vis measurement taken in a 0.021 mM solution in THF. Single crystals were grown by heating up sample in 1,2-difluorobenzene, and subsequent layering with hexane in 1:4 ratio and obtained crystals were analysed by XRD. Crystal data and structure refinement given in table below. Data collected and refined by Theo Tanner and Adrian Whitwood.

Empirical formula	$C_{52}H_{20}F_{24}Mo_2N_8$
Formula weight	1404.64
Temperature/K	110.00(14)
Crystal system	triclinic
Space group	P-1
a/Å	12.3797(5)
b/Å	19.1386(6)
c/Å	21.9281(7)
α/°	73.700(3)
β/°	76.805(3)
γ/°	87.364(3)
Volume/Å^3	4854.0(3)
Z	4
ρ_{calc}g/cm^3	1.922
μ/mm^{-1}	5.540

F(000)	2752.0
Crystal size/mm^3	0.052 × 0.031 × 0.025
Radiation	Cu Kα (λ = 1.54184)
2Θ range for data collection/°	7.298 to 134.16
Index ranges	-11 ≤ h ≤ 14, -22 ≤ k ≤ 22, -26 ≤ l ≤ 26
Reflections collected	34716
Independent reflections	17310 [R_{int} = 0.0369, R_{sigma} = 0.0520]
Data/restraints/parameters	17310/12/1575
Goodness-of-fit on F^2	1.010
Final R indexes [I>=2σ (I)]	R_1 = 0.0334, wR_2 = 0.0686
Final R indexes [all data]	R_1 = 0.0506, wR_2 = 0.0756
Largest diff. peak/hole / e Å^{-3}	0.65/-0.61

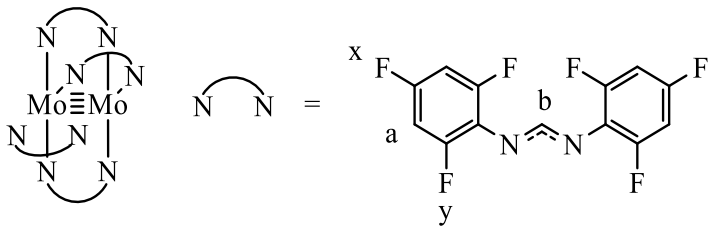

(4) Compound (**iv**). $Mo(CO)_6$ (0.2467 g, 0.9343 mmol) and 2,4,6-DFArF (0.57 g, 1.87 mmol) were stirred together. Yield: 20% (0.13 g, 0.43 mmol). **^{1}H NMR** (400 MHz, DMSO-d_6) δ_H ppm: 8.63 (s, 4H, b), 6.88 (t, $^3J_{H-F}$ = 8.4 Hz, 16H, a). **^{19}F NMR** (376 MHz, DMSO-d_6) δ_F ppm: -114.89, -121.27 **MALDI-TOF MS:** calc. for $Mo_2C_{52}H_{20}N_8F_{24}$ $[M]^+$ m/z 1407.95, found m/z 1408.96 $[M]^+$. Single crystals were grown by layering THF and hexane (1:10) and obtained crystals were analysed by XRD. UV/Vis measurement taken in a 0.026 mM solution in THF. Crystal data and structure refinement given in table below. Data collected and refined by Adrian Whitwood.

Empirical formula	$C_{59.99}H_{35.98}F_{24}Mo_2N_8O_2$
Formula weight	1548.71
Temperature/K	110.00(10)
Crystal system	triclinic

Space group	P-1
a/Å	11.1746(7)
b/Å	11.3264(6)
c/Å	11.9436(6)
α/°	71.875(4)
β/°	82.228(5)
γ/°	80.445(5)
Volume/$Å^3$	1411.09(14)
Z	1
$\rho_{calc}g/cm^3$	1.822
μ/mm^{-1}	4.859
F(000)	768.0
Crystal size/mm^3	0.22 × 0.159 × 0.025
Radiation	Cu Kα (λ = 1.54184)
2Θ range for data collection/°	7.82 to 134.156
Index ranges	$-13 \leq h \leq 13$, $-11 \leq k \leq 13$, $-14 \leq l \leq 12$
Reflections collected	9380
Independent reflections	5044 [R_{int} = 0.0230, R_{sigma} = 0.0347]
Data/restraints/parameters	5044/8/536
Goodness-of-fit on F^2	1.031
Final R indexes [I>=2σ (I)]	R_1 = 0.0265, wR_2 = 0.0626
Final R indexes [all data]	R_1 = 0.0320, wR_2 = 0.0660
Largest diff. peak/hole / e $Å^{-3}$	0.52/-0.52

Bibliography

1 F. A. Cotton, C. A. Murillo and R. A. Walton, in *Multiple Bonds Between Metal Atoms*, Springer Science and Business Media, Inc., New York, 3rd Editio., 2005.

2 L. A. Wilkinson, *J. Organomet. Chem.*, 2020, **43**, 111–1143.

3 M. H. Chisholm, *Coord. Chem. Rev.*, 2015, 282–283, 60–65.

4 S. E. Brown-Xu, M. H. Chisholm, C. B. Durr and T. F. Spilker, *J. Am. Chem. Soc.*, 2013, **135**, 8254–8259.

5 Y. Yamashita, M. M. Salter, K. Aoyama and S. Kobayashi, *Angew. Chemie Int. Ed.*, 2006, **45**, 3816–3819.

6 S. Rej, M. Majumdar, S. Kando, Y. Sugino, H. Tsurugi and K. Mashima, *Inorg. Chem.*, 2017, **56**, 634–644.

7 H. Tsurugi, A. Hayakawa, S. Kando, Y. Sugino and K. Mashima, *Chem. Sci.*, 2015, **6**, 3434–3439.

8 M. Köberl, M. Cokoja, W. A. Herrmann and F. E. Kühn, *Dalton. Trans.*, 2011, 40, 6834–6859.

9 C. Jiang, P. J. Young, S. Brown-Xu, J. C. Gallucci and M. H. Chisholm, *Inorg. Chem*, 2017, **56**, 1433–1445.

10 M. J. Byrnes, M. H. Chisholm, R. J. H. Clark, J. C. Gallucci, C. M. Hadad and N. J. Patmore, *Inorg. Chem.*, 2004, **43**, 6334–6344.

11 H. M. McConnell, *J. Chem. Phys.*, 1961, **35**, 508–515.

12 C. Creutz and H. Taube, *J. Am. Chem. Soc.*, 1969, **91**, 3988–3989.

13 R. F. Winter, *Organometallics*, 2014, **33**, 4517–4536.

14 M. B. Robin and P. Day, *Adv. Inorg. Chem. Radiochem.*, 1968, **10**, 247–422.

15 C. Y. Liu, X. Xiao, M. Meng, Y. Zhang and M. J. Han, *J. Phys. Chem. C*, 2013, **117**, 19859–19865.

16 M. V. Barybin, M. H. Chisholm, N. S. Dalal, T. H. Holovics, N. J. Patmore, R. E. Robinson and D. J. Zipse, *J. Am. Chem. Soc.*, 2005, **127**, 15182–15190.

17 M. H. Chisholm, *Philos. Trans. R. Soc. A Math. Phys. Eng. Sci.*, 2008, **366**, 101–112.

18 M. H. Chisholm and N. J. Patmore, *J. Chem. Soc. Dalton. Trans.*, 2006, 3164–3169.

19 Y. Y. Wu, M. Meng, G. Y. Wang, P. Feng and C. Y. Liu, *Chem. Commun.*, 2017, **53**, 3030–3033.

20 J. P. Launay, *Chem. Soc. Rev.*, 2001, **30**, 386–397.

21 F. A. Cotton, J. P. Donahue, C. A. Murillo and L. M. Pérez, *J. Am. Chem. Soc.*, 2003, **125**, 5486–5492.

22 F. A. Cotton, J. P. Donahue and C. A. Murillo, *J. Am. Chem. Soc.*, 2003, **125**, 5436–5450.

23 L. Chen, S. Mallick, Y. N. Tan, M. Meng and C. Y. Liu, *Inorg. Chem.*, 2017, **56**, 7470–7481.

24 S. Mallick, Y. Lu, M. H. Luo, M. Meng, Y. N. Tan, C. Y. Liu and J. L. Zuo, *Inorg. Chem.*, 2017, **56**, 14888–14899.

25 M. Meng, Z. Tang, S. Mallick, M. H. Luo, Z. Tan, J. Y. Liu, J. Shi, Y. Yang, C. Y. Liu and W. Hong, *Nanoscale*, 2020, **12**, 10320–10327.

26 J. Hicks, S. P. Ring and N. J. Patmore, *Dalton. Trans.*, 2012, **41**, 6641–6650.

27 C. Lin, J. D. Protasiewicz, E. T. Smith and T. Ren, *Inorg. Chem.*, 1996, **35**, 6422–6428.

28 T. Ren, *Coord. Chem. Rev.*, 1998, **175**, 43–58.

29 S. Krackl, S. Inoue, M. Driess and S. Enthaler, *Eur. J. Inorg. Chem.*, 2011, **2011**, 2103–2111.

30 N. Rodríguez-López, N. Metta, A. J. Metta-Magana and D. Villagrán, *Inorg. Chem.*, 2020, **59**, 3091–3101.

31 C. Lin, J. D. Protasiewicz, E. T. Smith and T. Ren, *Inorg. Chem.*, 1996, **35**, 6422–6428.

32 H. Miyasaka, N. Motokawa, R. Atsuumi, H. Kamo, Y. Asai and M. Yamashita, *Dalton. Trans.*, 2010, **40**, 673–682.

33 M. O. Senge, *Chem. Commun.*, 2011, **47**, 1943–1960.

34 A. Yella, C. L. Mai, S. M. Zakeeruddin, S. N. Chang, C. H. Hsieh, C. Y. Yeh and M. Grätzel, *Angew. Chemie - Int. Ed.*, 2014, **53**, 2973–2977.

35 W. Zheng, N. Shan, L. Yu and X. Wang, *Dye. Pigment.*, 2008, **77**, 153–157.

36 P. Bhyrappa, M. Sankar and B. Varghese, *Inorg. Chem.*, 2006, **45**, 4136–4149.

37 P. Chen, O. S. Finikova, Z. Ou, S. A. Vinogradov and K. M. Kadish, *Inorg. Chem.*, 2012, **51**, 6200–6210.

38 J. P. Celli, B. Q. Spring, I. Rizvi, C. L. Evans, K. S. Samkoe, S. Verma, B. W. Pogue and T. Hasan, *Chem. Rev.*, 2010, **110**, 2795–2838.

39 J. Kou, D. Dou and L. Yang, *Oncotarget*, 2017, **8**, 81591–81603.

40 C. F. Zhuang, X. X. Tang, D. Wang, W. H. Lian, A. Q. Xia, Y. H. Shi and T. S. Sht, *Pol. J. Chem.*, 2009, **83**, 2205–2213.

41 M. Su, Y. Hu, A. Yu, Z. Peng, W. Long, S. Gao, P. Peng, B. Su and F.-F. Li, *Nanoscale Adv.*, 2021, **3**, 1096–1105.

42 S. A. Vail, J. P. C. Tomé, P. J. Krawczuk, A. Dourandin, V. Shafirovich, J. A. S. Cavaleiro and D. I. Schuster, *J. Phys. Org. Chem.*, 2004, **17**, 814–818.

43 L. Jin, S. Lv, Y. Miao, D. Liu and F. Song, *ChemCatChem*, 2021, **13**, 140–152.

44 M. G. Walter, A. B. Rudine and C. C. Wamser, *J. Porphyr. Phthalocyanines*, 2010, **14**, 759–792.

45 H. Zhou, J. M. Ji and H. K. Kim, *Dye. Pigment.*, 2021, **187**, 109082.

46 J. Lu, S. Liu and M. Wang, *Front. Chem.*, 2018, **6**, 541.

47 Y. Hu, W. A. Webre, M. B. Thomas, A. Moss, S. N. Hancock, J. Schaffner, F. D'Souza and H. Wang, *J. Mater. Chem. A*, 2019, **7**, 10712–10722.

48 S. Mathew, A. Yella, P. Gao, R. Humphry-Baker, B. F. E. Curchod, N. Ashari-Astani, I. Tavernelli, U. Rothlisberger, M. K. Nazeeruddin and M. Grätzel, *Nat. Chem.*, 2014, **6**, 242–247.

49 F. M. Karmova, V. S. Lebedeva and A. F. Mironov, *Russ. J. Gen. Chem.*, 2016, **86**, 2145–2179.

50 D. K. Dogutan, S. H. H. Zaidi, P. Thamyongkit and J. S. Lindsey, *J. Org. Chem.*, 2007, **72**, 7701–7714.

51 A. Wiehe, C. Ryppa and M. O. Senge, *Org. Lett.*, 2002, **4**, 3807–3809.

52 J. S. Lindsey, *Acc. Chem. Res.*, 2010, **43**, 300–311.

53 A. D. Adler, F. R. Longo, J. D. Finarelli, J. Goldmacher, J. Assour and L. Korsakoff, *J. Org. Chem.*, 1967, **32**, 476.

54 J. S. Lindsey, I. C. Schreiman, H. C. Hsu, P. C. Kearney and A. M. Marguerettaz, *J. Org. Chem.*, 2002, **52**, 827–836.

55 B. J. Littler, Y. Ciringh and J. S. Lindsey, *J. Org. Chem.*, 1999, **64**, 2864–2872.

56 D. M. Wallace, S. H. Leung, M. O. Senge and K. M. Smith, *J. Org. Chem.*, 1993, **58**, 7245–7257.

57 S. Neya and N. Funasaki, *Tetrahedron Lett.*, 2002, **43**, 1057–1058.

58 S. Hatscher and M. O. Senge, *Tetrahedron Lett.*, 2003, **44**, 157–160.

59 D. E. Chumakov, A. V Khoroshutin, A. V Anisimov and K. I. Kobrakov, *Chem. Heterocycl. Compd.*, 2009, **45**, 259–283.

60 O. B. Locos and D. P. Arnold, *Org. Biomol. Chem.*, 2006, **4**, 902–916.

61 M. Taniguchi, N. K. Man, D. Ra and J. S. Lindsey, *J. Org. Chem.*, 2005, **70**, 275–285.

62 B. J. Burnett, P. M. Barron and Wonyoung Choe, *CrystEngComm*, 2012, **14**, 3839–3846.

63 Y. Zhao, L. Jiang, L. Shangguan, L. Mi, A. Liu and S. Liu, *J. Mater. Chem. A*, 2018, **6**, 2828–2833.

64 S. Motoyama, R. Makiura, O. Sakata and H. Kitagawa, *J. Am. Chem. Soc.*, 2011, **133**, 5640–5643.

65 X. Wang, W. Y. Gao, Z. Niu, L. Wojtas, J. A. Perman, Y. S. Chen, Z. Li, B. Aguila and S. Ma, *Chem. Commun.*, 2018, **54**, 1170–1173.

66 M. C. So, S. Jin, H. J. Son, G. P. Wiederrecht, O. K. Farha and J. T. Hupp, *J. Am. Chem. Soc.*, 2013, **135**, 15698–15701.

67 S. Goswami, L. Ma, A. B. F. Martinson, M. R. Wasielewski, O. K. Farha and J. T. Hupp, *ACS Appl. Mater. Interfaces*, 2016, **8**, 30863–30870.

68 Y. Kataoka, K. S. Kataoka, H. Murata, M. Handa, W. Mori and T. Kawamoto, *Inorg. Chem. Commun.*, 2016, **68**, 37–41.

69 X. Liu, J. Zhou, M. Meng, G. Y. Zhu, Y. Tan, X. Chen, J. Wei, D.-B. Kuang, Y. Y. Wu, S. Su, T. Cheng, Y. Zhou and C. Y. Liu, *Appl. Catal. B Environ.*, 2020, **286**, 119836.

70 C. D. Windle, M. W. George, R. N. Perutz, P. A. Summers, X. Z. Sun and A. C. Whitwood, *Chem. Sci.*, 2015, **6**, 6847–6864.

71 P. Wang, S. Guo, H. J. Wang, K. K. Chen, N. Zhang, Z. M. Zhang and T. B. Lu, *Nat. Commun.*, 2019, **10**, 3155.

72 X. Zhao, L. Yuan, Z. Q. Zhang, Y. S. Wang, Q. Yu and J. Li, *Inorg. Chem.*, 2016, **55**, 5287–5296.

73 F. A. Cotton, C. Y. Liu and C. A. Murillo, *Inorg. Chem.*, 2004, **43**, 2267–2276.

74 B. G. Alberding, M. H. Chisholm, Y. H. Chou, J. C. Gallucci, Y. Ghosh, T. L. Gustafson, N. J. Patmore, C. R. Reed and C. Turro, *Inorg. Chem.*, 2009, **48**, 4394–4399.

75 F. A. Cotton, A. H. Reid and W. Schwotzer, *Inorg. Chem.*, 1985, **24**, 3965–3968.

76 G. E. S. M. J. Frisch, G. W. Trucks, H. B. Schlegel, V. B. M. A. Robb, J. R. Cheeseman, G. Scalmani, A. V. M. G. A. Petersson, H. Nakatsuji, X. Li, M. Caricato, H. P. H. J. Bloino, B. G. Janesko, R. Gomperts, B. Mennucci, D. W.-Y. J. V. Ortiz, A. F. Izmaylov, J. L. Sonnenberg, A. P. F. Ding, F. Lipparini, F. Egidi, J. Goings, B. Peng, N. R. T. Henderson, D. Ranasinghe, V. G. Zakrzewski, J. Gao, R. F. G. Zheng, W. Liang, M. Hada, M. Ehara, K. Toyota, H. N. J. Hasegawa, M. Ishida, T. Nakajima, Y. Honda, O. Kitao, J. E. P. T. Vreven, K. Throssell, J. A. Montgomery, Jr., K. N. K. F. Ogliaro, M. J. Bearpark, J. J. Heyd, E. N. Brothers, J. N. V. N. Staroverov, T. A. Keith, R. Kobayashi, S. S. I. K. Raghavachari, A. P. Rendell, J. C. Burant, R. C. J. Tomasi, M. Cossi, J. M. Millam, M. Klene, C. Adamo, O. F. J. W. Ochterski, R. L. Martin, K. Morokuma and and D. J. F. J. B. Foresman, 2016.